(2+1)-d U(1) Quantum Link and Quantum Dimer Models

Inauguraldissertation
der Philosophisch-naturwissenschaftlichen Fakultät
der Universität Bern

vorgelegt von

Philippe Widmer

von Heimiswil BE

2015

Leiter der Arbeit:

Prof. Dr. Uwe-Jens Wiese

Albert Einstein Center for Fundamental Physics
Institut für theoretische Physik, Universität Bern

(2+1)-d U(1) Quantum Link and Quantum Dimer Models

Inauguraldissertation
der Philosophisch-naturwissenschaftlichen Fakultät
der Universität Bern

vorgelegt von

Philippe Widmer

von Heimiswil BE

2015

Leiter der Arbeit:

Prof. Dr. Uwe-Jens Wiese

Albert Einstein Center for Fundamental Physics
Institut für theoretische Physik, Universität Bern

Von der Philosophisch-naturwissenschaftlichen Fakultät angenommen.

Bern, 17.08.2015 der Dekan:

Prof. Dr. Gilberto Colangelo

Abstract

Quantum link models are generalizations of lattice gauge theories, where the classical gauge fields are replaced by quantum operators. While these quantum models with discrete variables have a finite-dimensional Hilbert space per link, the continuous gauge symmetry is still exact. Using exact diagonalization and an efficient cluster algorithm, we study a quantum link model in $2 + 1$ dimensions with a $U(1)$ gauge symmetry, finding exotic phases. The theory is confining at zero temperature with a spontaneously broken translation symmetry. A crystalline phase exhibits confinement via multi-stranded strings between charge-anti-charge pairs. A phase transition between two distinct confined phases is weakly first order and has an emergent spontaneously broken approximate $SO(2)$ global symmetry. The low-energy physics is described by a (2+1)-d $\mathbb{R}P(1)$ effective field theory, perturbed by an $SO(2)$ breaking operator, which prevents the interpretation of the emergent pseudo-Goldstone boson as a dual photon. This model is an ideal candidate to be implemented in quantum simulators to study phenomena that are not accessible using Monte Carlo simulations such as the real-time evolution of the confining string and the real-time dynamics of the pseudo-Goldstone boson.

Additionally, the framework of quantum link models can be applied to other theories as well. In particular, the quantum dimer model, a $U(1)$ gauge theory that addresses aspects of the physics of high-T_c superconductors, can be re-expressed as a quantum link model. Based on the insights from the quantum link model, we gain access to quantum Monte Carlo simulations that are significantly more efficient than what has previously been possible, allowing us to shed more light on the phase structure of this model. We find that the theory exists in a confining columnar valence bond solid phase. The interfaces separating distinct columnar phases display plaquette order, which, however, is not realized as a bulk phase. Static "electric" charges are confined by flux tubes that consist of multiple strands, each carrying a fractionalized flux $\frac{1}{4}$. A soft pseudo-Goldstone mode (which becomes exactly massless at the Rokhsar-Kivelson point) extends deep into the columnar phase, with potential implications for high-T_c physics.

Contents

1 Introduction

Solving strongly coupled problems in particle and condensed matter physics is a difficult task, which leads to a number of important open questions concerning e.g. real-time dynamics and the physics at non-zero baryon density in particle physics or high-T_c superconductivity in condensed matter physics. In this thesis we will show that quantum link models may offer a way to solve or circumvent some of these problems.

In particle physics, quantum chromodynamics describes the strong interaction, governing the behavior of the quark and gluon fields. These give rise to the fundamental particles that form protons and neutrons, which (together with electrons) are the basic building blocks of ordinary stable matter. At high energies, quantum chromodynamics shows asymptotic freedom, which means that the coupling strength becomes weaker, allowing perturbative calculations. In the strong coupling case, i.e. at low energies, this approach is not possible. Additionally, neither phenomena concerning a large number of particles (like e.g. a quark-gluon-plasma) nor properties of the theory like confinement or chiral symmetry breaking are accessible with perturbative methods. Confinement is the effect that, at low energies, quarks and gluons cannot exist on their own as free particles. Only states that are neutral with respect to the color charge of quantum chromodynamics have finite energy and appear in the physical spectrum.

The only non-perturbative approach known today is based on replacing the continuous space-time by a discrete lattice. It was first introduced by Wilson [1] and has since been used to achieve a number of remarkable results. In 2+1 dimensions, for example, it has first been shown by Polyakov [2, 3] and later been rigorously proved by Göpfert and Mack [4] that the compact $U(1)$ lattice gauge theory is confining for all values of the coupling constant. This is not true in higher dimensions. In 2+1 dimensions, confinement is related to the condensation of magnetic monopoles, which are instanton-like events (centered at an instant in space-time). In 3+1 dimensions magnetic monopoles are particles, which can also exist in a non-confining Coulomb phase. Furthermore, the lattice formulation is suitable for large-scale computer simulations, which has been used with great success. Most notably, many properties of hadrons have been numerically calculated (see e.g. [5, 6, 7, 8]), including the low-energy mass spectrum of quantum chromodynamics, which is not accessible with perturbative methods due to confinement, and calculations of the nature of its finite temperature transition where chiral symmetry spontaneously breaks and confinement appears.

In condensed matter physics, much research has gone into attempts to understand high-T_c superconductivity. The Hubbard model [9] has been proposed already early on as a model for it. Since then, many different models with a large number of strongly coupled degrees of freedom have been investigated analytically as well as numerically, among them gauge field theories similar to the ones used in particle physics. One of these is the quantum dimer model [10]. It implements Anderson's ideas of resonating valence bonds [11] as a potential route toward understand high-T_c superconductivity. A dimer connecting neighboring lattice sites represents a singlet-pair of two spins $\frac{1}{2}$, potentially related to preformed Cooper pairs that arise when an antiferromagnet turns into a high-T_c superconductor upon doping. In the undoped dimer model, each lattice site is touched by exactly one dimer, thus modeling a system in which each spin participates in a singlet pair. Even though a lot of progress has been made on unraveling the phase structure of classical and quantum dimer models for various lattice geometries [12, 13, 14, 15, 16, 17, 18, 19, 20, 21, 22, 23], the results are still inconclusive overall. Another important topic in condensed matter physics are the spin liquid models [24, 25]. These are systems without any broken symmetry, i.e. they are in a disordered state.

Despite the success of numerical calculations in both condensed matter and particle physics, there are still many problems that are currently unsolvable. Often a so-called sign problem prevents simulation-based approaches. The Monte Carlo technique for evaluating difficult multi-dimensional integrals numerically is based on statistical importance sampling where the part of the integrand that represents a Boltzman-type factor is interpreted as a probability. This method breaks down if the sign of this factor can become negative or if the factor is complex. In both cases, changing phases (or signs) lead to large cancellations and to a very small signal to noise ratio. This problem occurs in a large number of physical cases of interest, including for example calculations with a baryon chemical potential which are needed to study the phase diagram of quantum chromodynamics. Also the calculation of the real-time evolution of systems in condensed matter, nuclear and particle physics are not possible due to a very severe sign problem. Only calculations in Euclidean time (where the real-time t is substituted with the imaginary time it) are practically feasible.

An alternative approach may be based on the rapid development of the field of atomic, molecular, and optical physics (AMO). The basic idea that the use of quantum variables could speed up the simulation tremendously was conceived by Feynman already early on [26]. Special purpose quantum computers, known as quantum simulators [27], are used as digital [28] or analog devices [29] to simulate strongly coupled quantum systems. Recently, the use of quantum simulators to study the real-time evolution in gauge theories and their phase structure in the context of particle physics has been proposed [30, 31, 32, 33, 34, 35, 36, 37, 38]. The idea behind the quantum simulator constructions is that the quantum mechanical nature

of quarks and gluons can be embodied for example by ultra-cold atoms in optical lattices, by ultra-cold ions in ion traps or by superconducting quantum circuits. The interactions between the atoms, ions or circuits can be tuned, so that they follow a properly designed Hamiltonian. The quantum degrees of freedom evolve in time according to this Hamiltonian. A number of important models, such as the Bose-Hubbard model and the toric code, have already been quantum simulated using these methods [39, 40]. However, not all theories are suitable for quantum simulations. For example, the Wilson formulation of lattice gauge theory is based on classical degrees of freedom that lead to an infinite-dimensional Hilbert space on each link of the lattice which cannot be easily represented using quantum degrees of freedom.

In this thesis, we present results based on a class of lattice gauge theories as well as models in condensed matter physics, which are also suitable for quantum simulations. We will consider a toy model $U(1)$ lattice gauge theory and the quantum dimer model. We develop new algorithms, which allow us to shed light on the equilibrium physics of these systems. Additionally, our classical calculations can be used to validate future quantum simulators.

1.1 Quantum link models

Quantum link models were initially constructed by Horn in 1981 [41], and further investigated by Orland and Rohrlich [42, 43]. In [44] their potential as an alternative non-perturbative regularization of Abelian and Non-Abelian gauge theories was first realized by Chandrasekharan and Wiese. They realized that ordinary gauge fields emerge dynamically from the dimensional reduction of discrete quantum link variables. Dimensional reduction of discrete variables is a generic phenonmenon in asymptotically free theories, which gives rise to the D-theory formulation of quantum field theory [45]. In the D-theory formulation of 4-d quantum chromodynamics, the confining gluon field emerges by dimensional reduction from a deconfined Coulomb phase of a (4+1)-d $SU(3)$ quantum link model [46]. Chiral quarks arise naturally as domain wall fermions located at the two 4-d sides of a (4+1)-d slab. Additionally, quantum link models are also of interest in condensed matter physics. Apart from the quantum dimer models mentioned above, the (2+1)-d $U(1)$ quantum link model has also been investigated in the context of quantum spin liquids under the name of spin-ice models [25], and Kitaev's toric code [47] is a $\mathbb{Z}(2)$ quantum link model. Furthermore, it shares some similarity with the controversially discussed deconfined quantum criticality [48, 49, 50, 51, 52, 53, 54, 55, 56, 57, 58, 59]. This refers to a situation where a phase transition between different types of order is not of first order (as one would expect based on the Landau-Ginsburg-Wilson paradigm), but of second order. At the transition itself, a deconfined gauge boson emerges dynamically. In the (2+1)-d $U(1)$ quantum link model we encounter such a situation with different kinds of order, but with a (weakly) first order transition in-between. In addition, the transition point is

almost but not quite deconfined as the string tension does not vanish, even though it becomes rather small.

Quantum link models have a finite-dimensional Hilbert space per link, which makes them ideally suited for the construction of quantum simulators for Abelian [60, 33, 34, 61, 62, 63] and non-Abelian gauge theories [35, 36, 64, 37]. A long term goal of this research is to quantum simulate quantum chromodynamics in the D-theory formulation with ultracold matter, in order to address the problems mentioned above, including the real-time evolution of strongly interacting systems in nuclear and particle physics, as well as their dynamics at non-zero baryon density.

Moreover, the framework of quantum link models can be applied to other theories as well. In particular, the quantum dimer model is a $U(1)$ gauge theory which is equivalent to a quantum link model in a background of staggered charges. Even though a lot of progress has been made and despite the fact that it does not suffer from the notorious sign problem, quantum Monte Carlo calculations [65, 66, 67] were not able to provide conclusive results about its phase structure. However, the framework of quantum link models naturally leads to defining new order parameters that allow us to unambiguously distinguish the various candidate phases proposed in earlier works.

This thesis consists of a detailed description of our calculations and simulations for the (2+1)-d $U(1)$ quantum link [68, 69] and the (2+1)-d quantum dimer model [70, 71]. We will start with the definition of the (2+1)-d $U(1)$ quantum link model and its relation to Wilson's formulation of lattice gauge theory in chapter 2. Chapter 3 contains a description of the methods we used, namely exact diagonalization and a newly developed, efficient cluster algorithm, together with our results based on them. Our results lead to the formulation of an effective theory which will be the topic of chapter 4. The final part of this thesis addresses the quantum dimer model, where we performed similar calculations using the methods developed previously and managed to shed light on some controversial questions about its phase structure.

2 The (2+1)-d U(1) Quantum Link Model

In this chapter we will present a short introduction to the standard way of formulating quantum field theories in a non-perturbative way using the lattice regularization. It was originally invented by Kenneth G. Wilson [1] and is named after him. The standard approach is to define the theory using the Lagrangian formulation as is explained in many textbooks, like e.g. [72]. However, here we will not use this formulation, but the equivalent Hamiltonian theory. The reason for this is that the latter is a natural starting point for a generalization leading to quantum link models. As the chapter title suggests, the discussion will be limited to (2+1) dimensions and a $U(1)$ gauge group. After the introduction, the primary properties and symmetries of quantum link models are discussed, with the focus on the specific (2+1)-dimensional model that will be the topic of the rest of this thesis.

2.1 Wilson formulation of lattice gauge theory

Quantum field theories describe the behavior of all known fundamental fields and particles. For the purpose of this thesis, however, we are only concerned about the mediators of the fundamental forces, i.e. the gauge fields, and we will limit ourselves to the gauge group $U(1)$. Therefore we will provide a short introduction to the formulation of pure $U(1)$ gauge theories in $2+1$ dimensions using the lattice regularization.

Let us first start with the continuum formulation in Euclidean time. Its partition function can be written as

$$Z = \int \mathcal{D}A \, \exp\left(-\int d^3x \, \mathcal{L}\right), \tag{2.1}$$

where the Lagrangian is defined as

$$\mathcal{L} = \frac{1}{4e^2} F_{\mu\nu} F_{\mu\nu}. \tag{2.2}$$

As we are not concerned about fermions, the Lagrangian consists of the kinetic part of the gauge fields only, written in terms of the field strength tensor defined as

$$F_{\mu\nu}(x) = \partial_\mu A_\nu(x) - \partial_\nu A_\mu(x). \tag{2.3}$$

Here, $A_\mu(x)$ are the gauge fields, transforming as

$$A'_\mu(x) = A_\mu(x) + \partial_\mu \alpha(x) \tag{2.4}$$

under gauge transformations $\Omega(x) = \exp(ie\alpha(x)) \in U(1)$. Note that such a transformation leaves the Lagrangian $\mathcal{L}$ invariant.

This formulation is not fully defined yet as the integral measure $\mathcal{D}A$ is just a formal symbol for a product of uncountably many integrals. In order to rigorously define it, we need a regularization, either perturbatively or non-perturbatively. The only non-perturbative regularization known at the moment is the lattice regularization, where the space-time continuum is replaced by a discrete lattice. The theory is then fully defined by taking the limit of vanishing lattice spacing and infinite number of lattice points.

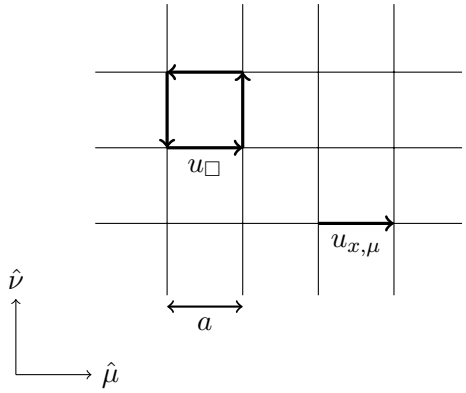

Figure 2.1: Basic building blocks of lattice gauge theory on a 2-dimensional slice of space-time.

Discretizing space-time is achieved by introducing a lattice spacing a between adjacent points and limiting their number in each direction to a finite number. This implies that also the gauge fields themselves are only defined on this subset. In Wilson's approach they are actually replaced by parallel transporters defined on the links between neighboring lattice sites, i.e. a link variable $u_{x,\mu} \in U(1)$ resides on the line connecting the point x to $x + a\hat{\mu}$ in the positive μ-direction (where $\hat{\mu}$ is a unit-vector in this direction) as shown in figure 2.1. They can, in principle, be constructed from the continuum gauge fields by taking the integral along the corresponding link, i.e.

$$u_{x,\mu} = P \exp\left(a \int_x^{x+a\hat{\mu}} ds\, A_\mu(s)\right). \tag{2.5}$$

However, it is important to note that, in the lattice formulation, the $u_{x,\mu}$ are actually the fundamental degrees of freedom and not quantities derived from a continuum field. Under gauge transformations these fields transform as

$$u'_{x,\mu} = \Omega_x u_{x,\mu} \Omega^\dagger_{x+a\hat{\mu}}, \quad \Omega_x = \exp(ie\alpha_x) \in U(1), \tag{2.6}$$

which yields in the continuum limit, after a short calculation involving a series expansion and

using continuum notation again,

$$u'_{x,\mu} = \mathbf{1} + a\Omega(x)\left[A_\mu(x) + \partial_\mu\right]\Omega(x)^\dagger + O(a^2) = \mathbf{1} + a\left[A_\mu(x) + \partial_\mu\alpha(x)\right] + O(a^2), \tag{2.7}$$

which corresponds up to order $O(a^2)$ to the continuum transformation properties of the gauge field shown in equation (2.4).

In order to define the theory, we need to construct a lattice action or, equivalently, Hamiltonian from gauge invariant quantities. The basic building blocks for this are closed loops of link variables. There are many ways of defining and combining such loops which differ by their convergence behavior with regards to the continuum limit (i.e. up to which order in a they correspond to the continuum action). The simplest variant is the one proposed by Wilson, which is defined in terms of elementary plaquette loops,

$$u_\square = u_{x,\mu}u_{x+a\hat{\mu},\nu}u^\dagger_{x+a\hat{\nu},\mu}u^\dagger_{x,\nu}. \tag{2.8}$$

An elementary plaquette is a closed loop around a square of four nearest neighbor points as depicted in figure 2.1.

In the Hamiltonian formulation (a derivation of which can be found e.g. in [73]), the lattice Hamiltonian becomes

$$H = \frac{e^2}{2}\sum_i e_{x,i}e_{x,i} - \frac{1}{2e^2}\sum_\square\left(u_\square + u^\dagger_\square\right), \tag{2.9}$$

where $e_{x,i} = -i\partial_{\varphi_{x,i}}$ (for $u_{x,i} = e^{i\varphi_{x,i}}$) are the electric field operators. Note that, from here on and for the rest of this thesis, we will set $a = 1$ for convenience. The fields obey the commutation relations

$$[e_{x,i}, u_{y,j}] = \delta_{xy}\delta_{ij}u_{x,i}, \tag{2.10}$$

$$[e_{x,i}, e_{y,j}] = 0. \tag{2.11}$$

Additionally, gauge invariance has to be ensured by a constraint on the Hilbert space of states, namely the Gauss law. This means that the generators G_x of local gauge transformations at a site x have to annihilate the wave function $|\psi\rangle$, i.e.

$$G_x|\psi\rangle = 0. \tag{2.12}$$

Together with the fact that the Hamiltonian commutes with G_x, this ensures that the allowed states are gauge invariant and therefore physical.

Note that the link variables $u_{x,i}$ are just complex numbers. Therefore, they commute among each other and we can write

$$[u_{x,i}, u_{y,j}] = 0. \tag{2.13}$$

However, this relation is actually of no formal relevance for the gauge symmetry and can therefore, in principle, be changed arbitrarily. This observation is the starting point for the construction of quantum link models, as will be explained in the next section.

2.2 The U(1) quantum link model in the spin $\frac{1}{2}$ representation

As mentioned in the previous chapter, quantum link models are a generalization of standard Wilson lattice gauge theory that differs only by the choice of degrees of freedom on the links between lattice sites. Formally, this means that the Hamiltonian can essentially be written in the exact same way, but using a different representation for the link degrees of freedom $U_{x,i}$. In the case we are interested in here, using the Abelian gauge group U(1), the Hamiltonian can be written as

$$H = \frac{J'}{2} \sum_{x,i} E_{x,i}^2 - \frac{J}{2} \sum_{\square} \left(U_{\square} + U_{\square}^{\dagger} \right), \tag{2.14}$$

where the $E_{x,i}$ still correspond to the generators of infinitesimal gauge transformations on a link (and are still quantum mechanical operators). The plaquette variables are again defined as

$$U_{\square} = U_{x,i} U_{x+\hat{i},j} U_{x+\hat{j},i}^{\dagger} U_{x,j}^{\dagger}. \tag{2.15}$$

The difference to Wilson's theory is that the complex-valued classical link variables $u_{x,i}$ have been turned into quantum links $U_{x,i}$, which are operators acting in a finite-dimensional local Hilbert space on each link. In order for the Hamiltonian to be gauge invariant, they should have the same transformation properties as their classical counterparts, i.e. they should transform as

$$U'_{x,i} = \exp\left(-i\alpha_x G_x\right) U_{x,i} \exp\left(i\alpha_x G_x\right) = \exp(i\alpha_x) U_{x,i}, \tag{2.16}$$

$$U'_{x,i} = \exp\left(-i\alpha_{x+\hat{i}} G_{x+\hat{i}}\right) U_{x,i} \exp\left(i\alpha_{x+\hat{i}} G_{x+\hat{i}}\right) = U_{x,i} \exp(-i\alpha_{x+\hat{i}}), \tag{2.17}$$

for local gauge transformations

$$G_x = \sum_i \left(E_{x,i} - E_{x-\hat{i},i} \right) \tag{2.18}$$

at a site x from the left or right, respectively. This is a consequence of demanding gauge-invariance of the Hamiltonian, i.e. for it to commute with gauge transformations,

$$[H, G_x] = 0. \tag{2.19}$$

Under a general gauge transformation $V = \prod_x \exp(i\alpha_x G_x)$, the link operators then transform as

$$U'_{x,i} = V^{\dagger} U_{x,i} V = \exp(i\alpha_x) U_{x,i} \exp(-i\alpha_{x+\hat{i}}). \tag{2.20}$$

From these properties, the commutator between the parallel transportation operators and the generators of gauge transformations become

$$[G_x, U_{y,i}] = (\delta_{x,y+\hat{i}} - \delta_{x,y}) U_{y,i}, \tag{2.21}$$

$$[G_x, U_{y,i}^{\dagger}] = (\delta_{x,y} - \delta_{x,y+\hat{i}}) U_{y,i}^{\dagger}. \tag{2.22}$$

Using the definition of G_x in terms of the infinitesimal generators $E_{x,i}$ (and their Hermiticity, $E^\dagger_{x,i} = E_{x,i}$), we obtain the commutation relations between the elementary operators $E_{x,i}$, $U_{x,i}$ and $U^\dagger_{x,i}$,

$$[E_{x,i}, U_{y,j}] = \delta_{x,y}\delta_{i,j}U_{x,i}, \tag{2.23}$$

$$[E_{x,i}, U^\dagger_{y,j}] = -\delta_{x,y}\delta_{i,j}U^\dagger_{x,i}. \tag{2.24}$$

As mentioned previously, the commutator of $U_{x,i}$ and $U^\dagger_{y,j}$ is actually not relevant for the gauge symmetry or other basic ingredients of the theory. Therefore, also the nature of the $U_{x,i}$ is still not clear. Classically, it could be written as $e^{i\phi_{x,i}} \in U(1)$. However, as there is no Hermitian operator that replaces a classical angle, we have to write this in a different form by replacing $\cos(\phi_{x,i})$ and $\sin(\phi_{x,i})$ with operators. Therefore we write

$$U_{x,i} = C_{x,i} + iS_{x,i}, \tag{2.25}$$

$$U^\dagger_{x,i} = C_{x,i} - iS_{x,i}. \tag{2.26}$$

With the above commutation relations, we can determine the relations between these new degrees of freedom,

$$[E_{x,i}, C_{y,j}] = i\delta_{x,y}\delta_{i,j}S_{x,i}, \tag{2.27}$$

$$[E_{x,i}, S_{y,j}] = -i\delta_{x,y}\delta_{i,j}C_{x,i}. \tag{2.28}$$

These actually resemble two of the three commutation relations of the $SU(2)$ algebra. Therefore it is natural to extend it also to the previously undefined relation between $C_{x,i}$ and $S_{x,i}$ and to set $[C_{x,i}, S_{y,j}] = i\delta_{x,y}\delta_{i,j}E_{x,i}$. By renaming the operators to

$$C_{x,i} = S^1_{x,i}, \qquad S_{x,i} = S^2_{x,i}, \qquad E_{x,i} = S^3_{x,i}, \tag{2.29}$$

the above commutation relations can then be written in the simple form

$$[S^k_{x,i}, S^l_{y,j}] = i\delta_{x,y}\delta_{i,j}\epsilon_{klm}S^m_{x,i}, \tag{2.30}$$

which corresponds to the conventional form an $SU(2)$ algebra. Therefore, the $U(1)$ quantum link model has a local Hilbert space that can be chosen to be any representation of $SU(2)$. This is the aforementioned feature of having a finite-dimensional Hilbert space per link, which is the main difference between Wilson's formulation and quantum link models. Additionally, we can now identify

$$U_{x,i} = C_{x,i} + iS_{x,i} = S^1_{x,i} + iS^2_{x,i} = S^+_{x,i}, \tag{2.31}$$

$$U^\dagger_{x,i} = C_{x,i} - iS_{x,i} = S^1_{x,i} - iS^2_{x,i} = S^-_{x,i}, \tag{2.32}$$

i.e. the link operators can be viewed as raising and lowering operators, respectively. Their commutation relation becomes

$$[U_{x,i}, U^{\dagger}_{y,j}] = 2\delta_{x,y}\delta_{i,j}E_{x,i}. \tag{2.33}$$

At this point, it is worth mentioning that one way to recover Wilson's formulation from the quantum link model is by taking an infinitely large representation of $SU(2)$ with integer spin. Practically, this would not gain us anything, though, and the way to go would be to use smaller representations and rely on the mechanism of dimensional reduction explained in [44] in order to obtain continuum physics. However, continuum limits are not the focus of this thesis and we will consider the simplest case possible as it already offers rich physics worth investigating.

The smallest possible representation of $SU(2)$ has spin $\frac{1}{2}$, where the generators are given by the Pauli matrices

$$\sigma_1 = \begin{pmatrix} 0 & 1 \\ 1 & 0 \end{pmatrix}, \qquad \sigma_2 = \begin{pmatrix} 0 & -i \\ i & 0 \end{pmatrix}, \qquad \sigma_3 = \begin{pmatrix} 1 & 0 \\ 0 & -1 \end{pmatrix}, \tag{2.34}$$

and where the Hilbert space becomes the direct product of local two-dimensional spaces on each lattice link. Analogously to a particular basis of ordinary $U(1)$ lattice gauge theory, we can work with quantized electric fluxes. In this case, $E_{x,i} = S^3_{x,i}$ is a diagonal operator giving the flux on a given link, while $U_{x,i}$ and $U^{\dagger}_{x,i}$ raise and lower the flux by one unit, respectively. The spin $\frac{1}{2}$ representation restricts us to two possible states per link, so we can have a flux of either $+\frac{1}{2}$ or $-\frac{1}{2}$, i.e. the flux is either flowing to the left (top) or right (bottom) on any link on a square lattice. This will be indicated by drawing an arrow on every link as illustrated in figure 2.2a.

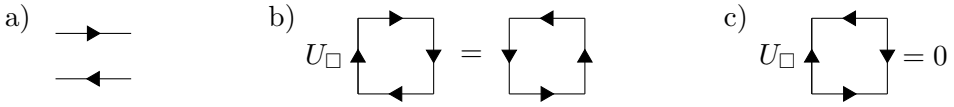

Figure 2.2: In the spin $\frac{1}{2}$ representation, we have two flux states per link with flux flowing either to the left / top (positive) or right / bottom (negative). The two states can be depicted as is shown here (a). The plaquette operator $U_\square$ changes the direction of a closed flux loop around an elementary plaquette (b) or annihilates plaquettes without flux loops (c).

The Hamiltonian (2.14) is written in terms of the two operators $E^2_{x,i}$ and $U_\square$. In the spin $\frac{1}{2}$ representation, the first one is actually just a constant because the allowed flux values are only $\pm\frac{1}{2}$. It can therefore be omitted. The second one operates on closed loops of flux around elementary plaquettes, flipping them from clockwise to counter-clockwise, while annihilating

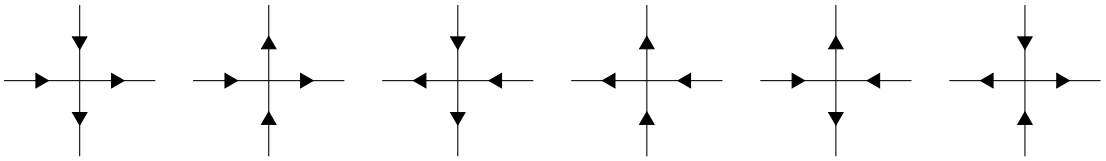

Figure 2.3: The six possible ways of fulfilling Gauss' law at a lattice site x in two dimensions.

all other configurations. Its Hermitian conjugate $U_\square^\dagger$ changes the flux in the opposite way, i.e. from counter-clockwise to clockwise, while also annihilating all other configurations. This behavior is illustrated in figure 2.2b,c.

In order to have more than one term (and another adjustable parameter apart from the scale-setting one from the first term), we are also adding one that counts the number of flippable plaquettes, i.e. the number of elementary plaquettes with a closed, circular flux around them. This is known as the Rokhsar-Kivelson (RK) term [10] and in our case it can be expressed as the square of the first term. The full Hamiltonian we are using can then be written as

$$H = -J \sum_\square \left[U_\square + U_\square^\dagger - \lambda \left(U_\square + U_\square^\dagger \right)^2 \right]. \tag{2.35}$$

One can convince oneself that the term proportional to λ indeed counts the number of flippable plaquettes by observing that $U_\square^2$ and $\left(U_\square^\dagger\right)^2$ annihilate any configuration on a plaquette. Therefore the only surviving term in the square is actually $U_\square U_\square^\dagger + U_\square^\dagger U_\square$. This yields a constant for any flippable plaquette and zero for every other configuration. Furthermore, with the spin $\frac{1}{2}$ representation, there is no additional higher order term of similar form because, as can be easily seen, all of those correspond to a product of a projection operator (i.e. higher orders of the λ term) with (odd powers) or without (even powers) an additional flipping of plaquettes.

The last missing piece for a fully defined model is the Gauss law. As explained in the previous chapter, in addition to a gauge invariant Hamiltonian, a gauge invariant theory needs to operate also on gauge invariant states, i.e. $G_x|\psi\rangle = 0$, unless we want to examine a system that contains additional static charges (which will be explained below). This is a consequence of charge conservation which follows from the familiar continuum Gauss law. In this case it means that at each site x, the in- and out-going fluxes have to add up to zero, i.e. there have to be as many arrows pointing to x as there are pointing away from x. There are six possible ways of realizing this in two dimensions which are shown in figure 2.3.

Additionally, we can place infinitely heavy, static charges on the lattice. This is done by locally changing the Gauss law at a given site x to

$$G_x|\psi\rangle = q_x|\psi\rangle, \qquad q_x \in \{-2, -1, 1, 2\}. \tag{2.36}$$

As the value of these charges is given by adding up the fluxes surrounding the lattice site, its values are restricted to integer numbers between -2 and 2, where the number 2 is due to the number of dimensions. Additionally, the total charge of a given configuration has to add up to zero, unless one considers non-periodic boundary conditions. Otherwise, no configurations fulfilling this variant of the Gauss law actually exist. Practically, these charges can be used to measure static properties like e.g. the energy of flux strings between charge-anticharge pairs. Moreover, as we will see in chapter 5, theories like the quantum dimer model can be expressed by a quantum link model living in a background of staggered charges ± 1. Figure 2.4 shows the allowed configurations corresponding to local charges ± 2 and ± 1 in two dimensions.

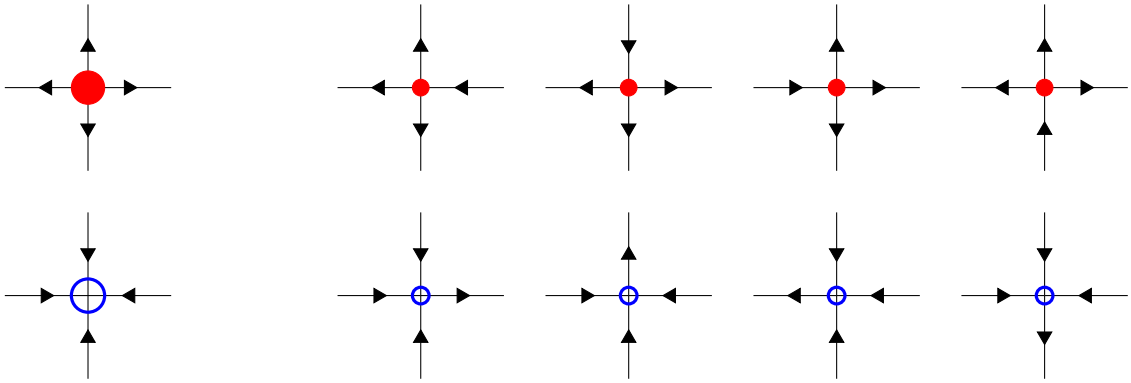

Figure 2.4: The two ways of placing a charge ± 2 (left) and the eight ways of placing a charge ± 1 (right) at a lattice site x in two dimensions.

Starting from here, we will be working with a 2-dimensional spatial lattice with volume $V = L_1 \times L_2$. Figure 2.5 shows a typical configuration on a 4×4 spatial lattice using periodic boundary conditions and fulfilling Gauss' law at every site.

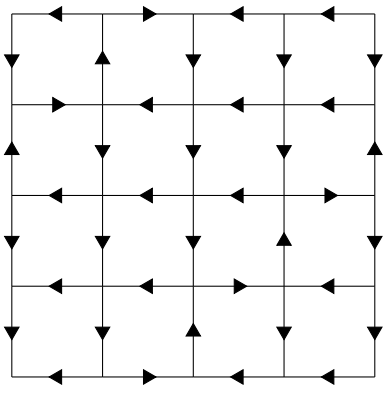

Figure 2.5: Typical configuration on a 4×4 lattice fulfilling the Gauss law in the flux representation of the link operators.

2.3 Symmetries

Apart from the gauge symmetry introduced in detail in the previous chapter, the (2+1)-d $U(1)$ quantum link model has the usual discretized space-time symmetries found in lattice theories. Depending on the boundary conditions, the existence of charges and the lattice geometry, these consist of translations by one lattice spacing in both directions, 90 degrees rotations around sites as well as around the center of plaquettes and reflections on either of the two axes. Additionally, the model has a charge conjugation symmetry and conserved global fluxes in either direction which are related to the $U(1)$ center symmetry. This section consists of a discussion of those symmetries that are relevant for the physical results presented later (which includes translations, charge conjugation, and the preserved fluxes).

2.3.1 Translations

In the continuum, infinitesimal translations are generated by the momentum operator $p_i = -i\partial_i$. On the lattice, however, only translations by multiples of the lattice spacing are possible and, with periodic boundary conditions, we return to the same state after either L_1 or L_2 translations, respectively. This reduces the symmetry from an $\mathbb{R}^2$ symmetry in the continuum down to a $\mathbb{Z}(L_1) \times \mathbb{Z}(L_2)$ on the lattice. We have

$$T_i^{L_i}|\psi\rangle = |\psi\rangle \tag{2.37}$$

where T_i is the unitary operator that translates the lattice by one unit in the i-direction. This implies a discretization of the eigenvalues as well. They correspond to the L_i-th roots of unity, i.e.

$$T_i|p\rangle = \exp\left(i\frac{2\pi n_i}{L_i}\right)|p\rangle \tag{2.38}$$

for a momentum eigenstate with momentum $p = \left(\frac{2\pi n_1}{L_1}, \frac{2\pi n_2}{L_2}\right)$.

Translations act on the relevant operators in the expected way, i.e.

$${}^{T_j}U_{x,i} = U_{x+\hat{j},i}, \qquad {}^{T_j}U^\dagger_{x,i} = U^\dagger_{x+\hat{j},i}, \qquad {}^{T_j}E_{x,i} = E_{x+\hat{j},i}. \tag{2.39}$$

2.3.2 Charge conjugation

Charge conjugation C transforms particles into anti-particles, changing charges to anti-charges and reversing fluxes. Written in terms of the fundamental degrees of freedom, this implies

$${}^{C}U_{x,i} = U^\dagger_{x,i}, \qquad {}^{C}U^\dagger_{x,i} = U_{x,i}, \qquad {}^{C}E_{x,i} = -E_{x,i}, \tag{2.40}$$

as well as

$$C^2|\psi\rangle = |\psi\rangle. \tag{2.41}$$

Therefore, the only immediately visible effect of charge conjugation on a given configuration is the flipping of all fluxes. As the square of the operator is equal to the trivial operator, charge conjugation has eigenvalues ± 1, and for an eigenstate we consequently get

$$C|\psi\rangle = \pm|\psi\rangle. \tag{2.42}$$

2.3.3 $U(1)$ center symmetry and conserved global fluxes

The center of the group $U(1)$ is $U(1)$ itself and leads to an additional symmetry that gives rise to super-selection sectors within the theory describing the total electric flux winding around the lattice in a given periodic spatial direction [74]. The generators are given by

$$E_i = \frac{1}{L_i} \sum_x E_{x,i}, \tag{2.43}$$

i.e. they correspond to adding up all the fluxes in one direction on a given line going through the dual lattice points. This is illustrated by the two dashed lines in figure 2.6. Additionally, these lines can be (locally) arbitrarily deformed because of Gauss' law.

It can be easily seen that these operators commute with the Hamiltonian because flipping a plaquette doesn't change the total flux on a given line. Additionally, the generators are diagonal in the flux basis, making the conserved flux a global property of a given configuration and every gauge-invariant configuration of fluxes is actually an eigenstate of it. Therefore, we have

$$E_i|\psi\rangle = n|\psi\rangle, \quad n \in \{-\frac{L_i}{2}, -\frac{L_i}{2}+1, \ldots, \frac{L_i}{2}\}, \tag{2.44}$$

for every allowed configuration and we will work in sectors with fixed flux. As an example, figure 2.6 shows part of the configuration of figure 2.5. We can now add up the fluxes crossed by either of the two dashed lines (except the last one, as this is just a copy of the first one due to periodic boundary conditions). This calculation results in a flux $E_y = -1$. It can be easily checked that both lines yield the same value and that this is also true for every other horizontal line in the configuration of figure 2.5.

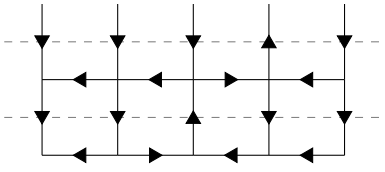

Figure 2.6: Example for the calculation of the overall flux of a configuration. The fluxes on either of the dashed lines have to be added up in order to obtain the total flux of -1 of this configuration.

As it corresponds to a certain electric flux winding around the lattice, states with higher flux in general have higher energies (at least for $\lambda < 1$, as will be explained in chapter 3) and therefore the groundstate is part of the flux sector with the lowest energy. While on lattices with an even extent in a given direction, the fluxes in this direction are integer valued, the ones in directions with an odd extent are half-integer valued. This implies that on lattices with at least one odd-length direction, a vanishing flux $(0, 0)$ is not possible, the flux sectors with the lowest energy become e.g. $(\pm\frac{1}{2}, 0)$ and are therefore degenerate. On even by even lattices (and $\lambda < 1$), the groundstate is non-degenerate as the zero-flux sector exists. Because of this, we will limit ourselves to lattices with even extents in both directions.

3 Numerical Methods and Results

This chapter describes the numerical methods used for solving the (2+1)-d $U(1)$ quantum link model in the spin $\frac{1}{2}$ representation together with the results produced with them. We use exact diagonalization to obtain the spectrum on small lattices. This provides qualitative insights into the phase structure already on rather small systems as will be explained below. Afterwards, a second method is discussed, which is based on a newly developed efficient quantum Monte Carlo cluster algorithm. As is shown, its results agree with and extend the exact diagonalization results. Both methods reveal a spontaneously broken, emergent symmetry at a quantum phase transition, which leads to the formulation of an effective theory that will be described in the next chapter.

3.1 Exact diagonalization

Exact diagonalization refers to calculating the energy spectrum of a theory, i.e. the eigenvalues and eigenfunctions of the Hamiltonian. This can be done either analytically or numerically. The first approach, however, quickly becomes impossible to apply, as larger lattice sizes imply large matrices for the Hamiltonian that cannot be diagonalized analytically anymore. The spectrum of these matrices can therefore only be calculated numerically. However, also for numerical calculations, the necessary operations for (exactly) diagonalizing the matrix needs an amount of time and memory that grows exponentially with the lattice size. Practically, this implies that on the largest system sizes accessible only the calculation of the lowest few states is actually possible. It is important to keep in mind though, that despite all this, the matrix is still implemented exactly, which means that the resulting spectrum is also exact, at least up to machine precision in the numerical values.

More precisely, calculating the eigenfunctions and eigenvalues of a Hamiltonian is a very difficult task on all but the smallest lattices because the dimension of the Hilbert space grows exponentially fast with the volume. In the case of the (2+1)-d quantum link model with the spin $\frac{1}{2}$ representation of $SU(2)$, we have one spin per link. Naively, for a volume $V = L_1 \times L_2$ we therefore have $2^{2L_1L_2}$ possible configurations.

Fortunately, an important realization to make is that different sectors of commuting symmetries can be considered separately, thereby decreasing the relevant matrix sizes significantly which allows reaching much larger lattices. The most important symmetry is actually the

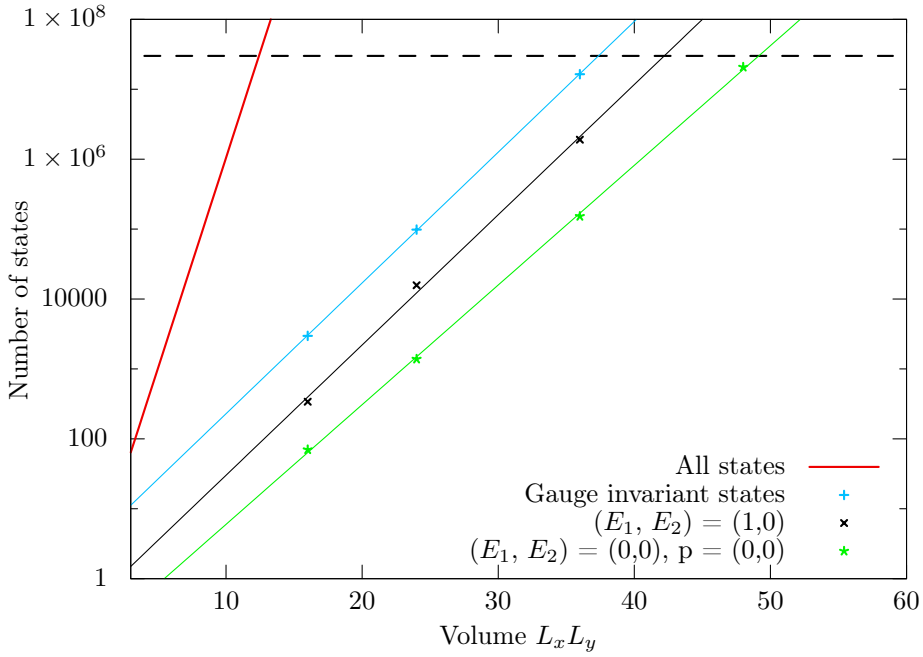

Figure 3.1: Number of states in different sectors of the $U(1)$ quantum link model. The dashed, horizontal line shows the approximate upper limit of current computational capabilities of our local computer cluster.

gauge symmetry itself. As explained previously, the Gauss law that follows from gauge invariance actually decreases the number of allowed states of the links directly connected to a site from $2^4 = 16$ down to just 6. Additionally, not all of these 6 states can actually reside on neighboring sites as they are connected by a common link thus restricting the number of allowed configurations even further.

Furthermore, the global symmetries offer some help in this as well. However, for this to work, we need to construct simultaneous eigenstates of all the symmetries whose different sectors we want to use. The task is therefore to find a maximal set of mutually commuting symmetry operators. For the $U(1)$ quantum link model, this is the combination of the $U(1)$ center symmetry together with the translation symmetry in each direction. As explained in section 2.3.3, the center symmetry leads to conserved fluxes in both directions. The number of these flux sectors is given by

$$N_i = V/L_i + 1, \tag{3.1}$$

for the flux in the i-direction. Therefore, in two dimensions this leads to a reduction of the order of the volume, if the flux in both directions is included. Similarly, it is possible to work with pre-generated momentum eigenstates, which lead to another reduction of similar order.

Figure 3.1 shows the number of states in several of the mentioned sectors together with a

dashed line indicating our (approximate) current computational capabilities with regards to matrix diagonalizations. The differences can easily be seen from this: Naively using all states without considering Gauss' law would limit us to volumes of around 12 lattice sites. Using just the Gauss' law allows us to already reach quite remarkable lattices sizes up to $V = 6 \times 6$. The combination of all the symmetries mentioned above actually raises the maximal lattice size to $V = 6 \times 8$. Further increasing this, however, seems unrealistic at the moment as the next useful lattice size is $V = 8 \times 8$ which is unreachable without further considerable improvements.

3.1.1 Technical aspects of exact diagonalizations

Exact diagonalization involves several steps and considerations of the memory usage together with the efficiency in terms of time duration are very important. This is because when trying to reach larger system sizes, the sizes of the matrices and vectors involved grow very quickly with the volume, as shown in figure 3.1. In general, the diagonalization begins by generating a list of all allowed basis states $|n\rangle$, $|m\rangle$ in the (symmetry) sector of interest, followed by the calculation of the Hamiltonian in matrix form, i.e. by calculating all non-zero matrix elements $\langle n|H|m\rangle$. This is followed by the diagonalization itself for which a number of well-established algorithms and libraries exist. This leads to a set of all (for small lattices) or the lowest few (for larger volumes) eigenfunctions and eigenvalues of the Hamiltonian, with which any desired observable or quantum number can be easily calculated. Some of the more critical considerations involved in these steps include the following:

- **Enumeration of allowed configurations:** As shown before, the number of all states grows exponentially fast with the volume which makes it practically impossible to naively generate those and then filter out the desired, gauge-invariant states only afterwards. A better approach is to use the Gauss law as much and as early as possible to generate only the subset of allowed configurations. This can be achieved by noting that choosing a certain state for a given site actually limits the number of possibilities for the surrounding sites, and constructing an algorithm that takes advantage of this. Furthermore, when working in the flux sectors related to the $U(1)$ center symmetry, it is possible to actually check for these much earlier than when an entire state is generated, because the Gauss law ensures that the flux flowing through every (straight) line wrapping the lattice in one direction is the same, as explained in section 2.3.3.

- **Momentum eigenstates:** Working with momentum eigenstates reduces the number of configurations by a factor comparable to the volume (for the $p = (0, 0)$ sector) or larger as all the configurations that differ from each other only by arbitrary numbers of translations in any direction are combined into one eigenstate. This reduces the matrix

size and it also lets one avoid saving all allowed configurations as it is sufficient to keep one representative configuration per basis state (as all the others can be trivially generated from this one by translations), which leads to large improvements of the speed and the memory consumption of the code.

- **Memory usage of configurations:** The $U(1)$ quantum link model with the spin $\frac{1}{2}$ representation has 2 states per link, which can be efficiently represented using a storage scheme based on one bit per link. In principle it would be possible to improve this even more by already taking into account Gauss' law. However, for our purposes this did not bring sufficiently significant improvements to be worth the difficulties in implementation. Additionally, this approach necessarily increases the computational power required.

- **Memory usage of matrices:** The only relevant matrix in terms of speed and memory consumption is the matrix of the Hamiltonian itself, because every other occurring matrix can be split into small, independent submatrices (by working in sectors defined by their energy eigenvalues). As the Hamiltonian operates only on flippable plaquettes, transitions from a particular configuration to another one are very much restricted and only a very limited number of them are possible. This implies that most matrix entries are actually zero. This can be taken into account by using a memory scheme suitable for sparse matrices, i.e. one that only keeps track of non-zero entries.

- **Calculation of operators:** From a performance point of view it is also very important to optimize the calculation of the action of an operator on a given state or configuration. This is true for all relevant operators, which in our case includes the Hamiltonian itself, translations and charge conjugations. Most of these consist of local updates which can be improved by taking advantage of the bit-based memory scheme. By writing bit-wise operations for these actions, it is possible to simultaneously change larger portions of the lattice, speeding up the calculation by a significant amount.

- **Parallelization:** Many parts, including the diagonalization of the Hamiltonian itself, involve steps that can easily benefit from using several threads to concurrently do the same operations on independent parts of the operands, e.g. by calculating different rows at the same time when performing the matrix multiplications necessary to diagonalize the Hamiltonian.

Table 3.2 shows some relevant statistics in terms of what we were able to reach with these optimizations for each of the two models considered, i.e. the quantum link model and the quantum dimer model (c.f. chapter 5). With the exponential growth of the Hilbert space, it seems unlikely that, given our local numerical resources, we can reach larger lattice sizes as the matrix size would increase by too much, making it impossible to store the entries in

	Quantum link model	**Quantum dimer model**
Max. lattice size	6×8	8×8
Max. matrix sizes	$20'792'698^2$	$33'490'432^2$
Max. # non-zero entries	$429'954'460$	$493'952'896$
Relative # non-zero entries	0.0001%	0.00004%

Figure 3.2: Relevant statistics for some of the properties of exact diagonalization.

memory. Even though it is theoretically possible, storing the matrix on a hard drive is not practical for performance reasons. It is worth noting, that the small relative amount of non-zero matrix entries is essential in being able to actually calculate eigenvectors of such large matrices.

Despite the smallness of the lattices, it is still possible to extract quite a lot of physical information from the spectrum in small volumes as will be shown in the next section.

3.2 Results from exact diagonalization

Exact diagonalization provides us with a lot of valuable information about the model already on small lattices. In this section, we will get an accurate picture of the phase diagram and we will be able to demonstrate indications of confinement. Additionally, first signs of the applicability of an effective theory emerge. This will allow accurate estimates of the critical value of the parameter λ using solely the effective theory and the exact diagonalization results in chapter 4.

3.2.1 Phase diagram

Exact diagonalization provides access to the eigenfunctions and their eigenvalues for every operator of interest. Even though the spectrum changes as a function of λ, it remains similar if λ is changed only slightly. This, together with a matching of the other quantum numbers described in section 2.3, allows us to identify how a given state changes as a function of the coupling. Figure 3.3 shows this for the relevant eigenstates that become the first excited state at some point. The energy gaps to the groundstate are given as functions of λ. In the part with $\lambda \lesssim -0.36$, the first excited state E_- almost degenerates with the groundstate and it has the quantum numbers $p = (\pi, \pi)$ and $C = -$. For $-0.36 \lesssim \lambda < 1$, a different state E_+ with quantum numbers $p = (\pi, \pi)$ and $C = +$ is almost degenerate with the groundstate. For $\lambda \geq 1$, the groundstate is exactly degenerate already in a finite volume and carries non-zero flux.

First, let us focus on values of $\lambda < 1$. Here figure 3.3 suggests possible spontaneous

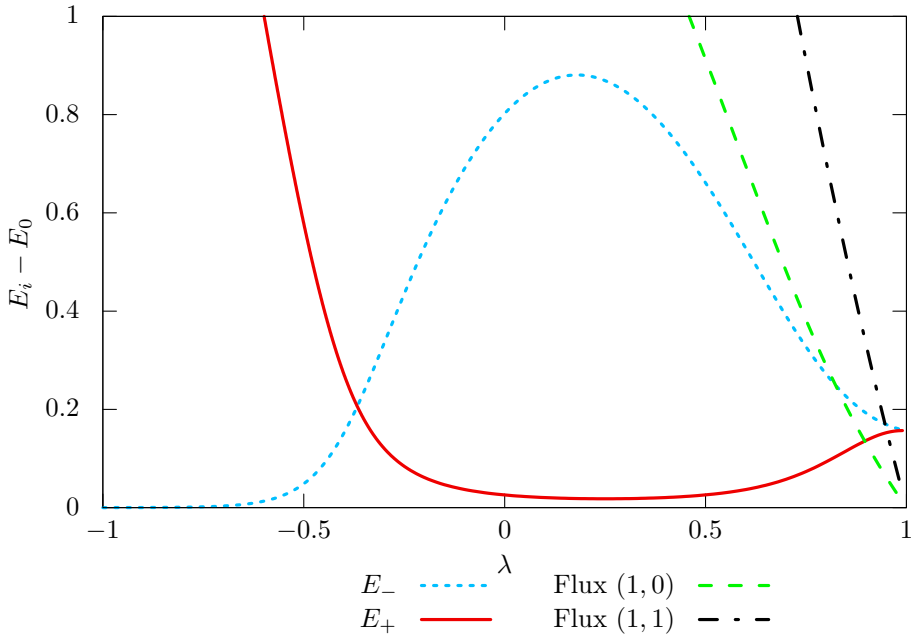

Figure 3.3: Energy gaps of the lowest lying energy eigenstates on the 6×8 lattice as a function of λ showing first hints of a phase transition around $\lambda_{pc} \approx -0.36$. Additionally, the deconfined RK point at $\lambda = 1$, where the energy of the flux states become zero, is clearly visible.

symmetry breaking, which would show up as a degenerate groundstate in the large volume limit. In a more formal way, the question is whether the gaps decay exponentially with the volume, i.e. whether the gap behaves as

$$E_1 - E_0 = A \exp\left(-\sigma L_x L_y\right). \tag{3.2}$$

Figure 3.4 shows a study of this in the two relevant regions, i.e. for $\lambda = -1$ and $\lambda = 0$. The plot is restricted to volumes $V \in \{4 \times 4, 4 \times 6, 6 \times 6, 6 \times 8\}$, i.e. to those that are larger than 2×2 and to (nearly) square lattices. The first condition is because the 2×2 lattice has only 16 gauge invariant states and therefore shows a rather different picture than larger volumes. The second restriction is due to the fact that elongated lattices show stronger finite size effects.

Clearly, on both sides of the crossing point $\lambda_{pc} \approx -0.36$ (where the subscript "pc" stands for "pseudo-critical", referring to the transition point on a finite lattice), one of the states with energies E_+ and E_- becomes degenerate with the groundstate while the other clearly does not, at least within the accuracy reachable by exact diagonalization. This suggests the spontaneous breaking of translation invariance and of the charge conjugation symmetry for $\lambda < \lambda_{pc}$, while for $\lambda_{pc} < \lambda < 1$ only translation invariance is spontaneously broken. Note that translations in either direction are broken, while their combination leaves the groundstate

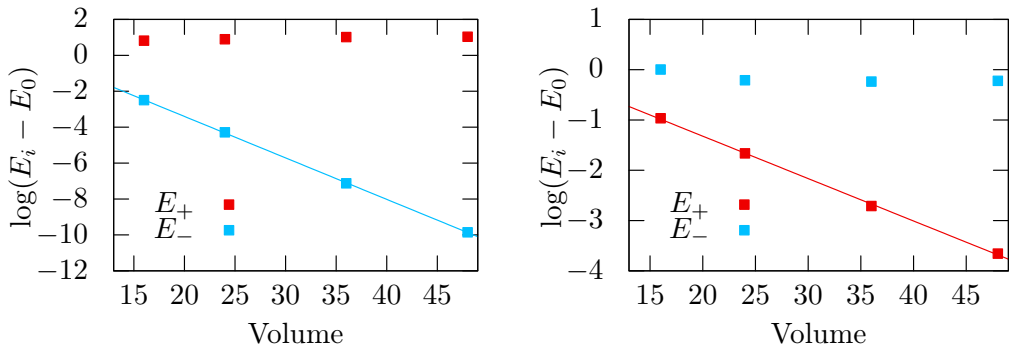

Figure 3.4: Energy gaps as a function of the volume for the two lowest lying states at $\lambda = -1$ (left) and $\lambda = 0$ (right). The colors of the states match with those from figure 3.3. Note, that in each plot only one of the gaps vanishes exponentially with the volume, while the other clearly converges to a finite value.

invariant. Additionally, figure 3.3 implies that it is not simply the case that translation invariance remains broken everywhere, while the charge conjugation symmetry gets restored at λ_{pc}. If this were the case, a state with non-zero momentum would remain degenerate with the groundstate. Here, however, the groundstate degenerates with a completely different state. Therefore, we have two distinct symmetry breaking patterns on either side of the transition.

3.2.2 Confinement

For values of $\lambda < 1$, the system is in a confined phase. This can be seen by examining the potential between two infinitely heavy, static charges as is shown in figure 3.5 (left). For $\lambda = 0$ this shows the behavior of the energy of a system with two charges as a function of their separation. A linearly rising potential is evident. In principle, the slope of this curve would yield the tension of the flux string between the charges. However, as we are using periodic boundary conditions, we are limited to distances of the order of half the lattices size. Therefore, the lattices reachable by exact diagonalization (with this method) are too small to really expect quantitative results for this.

Another way of looking at the same property is by considering states that include a flux string wrapping around the lattice as a function of the lattice extent in this direction. Figure 3.5 (right) shows the energy of such states relative to the groundstate on several lattices. The linear rise is again evident, showing the expected behavior for confinement already on these small lattices. For the cases where we can use both methods (i.e. for small L_y), we compare the slopes of the fits we obtain from both methods. Table 3.6 lists the (finite volume) string tensions σ resulting from the linear fits shown in figure 3.5. As expected, both methods agree

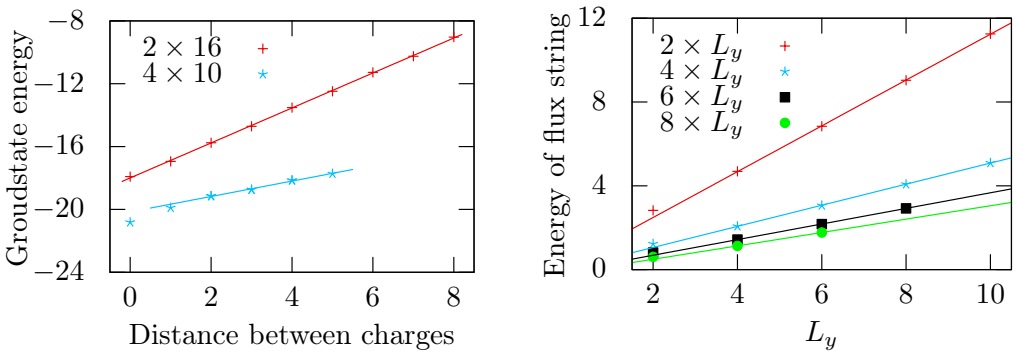

Figure 3.5: Groundstate energy E_0 on a 2×16 and a 4×10 lattice at $\lambda = 0$ for a system with a charge and an anti-charge as a function of the distance between the charges (left) and energy gap of the lowest flux state as a function of L_y on lattices with fixed $L_x \in \{2, 4, 6, 8\}$ at $\lambda = 0$ (right). The latter directly measures the energy of a flux string wrapping around the lattice.

within errors.

With the method based on flux strings wrapping the lattice, we can reach larger lattices and investigate what happens when we increase the size of the lattice perpendicular to the string. This shows the effects of squeezing the flux string and allows an extrapolation to infinitely wide lattices. Figure 3.7 shows the results of exponential fits at $\lambda = 0$ (based on the curves shown in figure 3.5 (right)) and at $\lambda = -1$. With these extrapolations we obtain values of $\sigma = 0.22 \pm 0.01, J/a$ at $\lambda = 0$ and $\sigma = 0.87 \pm 0.01\, J/a$ at $\lambda = -1$, respectively. In section 4.4.2 we will compare the values with the ones we obtain from simulations and the effective theory. Note though, that this is still based on very small lattices (and very short strings) and we don't expect these extrapolations to match exactly with the results we will obtain using the cluster algorithm. However, what can be seen already from this plot is that the finite volume estimate of the string tension changes by large factors as a function of the volume. This means that squeezing the string in a small periodic volume decreases the size of the string perpendicular to its direction, i.e. the string repels its periodic copy. This conclusion is further supported by numerical evidence showing that the tension of a string

	σ **from charges**	σ **from flux strings**
$2 \times Y$ **lattices**	$1.113 \pm 0.007\, J/a$	$1.092 \pm 0.008\, J/a$
$4 \times Y$ **lattices**	$0.49 \pm 0.02\, J/a$	$0.504 \pm 0.002\, J/a$

Figure 3.6: String tensions σ from linear fits to the exact diagonalization results on small lattices from fluxes between two charges and flux strings wrapping around the lattice, respectively.

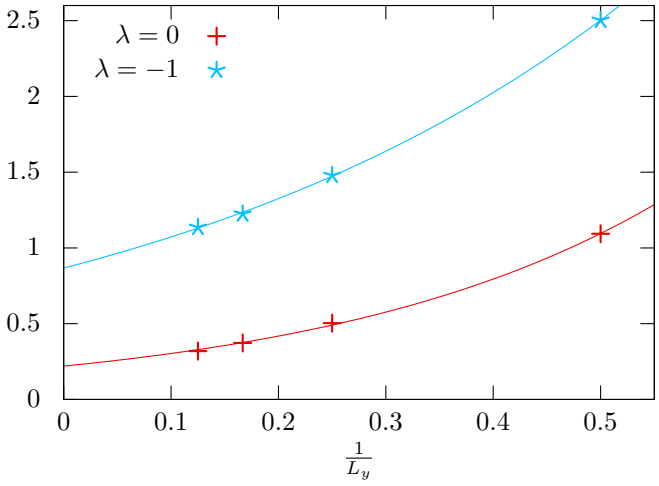

Figure 3.7: Exponential fits of the string tensions σ as a function of the lattice width in order to extrapolate to infinitely wide lattices for $\lambda = 0$ (based on the fits from figure 3.5) and $\lambda = -1$.

with flux two is more than twice as large as the one for a string with flux one.

Additionally, it is easy to see what happens with the string tension as a function of λ. For this we take another look at figure 3.3. It includes the energy gaps of the two lowest flux states. Both of them converge to zero at $\lambda = 1$. As we observe the same behavior on every lattice, this implies that the string tension approaches zero at the RK point, i.e. at $\lambda = 1$. This point is therefore deconfined. Additionally, it is exactly solvable, as the groundstate consists of an equal-weight superposition of all gauge-invariant states and has been studied extensively already (e.g. in [10, 15]).

3.2.3 Rotor spectrum

As explained above, the exact diagonalization results strongly suggest a phase diagram containing two distinct breaking patterns of the translation and charge conjugation symmetries with some kind of phase transition in between. As a next step, it is worthwhile to see what exact diagonalization can tell us about the transition itself. Figure 3.8 provides a more detailed picture of the lowest eigenstates with quantum numbers $p = (0, 0)$, $C = \pm$ or $p = (\pi, \pi)$, $C = \pm$, i.e. of those that share their quantum numbers with the presumed infinite volume groundstate. After the two states with energies E_+ and E_- already introduced in 3.3, the next relevant states have energies E'_+ and E'_- and charge conjugation parity $C = +$ and $C = -$, respectively, but their momentum vanishes, $p = (0, 0)$. Additionally, they have two crossing points λ'^{+}_{pc} and λ'^{-}_{pc} with $\lambda'^{-}_{pc} < \lambda_{pc} < \lambda'^{+}_{pc}$. Finally, the two states with energies E''_+ and E''_-, sharing a crossing point λ''_{pc}, again have the same quantum numbers as E_+ and E_-,

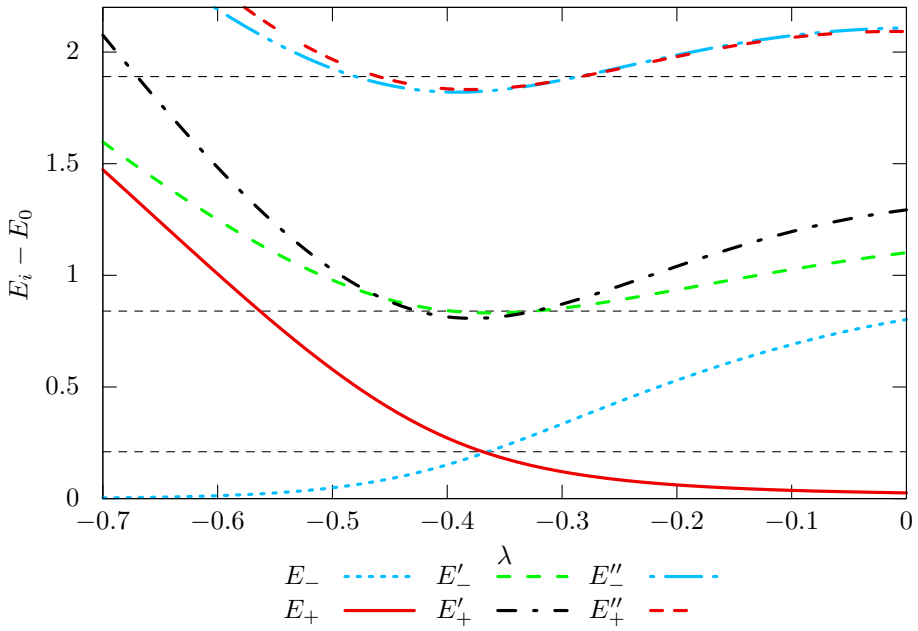

Figure 3.8: Energy gaps for the lowest states with momenta $p = (0, 0)$ or $p = (\pi, \pi)$ on a 6×8 lattice. The dashed lines have the ratios $1 : 4 : 9$, starting from the crossing points of the two lowest states, hinting at a rotor spectrum that will be explained by an effective theory.

i.e. $p = (\pi, \pi)$ and $C = \pm$. Interestingly, the crossing points follow a certain pattern: As indicated by the dashed lines in the plot, they follow the energy ratios $1 : 4 : 9$. A quantum mechanical system that shows a similar structure is the quantum rotor, i.e. a particle on a circle. Together with results presented in section 3.4, this observation will lead to the formulation of an effective theory valid near the phase transition in chapter 4.

3.3 Dualization, cluster algorithm and order parameters

As explained before, exact diagonalization is a powerful technique that allowed us to obtain valuable information about the phase structure of the model. However, due to the restriction to very small lattices, it is not possible to unambiguously extrapolate to large volumes. We will do this by using numerical simulations using a newly developed, efficient cluster algorithm that operates on height variables dual to the link variables introduced previously. We will start by calculating the transfer matrix in order to obtain the weights that will be needed to define the algorithm. Then the dual variables are explained, leading naturally to the algorithm itself. Finally, we will show the results obtained from simulations, which will provide detailed information about the phase structure of the model. Additionally, they will provide the

motivation for the formulation of the effective theory in the next chapter.

3.3.1 Construction of a path integral and the transfer matrix

As a starting point, we first calculate the elements of the transfer matrix in the flux basis defined previously. Starting with the Hamiltonian

$$H = -J \sum_{\square} \left[U_{\square} + U_{\square}^{\dagger} - \lambda \left(U_{\square} + U_{\square}^{\dagger} \right)^2 \right], \tag{3.3}$$

we define the partition function and the transfer matrix by

$$Z = \mathrm{tr} \left(e^{-\beta H} P_G \right) = \mathrm{tr} \left(T^{N_t} P_G \right), \tag{3.4}$$

where P_G is a projector onto the gauge invariant sector that ensures the fulfillment of Gauss' law. As usual, we used $\beta = \epsilon N_t$ to descretize the temporal direction. Calculating the transfer matrix elements suffers from the fact that for quantum link models the link variables on a given site do not commute among each other, $[U_{x,\mu}, U_{y,\nu}^{\dagger}] = 2\delta_{x,y}\delta_{\mu,\nu}E_{x,\mu} \neq 0$. Therefore, also neighboring plaquette variables $U_{\square}$ do not commute. This problem can be circumvented by Trotterizing the system, i.e. by splitting the lattice into an even (A) and an odd (B) sublattice, which each only contains mutually commuting plaquettes. This also splits the Hamiltonian into two parts, $H = H_A + H_B$. In each of those, all terms now commute among each other. This step is illustrated in figure 3.9.

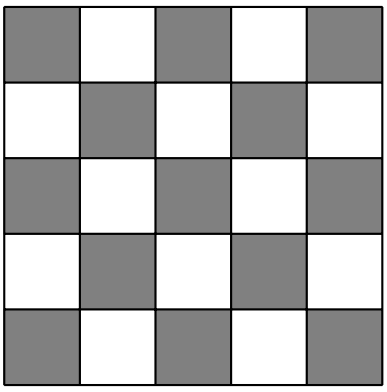

Figure 3.9: Trotterization: The lattice is split into two sublattices of mutually commuting plaquettes. Then the Hamiltonian can be split into two parts that consist only of commuting plaquettes. In a first step, only the shaded plaquettes on the even sublattice are active, while in the second step only the remaining white plaquettes on the odd sublattice contribute.

For $\epsilon \to 0$ and $N_t \to \infty$ with fixed $\beta = \epsilon N_t$, we can now write

$$Z = \mathrm{tr} \left(T^{N_t} P_G \right) = \mathrm{tr} \left[(T_A T_B)^{N_t} P_G \right], \tag{3.5}$$

where we defined $T_A = \exp(-\epsilon H_A)$ and $T_B = \exp(-\epsilon H_B)$. To simplify the notation, we introduce new symbols for the two plaquette operators in the Hamiltonian,

$$P_\square = U_\square + U_\square^\dagger, \tag{3.6}$$

$$P_\square^2 = \left(U_\square + U_\square^\dagger\right)^2. \tag{3.7}$$

As mentioned before, the first term flips flippable plaquettes, while the second term is a projection operator onto those plaquettes, which means that we have

$$(P_\square^2)^2 = P_\square^2, \qquad P_\square^3 = P_\square. \tag{3.8}$$

Considering the transfer matrix $T_X, X \in \{A, B\}$, on one of the two sublattices, we obtain

$$\begin{aligned} T_X &= \exp\left(\epsilon J \sum_{\square,X} \left[P_\square - \lambda P_\square^2\right]\right) \\ &= \prod_{\square,X} \exp\left(\epsilon J P_\square - \epsilon J \lambda P_\square^2\right) \\ &= \prod_{\square,X} \exp\left(\epsilon J P_\square\right) \exp\left(-\epsilon J \lambda P_\square^2\right), \end{aligned} \tag{3.9}$$

where products and sums are restricted to the X-sublattice (i.e. to either the even or the odd sublattice). We now consider the two exponential functions separately. The first one becomes

$$\begin{aligned} \exp\left(\epsilon J P_\square\right) &= 1 + \sum_{n=1}^{\infty} \frac{(\epsilon J)^n}{n!} P_\square^n \\ &= 1 + \sum_{n=1}^{\infty} \frac{(\epsilon J)^{2n+1}}{2n+1!} P_\square^{2n+1} + \sum_{n=1}^{\infty} \frac{(\epsilon J)^{2n}}{2n!} P_\square^{2n} \\ &= 1 + P_\square \sum_{n=1}^{\infty} \frac{(\epsilon J)^{2n+1}}{2n+1!} + P_\square^2 \sum_{n=1}^{\infty} \frac{(\epsilon J)^{2n}}{2n!} \\ &= 1 + P_\square \sinh(\epsilon J) + P_\square^2 \cosh(\epsilon J), \end{aligned} \tag{3.10}$$

where the third equality follows from equations (3.7) and (3.8). For the other term we get

$$\begin{aligned} \exp\left(-\epsilon J \lambda P_\square^2\right) &= 1 + \sum_{n=1}^{\infty} \frac{(-\epsilon J \lambda)^n}{n!} (P_\square^2)^n \\ &= 1 + P_\square^2 \sum_{n=1}^{\infty} \frac{(-\epsilon J \lambda)^n}{n!} \\ &= 1 + P_\square^2 (e^{-\epsilon J \lambda} - 1), \end{aligned} \tag{3.11}$$

where the second equality again follows from equations (3.7) and (3.8). With these we can now go ahead and calculate the transfer matrix for a single plaquette, which yields

$$\begin{aligned} T_\square &= \exp\left(\epsilon J P_\square\right) \exp\left(-\epsilon J \lambda P_\square^2\right) \\ &= \left[1 + P_\square^2 (e^{-\epsilon J \lambda} - 1)\right] \left[1 + P_\square \sinh(\epsilon J) + P_\square^2 \cosh(\epsilon J)\right] \\ &= 1 + P_\square e^{-\epsilon J \lambda} \sinh(\epsilon J) + P_\square^2 \left[e^{-\epsilon J \lambda} \cosh(\epsilon J) - 1\right]. \end{aligned} \tag{3.12}$$

From here we read off the matrix elements for the individual plaquettes. Non-flippable plaquettes only get a trivial diagonal element equal to unity. Flippable plaquettes on the other hand get two contributions. A diagonal one equal to the cosh term and an off-diagonal flipping term proportional to sinh. Symbolically, the non-trivial transfer matrix entries can be summarized as

$$\begin{aligned} \left\langle \right. \; \Big| \, T_\square \, \Big| \; \left. \right\rangle &= e^{-\epsilon J \lambda} \cosh\left(\epsilon J\right), \\ \left\langle \right. \; \Big| \, T_\square \, \Big| \; \left. \right\rangle &= e^{-\epsilon J \lambda} \cosh\left(\epsilon J\right), \\ \left\langle \right. \; \Big| \, T_\square \, \Big| \; \left. \right\rangle &= e^{-\epsilon J \lambda} \sinh\left(\epsilon J\right), \\ \left\langle \right. \; \Big| \, T_\square \, \Big| \; \left. \right\rangle &= e^{-\epsilon J \lambda} \sinh\left(\epsilon J\right). \end{aligned} \tag{3.13}$$

The whole single-plaquette transfer matrix then takes the form

$$\begin{pmatrix} e^{-\epsilon J \lambda} \cosh\left(\epsilon J\right) & e^{-\epsilon J \lambda} \sinh\left(\epsilon J\right) & 0 & 0 & 0 & 0 & 0 & 0 & 0 & 0 & 0 & 0 & 0 & 0 & 0 & 0 \\ e^{-\epsilon J \lambda} \sinh\left(\epsilon J\right) & e^{-\epsilon J \lambda} \cosh\left(\epsilon J\right) & 0 & 0 & 0 & 0 & 0 & 0 & 0 & 0 & 0 & 0 & 0 & 0 & 0 & 0 \\ 0 & 0 & 1 & 0 & 0 & 0 & 0 & 0 & 0 & 0 & 0 & 0 & 0 & 0 & 0 & 0 \\ 0 & 0 & 0 & 1 & 0 & 0 & 0 & 0 & 0 & 0 & 0 & 0 & 0 & 0 & 0 & 0 \\ 0 & 0 & 0 & 0 & 1 & 0 & 0 & 0 & 0 & 0 & 0 & 0 & 0 & 0 & 0 & 0 \\ 0 & 0 & 0 & 0 & 0 & 1 & 0 & 0 & 0 & 0 & 0 & 0 & 0 & 0 & 0 & 0 \\ 0 & 0 & 0 & 0 & 0 & 0 & 1 & 0 & 0 & 0 & 0 & 0 & 0 & 0 & 0 & 0 \\ 0 & 0 & 0 & 0 & 0 & 0 & 0 & 1 & 0 & 0 & 0 & 0 & 0 & 0 & 0 & 0 \\ 0 & 0 & 0 & 0 & 0 & 0 & 0 & 0 & 1 & 0 & 0 & 0 & 0 & 0 & 0 & 0 \\ 0 & 0 & 0 & 0 & 0 & 0 & 0 & 0 & 0 & 1 & 0 & 0 & 0 & 0 & 0 & 0 \\ 0 & 0 & 0 & 0 & 0 & 0 & 0 & 0 & 0 & 0 & 1 & 0 & 0 & 0 & 0 & 0 \\ 0 & 0 & 0 & 0 & 0 & 0 & 0 & 0 & 0 & 0 & 0 & 1 & 0 & 0 & 0 & 0 \\ 0 & 0 & 0 & 0 & 0 & 0 & 0 & 0 & 0 & 0 & 0 & 0 & 1 & 0 & 0 & 0 \\ 0 & 0 & 0 & 0 & 0 & 0 & 0 & 0 & 0 & 0 & 0 & 0 & 0 & 1 & 0 & 0 \\ 0 & 0 & 0 & 0 & 0 & 0 & 0 & 0 & 0 & 0 & 0 & 0 & 0 & 0 & 1 & 0 \\ 0 & 0 & 0 & 0 & 0 & 0 & 0 & 0 & 0 & 0 & 0 & 0 & 0 & 0 & 0 & 1 \end{pmatrix} \tag{3.14}$$

where the first two rows and columns correspond to the two flippable plaquettes with clockwise and counter-clockwise flux, respectively. The other rows and columns represent the remaining 14 non-flippable flux patterns on a plaquette.

Even though we can calculate the Boltzmann weights, formulating an efficient cluster algorithm in the flux basis remains a very challenging if not impossible task. Using a dualization procedure and going from a link basis to a plaquette basis greatly simplifies this. In the next section, we will explain this transformation of variables.

3.3.2 Dual height variables

In order to facilitate the formulation of a cluster algorithm, this section introduces the height variables that are used in the dual representation of the theory. In a 2-dimensional system, the link variables are replaced by dual site variables. The dual sites are located at the centers of the original plaquettes. Therefore, we go from link to plaquette variables. In standard $U(1)$ lattice gauge theory, the dual height variables can take any integer value. In quantum link models, the local link Hilbert space has finite dimension which implies a restriction of the allowed values for the height variables as well. They are restricted to two states per plaquette and the difference between neighboring height variables yields the flux of the link between them. In order to make this more explicit, we assign the values 0 and 1 for even dual sites and $\pm\frac{1}{2}$ for odd dual sites. The dual sites $\widetilde{x} = (x_1 + \frac{1}{2}, x_2 + \frac{1}{2})$ are located at the center of the plaquette to the upper right of a lattice site x. The transformation between height variables $h_{\widetilde{x}}$ and flux variables $E_{x,\mu}$ is given by

$$E_{x,\mu} = \left[h^{X}_{\widetilde{x}} - h^{X'}_{\widetilde{x}+\hat{1}+\hat{2}-i} \right] \mod 2 = \pm\frac{1}{2}, \tag{3.15}$$

where the superscripts X and X' refer to either the even or the odd sublattice. The modulo function is a generalization of the standard, integer-based modulo function, which works by adding or subtracting two until the result lies in the desired range $(-1, 1]$. Figures 3.10 and 3.11 show the possible combinations of height variables on neighboring sites and the resulting fluxes between them.

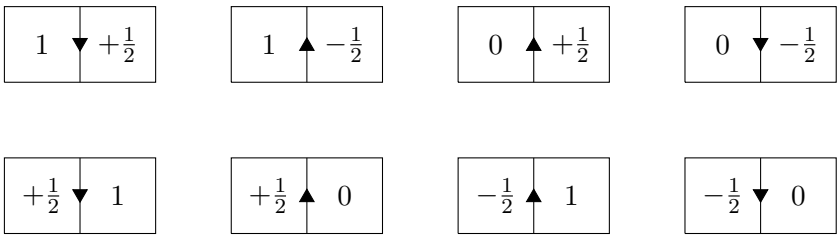

Figure 3.10: Relation between the height and the flux variables on even-odd (first row) and odd-even (second row) plaquette pairs.

Equation (3.15) clearly indicates that for each height configuration, there is exactly one associated flux configuration. The reverse, however, is not true. For every flux configuration satisfying the Gauss law (i.e. with zero net charge), there are exactly two corresponding

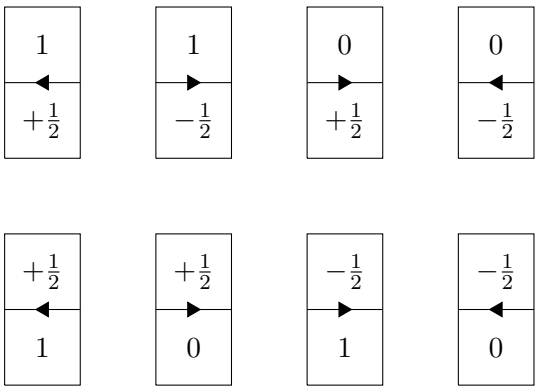

Figure 3.11: Relation between the height and the flux variables on even-odd (first row) and odd-even (second row) plaquette pairs.

height configurations which are related to each other by a total flip of all height variables as can be easily verified using equation (3.15). Additionally, it is not possible to find a height configuration around a site that has a net charge that is non-zero modulo two, i.e. charges ± 1 are not possible. As previously shown in figure 2.3, there are 6 flux configurations around a site that lead to zero net charge. Additionally, there is exactly one flux configuration that leads to charge 2 and one that leads to charge -2. Adding these together, there are 8 possible flux states with net charge 0 modulo 2. Taking the double-counting into account, these exactly correspond to the 16 possible configurations of height variables around a site as illustrated in figure 3.12 for even lattice sites.

3.3.3 Cluster algorithm

As shown in equation (3.13), the transfer matrix (and the Hamiltonian) acts non-trivially only on flippable plaquettes. Therefore we will formulate a cluster algorithm based on the dual height variables introduced in the previous section as they are already based on plaquettes. In the definition of the height variables we introduced a (somewhat) arbitrary distinction between the even and the odd sublattice. Because of this, we could then define them in such a way that the differences of neighboring heights directly correspond to the flux in-between (up to a modulo operation). Together with the Trotterization of the lattice, this leads to a system where we have integer valued (0 and 1) height variables on the even timeslices and half-integers ($\pm\frac{1}{2}$) on odd timeslices. Apart from this, there is no real difference between them. With this in mind, we will restrict ourselves in this section to plaquettes whose center lies on an odd site while the four surrounding height variables are therefore integer-valued. All the rules developed here apply also to the plaquettes on even sites by just switching even and odd height variables (i.e. by exchanging $0 \leftrightarrow -\frac{1}{2}$ and $1 \leftrightarrow +\frac{1}{2}$).

In order to construct an algorithm, we start by identifying flippable plaquettes in the

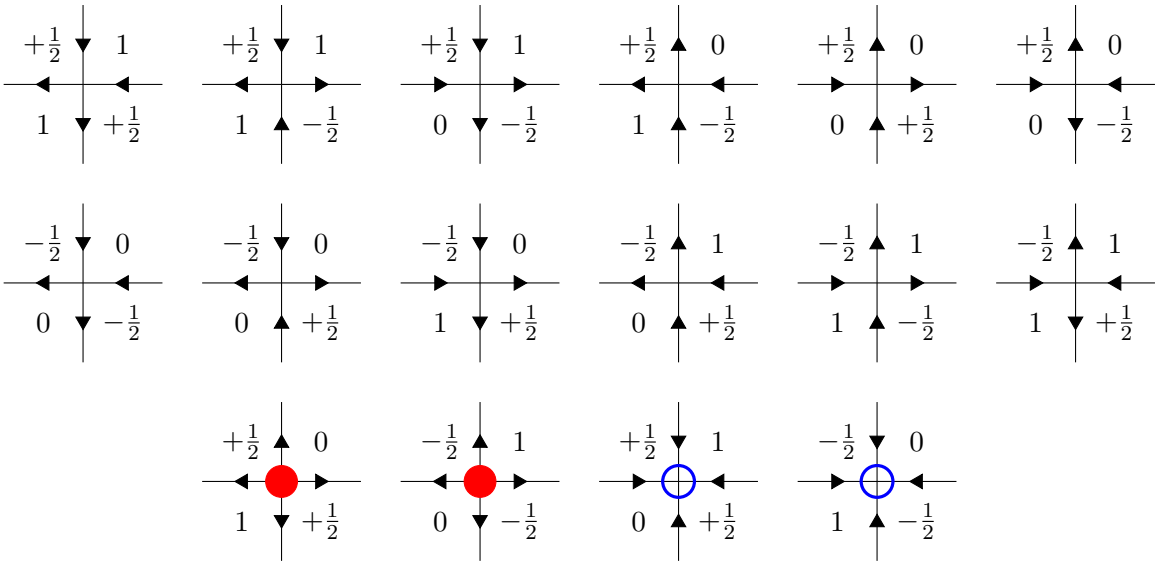

Figure 3.12: The 16 possible height configurations around an even lattice site and their corresponding flux configurations, showing the 2:1 relation between them. Additionally, the red (filled) and blue (empty) circles, indicate a net charge of plus and minus 2, respectively.

height variable formulation. Figure 3.13 illustrates the relation between flippable plaquettes of fluxes and their corresponding height patterns. Note again, that there are two height variable configurations for each flux configuration and that therefore there are four flippable configurations in the dual language equivalent to the two flux based configurations. The important observation here is that there is a flippable configuration if (and only if) the surrounding four height variables follow a given pattern that consists of two 1 and two 0 arranged in a certain way. In this configuration, flipping a plaquette then becomes a flip of the central height variable.

As previously mentioned, in the transfer matrix representation with height variables, when

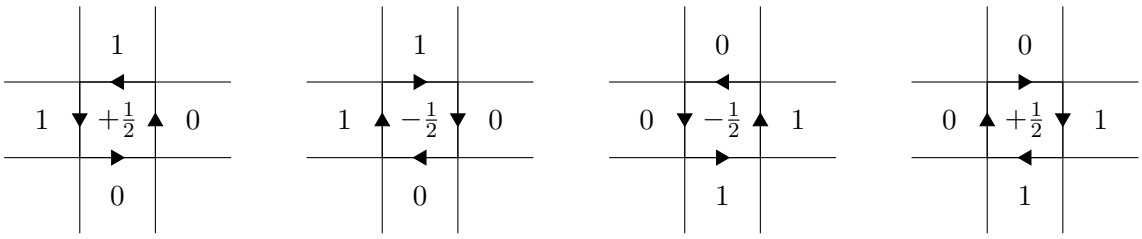

Figure 3.13: Height patterns associated with flippable plaquettes on the odd sublattice. Note again the doubling of states in the height representation compared to the flux representation.

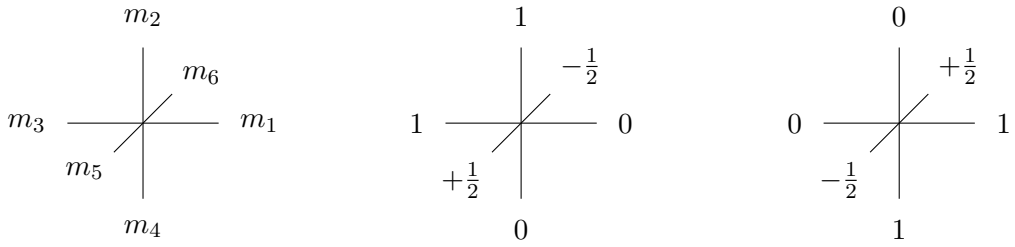

Figure 3.14: General representation of a plaquette on the timeslices from the transfer matrix representation with height variables. The height variables m_1, m_2, m_3 and m_4 reside in the timeslice t, while m_5 belongs to t-1 and m_6 to t+1 (left). The middle and the right figures show two possible transitions in which a plaquette is flipped (out of the four possibilities).

working with plaquettes, the relevant height variables reside on different timeslices. There are 6 different height variables involved in a transition, four of them living on one common timeslice (m_1 up to m_4), and one each in the previous (m_5) and the next (m_6) timeslice. This is illustrated in figure 3.14 on the left. The middle and the right figures show two (out of the four) possible transitions for a flippable plaquette that changes flux in a time step. In this language, a plaquette is flippable if the heights (m_1, m_2, m_3, m_4) are either $(1, 1, 0, 0)$ or $(0, 0, 1, 1)$. These two configurations are called the reference configurations. As flipping a plaquette is actually the only possible transition, it follows that if $m_5 \neq m_6$, then the other four heights have to be in one of the patterns of a flippable plaquette and the weight of the configuration is $e^{-\epsilon J\lambda} \sinh(\epsilon J)$. If $m_5 = m_6$, then all values for m_1, m_2, m_3 and m_4 are allowed, with a weight of $e^{-\epsilon J\lambda} \cosh(\epsilon J)$ if they are in a reference configuration and 1 otherwise.

Derivation of cluster rules

In order to formulate the cluster rules, let us consider the different cases. We start with the out-of-plane breakups, i.e. the question of whether or not to set a bond between m_5 and m_6 and therefore put them in the same cluster (and the probabilities for doing this). The first case (group m_5 and m_6 together) we call A, while B stands for keeping them separate.

- $m_5 = m_6$**, while** m_1**,** m_2**,** m_3 **and** m_4 **are not in a reference configuration:** This is the trivial case. The height variables m_5 and m_6 must be put together in a cluster as they have to retain the same value relative to each other (otherwise, we might generate a forbidden configuration where $m_5 \neq m_6$ without m_1, m_2, m_3, and m_4 being in a reference configuration). Therefore, in this case, there is no choice and we are always (with probability one) in case A.

- m_1, m_2, m_3 **and** m_4 **are in a reference configuration:** Here, two cases must be distinguished, either m_5 and m_6 have the same value or not. If they are different, the weight of the configuration is $e^{-\epsilon J\lambda}\sinh(\epsilon J)$ and we are in case B because otherwise we would generate a cluster that does not solely consist of a (temporally constant) reference configuration. If $m_5 = m_6$, the weight is $e^{-\epsilon J\lambda}\cosh(\epsilon J)$ and both A and B are possible, i.e. the weight is equal to $A + B$. Examples of both situations are depicted in figure 3.15. Therefore, we have

$$A + B = e^{-\epsilon J\lambda}\cosh(\epsilon J) \tag{3.16}$$

$$B = e^{-\epsilon J\lambda}\sinh(\epsilon J) \tag{3.17}$$

$$\Rightarrow \quad A = e^{-\epsilon J\lambda}\left[\cosh(\epsilon J) - \sinh(\epsilon J)\right] = e^{-2\epsilon J\lambda}. \tag{3.18}$$

The probabilities for choosing the A or B cluster break-up are then given by

$$P_A = \frac{A}{A+B} = \frac{e^{-\epsilon J\lambda}}{\cosh(\epsilon J)}, \tag{3.19}$$

$$P_B = \frac{B}{A+B} = \tanh(\epsilon J)\,. \tag{3.20}$$

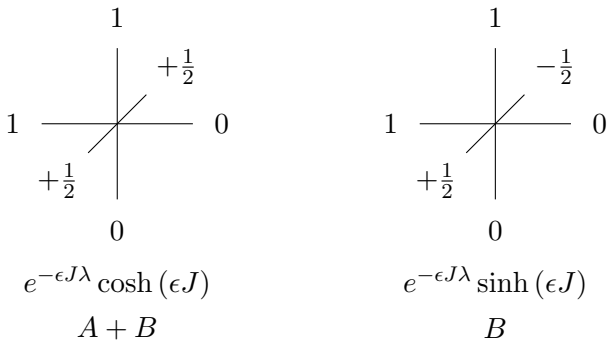

Figure 3.15: Example configuration for the case where m_1, m_2, m_3, and m_4 are in a reference configuration. On the left, m_5 and m_6 can either be bound into a cluster (A) or left separate (B). As calculated previously, this configuration has a weight of $e^{-\epsilon J\lambda}\cosh(\epsilon J)$. On the right, m_5 and m_6 have to be left separate (B) and the weight is $e^{-\epsilon J\lambda}\sinh(\epsilon J)$.

Next, we consider the in-plane breakups, i.e. we ask whether m_1, m_2, m_3, and m_4 are to be bound together (A) or left separate (B). We can again distinguish two cases:

- $m_5 \neq m_6$**:** This case implies that m_1, m_2, m_3, and m_4 have to be in a reference configuration and therefore we have to bind them together with probability one to avoid forbidden configurations.

- $m_5 = m_6$**:** There are again two cases. If m_1, m_2, m_3, and m_4 are in a reference configuration, the configuration has a weight $e^{-\epsilon J\lambda}\cosh(\epsilon J)$ and the four height variables can either be bound together (A) or left separate (B). Otherwise, the weight is 1 and the heights are not bound together (B). This situation is depicted in figure 3.16. Therefore, we have

$$B = 1 \tag{3.21}$$

$$A + B = e^{-\epsilon J\lambda}\cosh(\epsilon J) \tag{3.22}$$

$$\Rightarrow \quad A = e^{-\epsilon J\lambda}\cosh(\epsilon J) - 1. \tag{3.23}$$

The corresponding probabilities are then given by

$$P_A = \frac{A}{A+B} = 1 - \frac{e^{\epsilon J\lambda}}{\cosh(\epsilon J)}, \tag{3.24}$$

$$P_B = \frac{B}{A+B} = \frac{e^{\epsilon J\lambda}}{\cosh(\epsilon J)}. \tag{3.25}$$

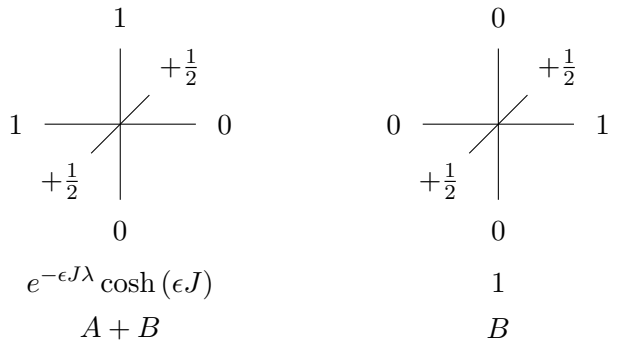

Figure 3.16: Example configuration for the case where $m_5 = m_6$. On the left, m_1, m_2, m_3 and m_4 are in a reference configuration and can either be bound into a cluster (A) or left separate (B). This configuration again has a weight of $e^{-\epsilon J\lambda}\cosh(\epsilon J)$. On the right, m_5 and m_6 have to be left separate (B) and the weight is $e^{-\epsilon J\lambda}\sinh(\epsilon J)$.

This covers all the cluster rules directly related to the action of the Hamiltonian. The only missing part is related to the Gauss law. As shown in figure 3.12, the height representation already ensures the Gauss law mod 2, i.e. it is impossible to generate configurations with charges ± 1. However, we still need to exclude the four configurations with charge ± 2. As the Gauss law is site-based, the rules depend again on sites on both sublattices. Figure 3.17 shows on the left the structure we are using. The A_i reside on one sublattice, while the B_i are part of the other one. What has to be done is most obvious, if one compares the height variables of the reference configuration (top row) with the ones leading to charge ± 2 (bottom

row). The reference configurations have a pattern such that diagonally from lower left to upper right, the height variables do not change their values, while they change from upper left to lower right. In all configurations leading to charge ± 2, both of these patterns are violated, i.e. these configurations are out of the reference configuration on both sublattices. Therefore, ensuring Gauss' law is equivalent to making sure that we never generate a situation where both sublattices are out of the reference configuration locally around a site. So for each of those sites on the active sublattice, we have to check whether the corresponding sites of the inactive sublattice are out of the reference configuration. If this is the case, we bind the two sites on the active lattice together in order to ensure that they stay in the reference configuration. As usual, it is enough to ensure these rules only on one complete timeslice, i.e., as we split the two sublattices, on one even and one odd timeslice.

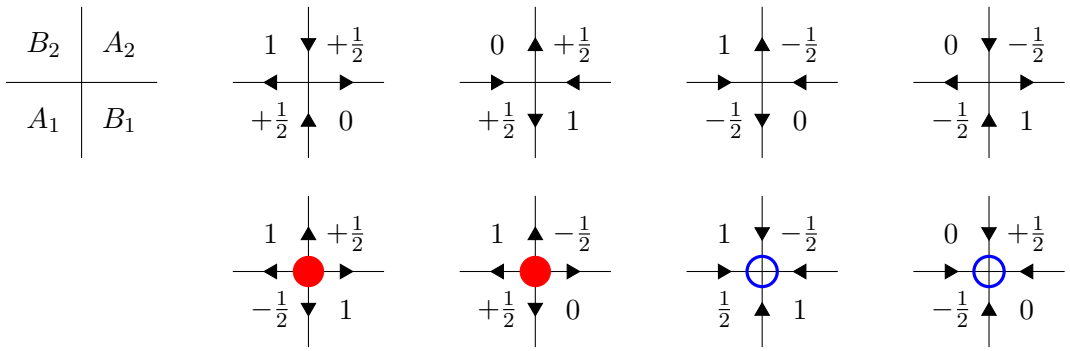

Figure 3.17: Name scheme of height variables around a lattice site (left most) together with a comparison between the reference configurations (top row) and configurations with charge ± 2 (bottom row) at a lattice site.

The cluster algorithm

After having derived all the rules, the complete (multi-cluster) algorithm proceeds as follows:

1. Set out-of-plane bonds for each pair of heights living on adjoining even timeslices (i.e. define which height variables are part of the same cluster) using the rules derived above (the names of the height variables again refer to figure 3.14):
   - If m_1, m_2, m_3, and m_4 are not in a reference configuration (i.e. they are not in one of the configurations in figure 3.14 on the left), m_5 and m_6 are bound together.
   - If m_1, m_2, m_3, and m_4 are in a reference configuration and $m_5 = m_6$, the latter are put in the same cluster with probability $p_A = \frac{e^{-\epsilon J \lambda}}{\cosh(\epsilon J)}$.
   - Otherwise, no bond is put between m_5 and m_6.

2. Set in-plane bonds for each set of heights arranged like m_1, m_2, m_3 and m_4 in figure 3.14 living on the same even timeslice:
   - If $m_5 \neq m_6$, put m_1, m_2, m_3, and m_4 in a common cluster
   - If $m_5 = m_6$, while m_1, m_2, m_3, and m_4 are in a reference configuration, then m_1, m_2, m_3 and m_4 are bound together with probability $P_A = 1 - \frac{e^{\epsilon J \lambda}}{\cosh(\epsilon J)}$.
   - Otherwise, m_1, m_2, m_3, and m_4 remain independent.
3. For one even timeslice (e.g. the first one), check whether bonds have to be set due to the Gauss law (using the notation of figure 3.17):
   - If for even height variables A_1 and A_2, we have $B_1 = B_2$, then bind A_1 and A_2 together.
   - If for even height variables B_1 and B_2, we have $A_1 \neq A_2$, then bind B_1 and B_2 together.
4. For each cluster, i.e. each independent set of height variables connected by bonds, flip all values with a fifty percent probability.
5. Repeat the steps 1 to 4 for the other half of the lattice, i.e. replacing "even" with "odd".

As usual, this algorithm describes one sweep and is repeated until a sufficient amount of data is accumulated. Starting from a configuration in a given charge sector, i.e. with a fixed distribution of charges ± 2, this algorithm ensures that we stay in this sector. In particular, if we start without charges, then the algorithm will never leave the zero-charge sector. Note that the total charge of the whole configuration has to be equal to zero, because otherwise there will be no allowed configurations.

3.3.4 Order parameters

Since we have identified two reference configurations, it is natural to define order parameters that measure the overlap of a given configuration with one of these reference configurations. As they are defined on each sublattice individually, we obtain two order parameters which we call M_A and M_B on the even (A) and odd (B) sublattice, respectively. These two "magnetizations" can be defined as

$$M_X = \sum_{\widetilde{x} \in X} s^X_{\widetilde{x}} h^X_{\widetilde{x}}, \quad X \in \{A, B\}, \tag{3.26}$$

where

$$s^A_{\widetilde{x}} = \frac{1}{2}\left((-1)^{(\widetilde{x}_1 - \widetilde{x}_2)/2} - 1\right), \qquad s^B_{\widetilde{x}} = (-1)^{(\widetilde{x}_1 - \widetilde{x}_2 + 1)/2}. \tag{3.27}$$

The additional factors in $s^A_{\widetilde{x}}$ compared to $s^B_{\widetilde{x}}$ are there in order to include the different definitions of height values on the even and odd sublattice while still having a common normalization for both M_A and M_B. Note that $\pm(M_A, M_B)$ represent the same physical flux configuration, because shifting the height variables to $h^{X'}_{\widetilde{x}} = [h^X_{\widetilde{x}} + 1] \mod 2$ leaves the electric flux configuration unchanged.

As shown in section 3.2, we are most interested in the spontaneous breaking of the translation and charge conjugation symmetries. In order to obtain the behavior of the order parameters under these, let us first consider the changes to the height variables. Charge conjugation inverts the direction of every flux. In the height language, this implies that only the variables on one of the two sublattices get flipped, i.e.

$$ {}^c h^A_{\widetilde{x}} = h^A_{\widetilde{x}}, \qquad {}^c h^B_{\widetilde{x}} = -h^B_{\widetilde{x}}. \tag{3.28} $$

This follows from the fact that the flux is directly related to the difference between the two adjoining height variables. Translations on the other hand, move the whole lattice by one lattice spacing. Clearly, this also exchanges the two dual sublattices, i.e.

$$ {}^T h^A_{\widetilde{x}} = h^B_{\widetilde{x}} + \frac{1}{2}, \qquad {}^T h^B_{\widetilde{x}} = h^A_{\widetilde{x}} - \frac{1}{2}. \tag{3.29} $$

Using these properties together with the definitions of the order parameters yields

$$ {}^C M_A = M_A, \qquad {}^C M_B = -M_B, \tag{3.30} $$

$$ {}^T M_A = -M_B, \qquad {}^T M_B = M_A. \tag{3.31} $$

These transformation properties make it clear that it is not useful to consider M_A and M_B individually, but to interpret them as the components of a two-dimensional vector. In this space, charge conjugation is equivalent to a reflection on the M_A axis, while a translation is equivalent to a counter-clockwise rotation by $\frac{\pi}{2}$. This is illustrated in figure 3.18.

The results from exact diagonalization indicate that the (2+1)-d quantum link model spontaneously breaks the translation and the charge conjugation symmetry in two distinct patterns. This implies that a probability distribution of (M_A, M_B) will show certain peaks as it has to change under these transformations between the different groundstates. Figure 3.19 illustrates how the two symmetry breaking patterns would show up in the peak structure of (M_A, M_B) plots. Keeping in mind that (M_A, M_B) and $-(M_A, M_B)$ actually represent the exact same flux state, we can see that the plot on the left is neither invariant under reflections on an axis (charge conjugation) nor under rotations by $\frac{\pi}{2}$ (translation). Either of these operations changes the system into a different phase, which is what we expect to happen in a system that spontaneously breaks both symmetries. In the situation on the right, rotations by $\frac{\pi}{2}$ still change the system into a different phase. However, reflections just invert the sign of the (M_A, M_B) vector and thus does not change the state, i.e. it shows a state where the translation symmetry is spontaneously broken, while charge conjugation remains unbroken.

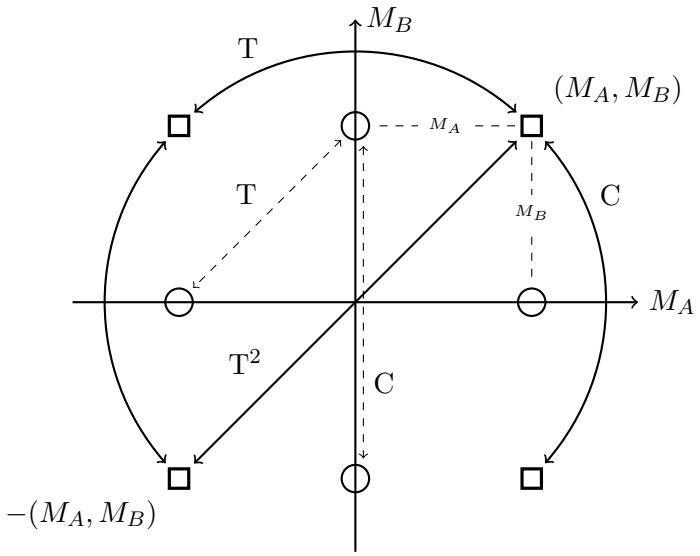

Figure 3.18: The effect of the symmetry transformations C and T on the two-component order parameter (M_A, M_B). The former is equivalent to a reflection on the M_A axis, while the latter is an anti-clockwise rotation by $\frac{\pi}{2}$. Performing the translation twice is equivalent to rotating by π, and leads back to the starting configuration, since $-(M_A, M_B)$ is an equivalent copy of (M_A, M_B).

3.3.5 Energy density and potential energy calculation

The energy density is given by

$$\mathcal{E} = -\frac{1}{L^2}\frac{\partial \ln Z}{\partial \beta} = -\frac{1}{L^2 N_t}\frac{\partial \ln Z}{\partial \epsilon} = -\frac{1}{L^2 N_t}\frac{1}{Z}\frac{\partial Z}{\partial \epsilon}, \tag{3.32}$$

where we used $\beta = \epsilon N_t$. As we have seen before, the partition function can be expressed through the transfer matrix shown in equation (3.13), consisting of the product of local 4-link (in the flux basis) or 6-height-variable interactions. The non-zero elements are given by

$$P_1 = e^{-\epsilon J \lambda}\cosh(\epsilon J) \qquad \text{(Unchanged flippable plaquette)}, \tag{3.33}$$

$$P_1 = e^{-\epsilon J \lambda}\sinh(\epsilon J) \qquad \text{(Flipped plaquette)}, \tag{3.34}$$

$$P_3 = 1 \qquad \text{(Otherwise)}. \tag{3.35}$$

Therefore, the energy density becomes a sum of such terms, i.e.

$$\mathcal{E} = -\frac{1}{L^2 N_t}\frac{1}{Z}\frac{\partial Z}{\partial \epsilon} = -\frac{1}{L^2 N_t}\left\langle \sum_k \frac{1}{P_k}\frac{\partial P_k}{\partial \epsilon} \right\rangle. \tag{3.36}$$

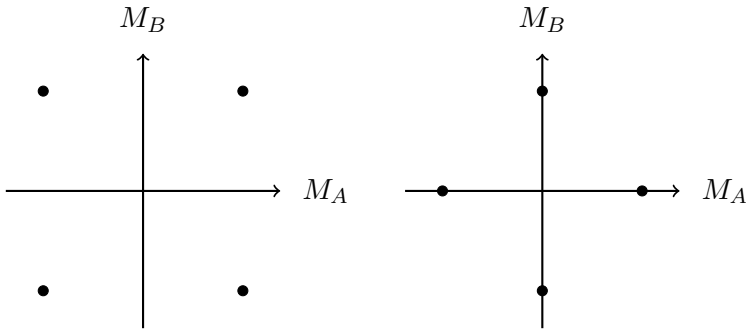

Figure 3.19: Expected patterns of the two-dimensional order parameter (M_A, M_B) for spontaneously broken charge conjugation and translation symmetry (left) and translation symmetry (right). Note that, as expected, these patterns change under the transformations associated with these symmetries, i.e. under 90 degree rotations for the translation symmetry and reflections on the M_A axis for the charge conjugation symmetry (left figure only).

The relevant logarithmic derivatives are

$$\begin{aligned}
\frac{1}{P_1}\frac{\partial P_1}{\partial \epsilon} &= \frac{J}{e^{-\epsilon\lambda}\cosh(\epsilon J)}\left[-\lambda e^{-\epsilon J\lambda}\cosh(\epsilon J) + e^{-\epsilon J\lambda}\sinh(\epsilon J)\right] \\
&= -J\lambda + J\tanh(\epsilon J), \\
\frac{1}{P_2}\frac{\partial P_2}{\partial \epsilon} &= \frac{J}{e^{-\epsilon\lambda}\sinh(\epsilon J)}\left[-\lambda e^{-\epsilon J\lambda}\sinh(\epsilon J) + e^{-\epsilon J\lambda}\cosh(\epsilon J)\right] \\
&= -J\lambda + J\coth(\epsilon J), \\
\frac{1}{P_3}\frac{\partial P_3}{\partial \epsilon} &= 0.
\end{aligned} \tag{3.37}$$

In order to calculate the energy density, we therefore have to go through all 6-height-variable interactions and check whether they are in a reference configuration with $m_5 = m_6$ (P_1) or in one that flips from one timeslice to the next ($m_5 \neq m_6$, P_2) and add up the appropriate value (or keep track of the factors for each plaquette separately to obtain the local energy density).

Similarly, the potential energy density is given by

$$\mathcal{E}_p = -\frac{1}{L^2 N_t}\frac{1}{Z}\frac{\partial Z}{\partial(\epsilon\lambda)}. \tag{3.38}$$

The non-zero transfer matrix elements become

$$\begin{aligned}
P_1 &= e^{-J\epsilon\lambda}\cosh(\epsilon J) \qquad &&\text{(Unchanged flippable plaquette)}, \\
P_1 &= e^{-J\epsilon\lambda}\sinh(\epsilon J) \qquad &&\text{(Flipped plaquette)}, \\
P_3 &= 1 \qquad &&\text{(Otherwise)},
\end{aligned} \tag{3.39}$$

and the derivatives become

$$\begin{aligned}
\frac{1}{P_1}\frac{\partial P_1}{\partial(\epsilon\lambda)} &= -J\frac{e^{-\epsilon\lambda}\cosh(\epsilon J)}{e^{-\epsilon\lambda}\cosh(\epsilon J)} = -J, \\
\frac{1}{P_2}\frac{\partial P_2}{\partial(\epsilon\lambda)} &= -J\frac{e^{-\epsilon\lambda}\sinh(\epsilon J)}{e^{-\epsilon\lambda}\sinh(\epsilon J)} = -J, \\
\frac{1}{P_3}\frac{\partial P_3}{\partial(\epsilon\lambda)} &= 0.
\end{aligned} \tag{3.40}$$

Therefore, the potential energy density is (not surprisingly) just the sum of factors of $-J$ for each flippable plaquette.

3.4 Results from numerical simulations

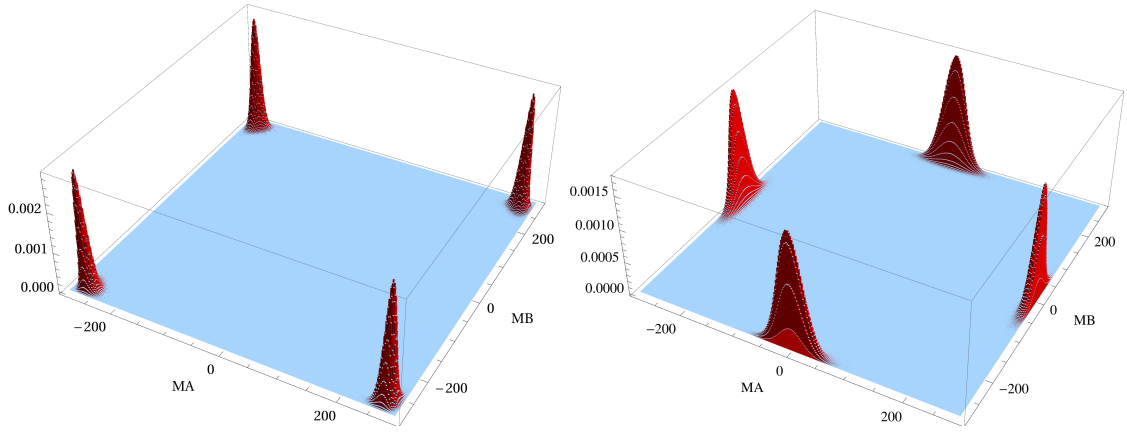

Figure 3.20: Probability distribution $p(M_A, M_B)$ for $\lambda = -1$ (left) and 0 (right) at $T = 0$ on an $L_x \times L_y = 24 \times 24$ lattice.

As a first step, we can compare the results obtained by exact diagonalization with those from the cluster algorithm. Exact diagonalization led us to conclude that there are two distinct symmetry breaking patterns separated by a phase transition. In order to investigate the different phases we consider probability distributions of the order parameters $p(M_A, M_B)$. Figure 3.20 shows the results for this observable. As expected, it is consistent with our previous results and agrees with what we conjectured in figure 3.19. For $\lambda < \lambda_c$, we observe four peaks situated in the corners of the two-dimensional space. This means that both sublattices are in one of the reference configurations, i.e. both of them are ordered, the system is maximally ordered. This pattern clearly shows that charge conjugation as well as the translation symmetries are spontaneously broken. For larger values of λ, i.e. larger than $\lambda_c \approx -0.36$, the pattern is different: The four peaks are now arranged on the axes. Therefore, as explained

previously, this implies that only the translation symmetry is broken, while the charge conjugation symmetry is unbroken in this phase. Additionally, this means that only one of the sublattices is ordered, while the other one is disordered. These patterns agree with our findings from exact diagonalization and confirm the existence of the two distinct phases.

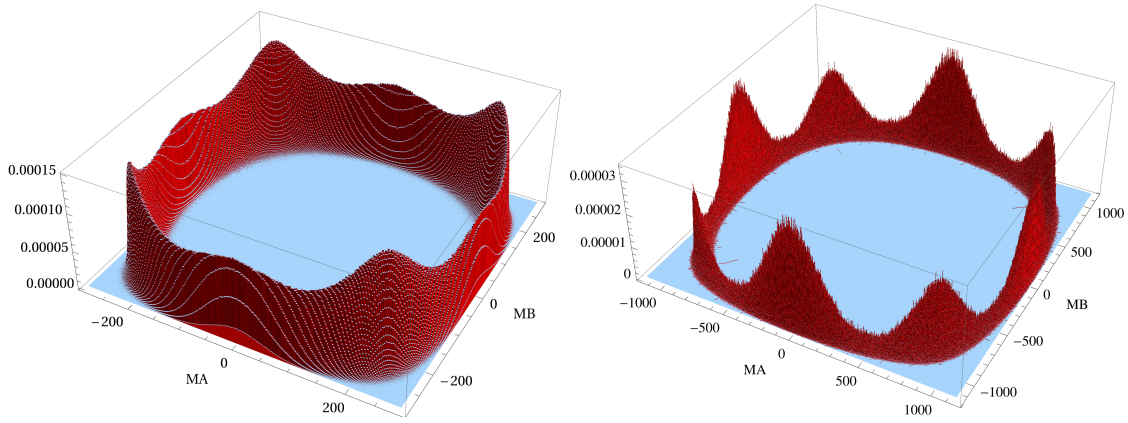

Figure 3.21: Probability distribution $p(M_A, M_B)$ at λ_c and $T \approx 0$ on a $V_s = (24a)^2$ (left) and $V_s = (48a)^2$ (right) lattice. Comparing the two plots shows that the first order nature of the transition becomes more pronounced on larger lattices.

Additionally, the cluster algorithm also allows us to investigate the phase transition itself in more detail. Figure 3.21 shows the results of simulations at λ_c. The plot on the left, on a smaller lattice, clearly shows an almost circular order parameter structure. This is evidence for an emergent approximate global $SO(2)$ symmetry, which is spontaneously broken, thus leading to an emergent pseudo-Goldstone boson. This is consistent with our findings from exact diagonalization and can be described by a low-energy effective theory we will develop in chapter 4. The plot on the right shows the behavior on larger lattices. Most evident is the more pronounced peak structure, indicating a first order nature of the transition (which is also supported by the analysis of the effective theory shown later on).

The phase diagram can also be studied as a function of temperature. Based on universality arguments, we expect that the system undergoes a Berezinski-Kosterlitz-Thouless transition into a deconfined Coulomb phase above a temperature T_c. However, translation invariance still remains broken as evidenced by the corresponding order parameter distribution shown in figure 3.22. At very high temperatures, we expect the breaking of translation invariance to disappear.

Since the quantum link model is a gauge theory in $(2+1)$-dimensions, we expect that it is linearly confining for $\lambda < 1$ and $T = 0$ [2, 3, 4]. A standard way of demonstrating this is to place a static charge-anti-charge pair at a certain distance r, and then study the static potential $V(r)$ as a function of r. A linearly increasing potential is an unambiguous

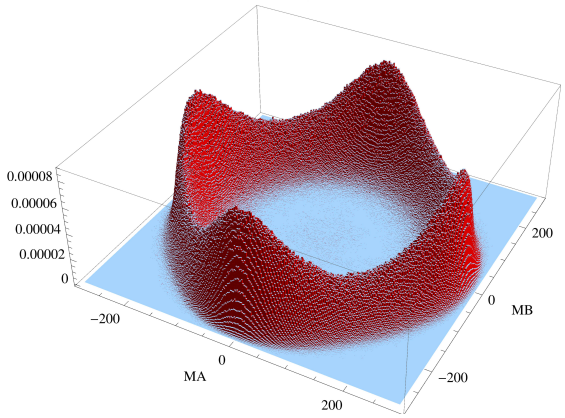

Figure 3.22: Probability distribution $p(M_A, M_B)$ at $\lambda = 0$ on a $V_s = (24a)^2$ lattice at $T > T_c$. This shows that, although the translation symmetry breaking becomes weaker, it is still present at moderate temperatures, even though we expect it to disappear completely at very high temperatures.

sign for confinement. The string tension σ is given by the slope of the static potential at large distances. We have studied this by placing static charges $Q = \pm 2$ along the lattice diagonal. Our results shown in figure 3.23 exhibit linear confinement at large distances, even at the phase transition, albeit with a small string tension $\sigma_2 = 0.156 \pm 0.014 J/a$ (compared to $\sigma_2 = 1.97 \pm 0.01 J/a$ at $\lambda = -1$. At $\lambda = 0$, we obtain $\sigma_2 = 0.46 \pm 0.01 J/a$). This non-zero string tension shows explicitly that the phase transition is not a deconfined quantum critical point. Since we insert the charges explicitly in the simulation, our results for the static potential do not suffer from an exponentially small signal-to-noise ratio at larger charge-anti-charge separations. In section 4.4.2 we will compare these values for the string tension with our results from exact diagonalization and the effective theory.

Since translation invariance by a single lattice spacing is spontaneously broken in both the phases at $\lambda < \lambda_c$ and at $\lambda > \lambda_c$, we denote the resulting confined phases as crystalline phases. The energy density $-J\langle U_\square + U_\square^\dagger \rangle$ in the presence of two charges ± 2 illustrates the nature of the bulk phases. The flux string connecting the charges, shown in figure 3.24, separates into four strands of flux $\frac{1}{2}$ that repel each other. The interior of the strands consists of the phase that is stable on the other side of the transition. Near λ_c the flux string undergoes topology change by wrapping one strand over the periodic boundary and materializing an additional strand at the edge of the system, whose interior then expands to become the new bulk phase (cf. figure 3.24 (b)).

In conclusion, we found two phases of distinct symmetry breaking patterns. One where charge conjugation and the translation symmetry are spontaneously broken ($\lambda < \lambda_c$) and one where only the translation symmetry is spontaneously broken ($\lambda > \lambda_c$). These are separated

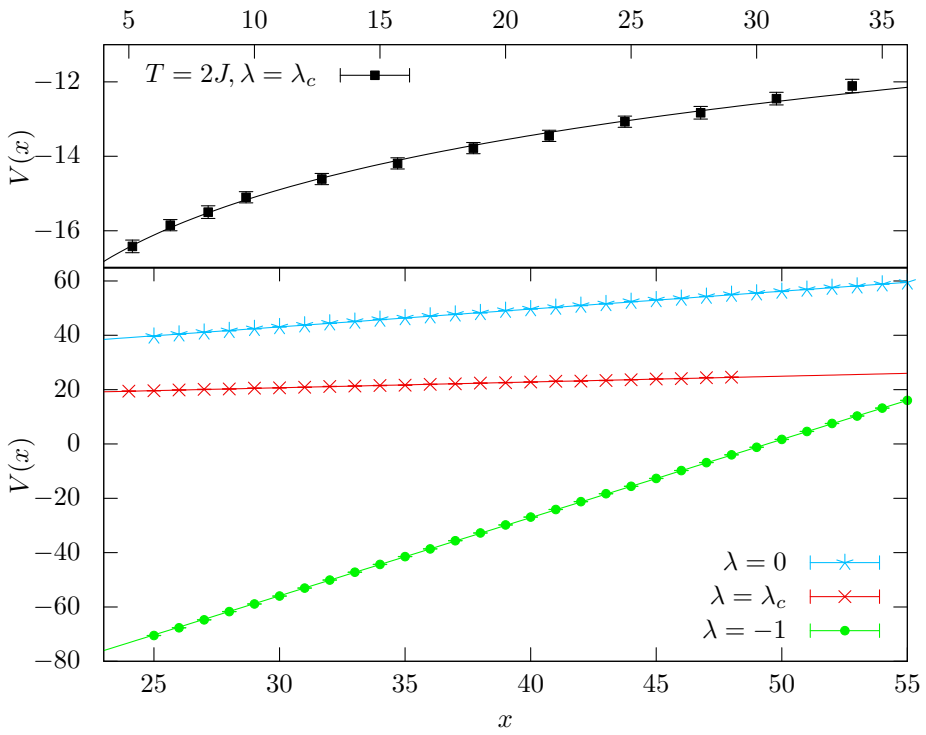

Figure 3.23: The potential between two static charges ± 2 separated by the distance (x, x) along a lattice diagonal, for $\lambda = -1, \lambda_c$, and 0, at $T \approx 0$, and at $\lambda = \lambda_c$ for $T = 2J$.

by a (weak) first order phase transition at λ_c where an emergent approximate $SO(2)$ symmetry appears. At low temperatures these phases are confined up to a deconfinement transition at a temperature T_c. The situation is sketched in figure 3.25. In the next chapter, we will formulate an effective theory that is valid near the phase transition and allows us to calculate additional properties of the transition and its surrounding.

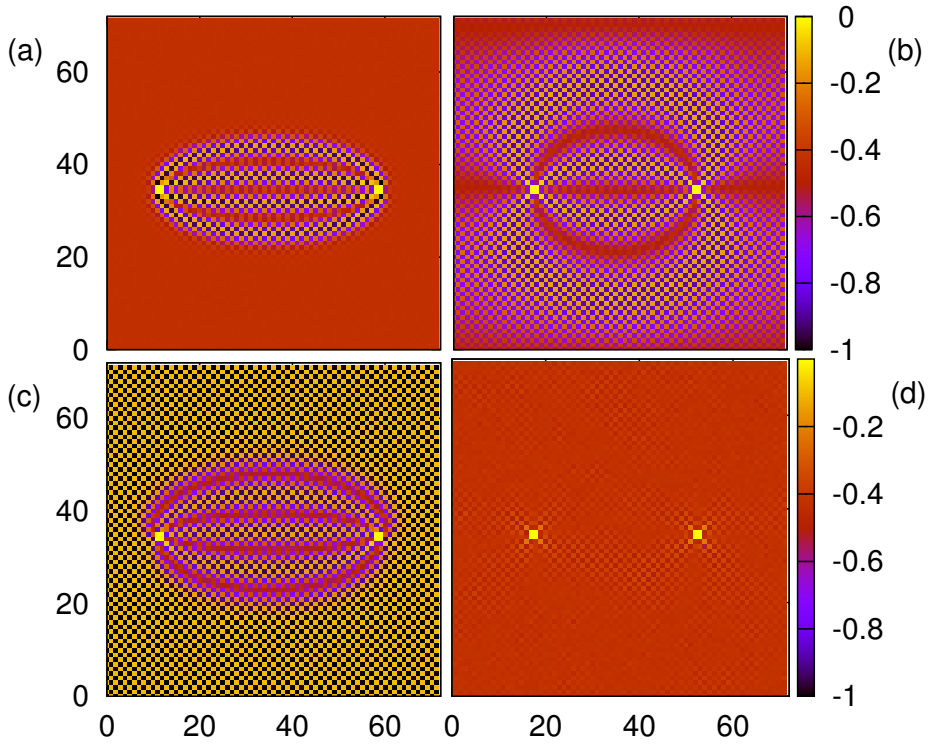

Figure 3.24: Energy density $-J\langle U_\square + U_\square^\dagger\rangle$ in the presence of two charges ± 2 for $\lambda = -1$ (a), $\lambda = \lambda_c$ (b), and $\lambda = 0$ (c) at $T \approx 0$, as well as for $\lambda = 0$ at $T > T_c$ (d).

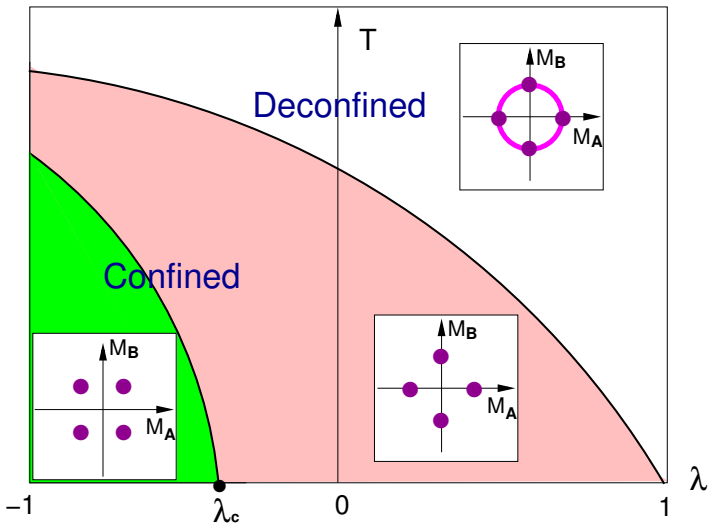

Figure 3.25: Schematic sketch of the $\lambda - T$ phase diagram with insets indicating the location of the peaks in the probability distribution of the order parameters $p(M_A, M_B)$.

4 Low-Energy Effective Theory

As described in the previous chapter, the (2+1)-d quantum link model has a quantum phase transition at $\lambda_c \approx -0.36$ at which a spontaneously broken approximate global $SO(2)$ symmetry emerges dynamically (reduced to $\mathbb{R}P(1)$ for symmetry reasons). The corresponding pseudo-Goldstone boson can be described by the effective action

$$S[\varphi] = \int d^3x \left[\frac{\rho}{2}\partial_i\varphi\partial_i\varphi + \frac{\rho}{2c^2}\partial_t\varphi\partial_t\varphi + \delta\cos^2(2\varphi) + \epsilon\cos^4(2\varphi)\right]. \tag{4.1}$$

The cos-terms break the symmetry down to $\mathbb{Z}(4)$ away from the phase transition ($\delta + \epsilon$ measures the deviation from the phase transition). The exact effects and reasoning for the different terms will become clear with the detailed explanations below.

4.1 Hamiltonian formulation and rotor spectrum

We are mostly interested in the vacuum effects of the theory. Starting with a periodic volume $L_1 \times L_2$, we can assume (to lowest order), that φ is constant in space, i.e. $\varphi(x,t) = \varphi(t)$, which implies

$$S[\varphi] = \int dt \left[\frac{\rho L1 L_2}{2c^2}\partial_t\varphi\partial_t\varphi + \delta L_1 L_2\cos^2(2\varphi) + \epsilon L_1 L_2\cos^4(2\varphi)\right]. \tag{4.2}$$

In order to calculate the spectrum of the theory, it is advisable to go to the Hamiltonian formulation of the theory. Performing the necessary transformations (while keeping in mind that the above action is written in Euclidean time) leads to the Hamiltonian

$$H = -\frac{c^2}{2\rho L_1 L_2}\partial_\varphi^2 + \delta L_1 L_2\cos^2(2\varphi) + \epsilon L_1 L_2\cos^4(2\varphi). \tag{4.3}$$

Ignoring the small perturbations, i.e. setting $\delta = \epsilon = 0$, this describes a free particle on a circle whose eigenfunctions and energy eigenvalues are given by

$$\psi_m(\varphi) = \frac{1}{\sqrt{2\pi}}\exp(im\varphi), \qquad E_m = \frac{m^2c^2}{2\rho L_1 L_2}, \quad m \in \mathbb{Z}. \tag{4.4}$$

Here, φ and $\varphi + \pi$ are physically equivalent, which implies that we should have

$$[m\varphi - m(\varphi + \pi)] = m\pi = 0 \mod 2\pi. \tag{4.5}$$

Therefore, m is restricted to even integers.

4.2 Perturbative corrections to the energy spectrum

In order to incorporate the effects of the additional terms on the spectrum, we employ perturbation theory in $\delta L_1 L_2$ and $\epsilon L_1 L_2$. Even though one might argue that they are not of the same order in the effective theory, we treat them as such here because the error contributed by this is small enough to be of no relevance for us.

4.2.1 First order perturbation theory

Using the eigenfunctions from equation (4.4), the corrections to the (non-degenerate) ground-state in first order perturbation theory are given by

$$\begin{aligned} E_0^{(1)} &= \langle 0 \left| \delta L_1 L_2 \cos^2(2\varphi) \right| 0 \rangle + \langle 0 \left| \epsilon L_1 L_2 \cos^4(2\varphi) \right| 0 \rangle \\ &= \frac{\delta L_1 L_2}{2\pi} \int_0^{2\pi} d\varphi \cos^2(2\varphi) + \frac{\epsilon L_1 L_2}{2\pi} \int_0^{2\pi} d\varphi \cos^4(2\varphi) \\ &= \frac{\delta L_1 L_2}{2} + \frac{3\epsilon L_1 L_2}{8}. \end{aligned} \tag{4.6}$$

For non-zero values of m, the states are degenerate. In order to lift this degeneracy, we will switch to using even and odd eigenfunctions, i.e. we split ψ_m into the two functions

$$\psi_m^e = \frac{1}{\sqrt{\pi}} \cos(m\varphi), \qquad \psi_m^o = \frac{1}{\sqrt{\pi}} \sin(m\varphi). \tag{4.7}$$

As we will see, in this basis the two energy eigenvalues are non-degenerate when adding the effects of the perturbations. With this we can now calculate the corrections

$$\begin{aligned} E_m^{e,(1)} &= {}_e\langle m \left| \delta L_1 L_2 \cos^2(2\varphi) \right| m \rangle_e + {}_e\langle m \left| \epsilon L_1 L_2 \cos^4(2\varphi) \right| m \rangle_e \\ &= \frac{\delta L_1 L_2}{2\pi} \int_0^{2\pi} d\varphi \cos^2(2\varphi) \cos^2(m\varphi) + \frac{\epsilon L_1 L_2}{2\pi} \int_0^{2\pi} d\varphi \cos^4(2\varphi) \cos^2(m\varphi) \end{aligned} \tag{4.8}$$

and

$$\begin{aligned} E_m^{o,(1)} &= {}_o\langle m \left| \delta L_1 L_2 \cos^2(2\varphi) \right| m \rangle_o + {}_o\langle m \left| \epsilon L_1 L_2 \cos^4(2\varphi) \right| m \rangle_o \\ &= \frac{\delta L_1 L_2}{2\pi} \int_0^{2\pi} d\varphi \cos^2(2\varphi) \sin^2(m\varphi) + \frac{\epsilon L_1 L_2}{2\pi} \int_0^{2\pi} d\varphi \cos^4(2\varphi) \sin^2(m\varphi). \end{aligned} \tag{4.9}$$

When evaluating the integrals, one finds a dependence on m of the results, which leads to corrections to the energy eigenvalues of

$$E_2^{e,(1)} = \frac{3\delta L_1 L_2}{4} + \frac{5\epsilon L_1 L_2}{8}, \tag{4.10}$$

$$E_2^{o,(1)} = \frac{\delta L_1 L_2}{4} + \frac{1\epsilon L_1 L_2}{8}, \tag{4.11}$$

$$E_4^{e,(1)} = \frac{\delta L_1 L_2}{2} + \frac{7\epsilon L_1 L_2}{16}, \tag{4.12}$$

$$E_4^{o,(1)} = \frac{\delta L_1 L_2}{2} + \frac{5\epsilon L_1 L_2}{16}, \tag{4.13}$$

$$E_m^{e/o,(1)} = \frac{\delta L_1 L_2}{2} + \frac{3\epsilon L_1 L_2}{8} \tag{4.14}$$

where the last line is valid for all $|m| > 4$. Remarkably, this tells us that the degeneracy of the energy levels is not lifted for values of m larger than 4 in first order perturbation theory.

4.2.2 Second order perturbation theory

The second order corrections to the energy eigenvalues are given by

$$E_m^{e/o,(2)} = -\sum_{n\neq 0} \frac{|{}_{e,o}\langle m\,|V|\,n\rangle_{e,o}|^2}{E_n - E_m}, \tag{4.15}$$

$$V = \delta L_1 L_2 \cos^2(2\varphi) + \epsilon L_1 L_2 \cos^4(2\varphi). \tag{4.16}$$

Using the relations

$$\cos^4(2\varphi) = \left[\frac{1+\cos(4\varphi)}{2}\right]^2 = \frac{1}{4}\left(1 + 2\cos(4\varphi) + \cos^2(4\varphi)\right), \tag{4.17}$$

$$\cos(m\varphi)\cos(n\varphi) = \frac{1}{2}\left[\cos((m-n)\varphi) + \cos((m+n)\varphi)\right], \tag{4.18}$$

$$\sin(m\varphi)\sin(n\varphi) = \frac{1}{2}\left[\cos((m-n)\varphi) - \cos((m+n)\varphi)\right], \tag{4.19}$$

the relevant matrix elements can be easily (but tediously) calculated. The matrix elements of the even functions for $m, n > 0$ yield

$${}_e\langle m\left|\delta L_1 L_2 \cos^2(2\varphi)\right| n\rangle_e = \frac{\delta L_1 L_2}{8}[2\delta_{m,n+4} + 4\delta_{m,n} + 2\delta_{m,n-4} + 2\delta_{m,-n+4}], \tag{4.20}$$

$$\begin{aligned}{}_e\langle m\left|\epsilon L_1 L_2 \cos^4(2\varphi)\right| n\rangle_e = \frac{\epsilon L_1 L_2}{8}[&3\delta_{m,n} + 2\delta_{4,m-n} + 2\delta_{4,m+n} + 2\delta_{4,n-m} \\ &+ \frac{1}{2}\delta_{8,m-n} + \frac{1}{2}\delta_{8,m+n} + \frac{1}{2}\delta_{8,n-m}],\end{aligned} \tag{4.21}$$

while for $m = 0$ and $n \neq 0$, we get

$${}_e\langle m\left|\delta L_1 L_2 \cos^2(2\varphi)\right| n\rangle_e = \frac{\delta L_1 L_2}{4}\left[\delta_{n,0} + \sqrt{2}\delta_{n,4}\right], \tag{4.22}$$

$${}_e\langle m\left|\epsilon L_1 L_2 \cos^4(2\varphi)\right| n\rangle_e = \frac{\epsilon L_1 L_2}{\sqrt{2}4}\left[\frac{3}{\sqrt{2}}\delta_{n,0} + 2\delta_{n,4} + \frac{1}{2}\delta_{n,8}\right]. \tag{4.23}$$

For the odd eigenfunctions, we obtain for $m, n > 0$

$$ {}_o\langle m \left| \delta L_1 L_2 \cos^2(2\varphi) \right| n \rangle_o = \frac{\delta L_1 L_2}{8} [2\delta_{m,n+4} + 4\delta_{m,n} + 2\delta_{m,n-4} - 2\delta_{m,-n+4}], \tag{4.24} $$

$$ \begin{aligned} {}_o\langle m \left| \epsilon L_1 L_2 \cos^4(2\varphi) \right| n \rangle_o = \frac{\epsilon L_1 L_2}{8} [&3\delta_{m,n} + 2\delta_{4,m-n} - 2\delta_{4,m+n} + 2\delta_{4,n-m} \\ &+ \frac{1}{2}\delta_{8,m-n} - \frac{1}{2}\delta_{8,m+n}], \end{aligned} \tag{4.25} $$

while for $m = 0$ and $n \neq 0$, we get

$$ {}_o\langle m \left| \delta L_1 L_2 \cos^2(2\varphi) \right| n \rangle_o = {}_o\langle m \left| \epsilon L_1 L_2 \cos^4(2\varphi) \right| n \rangle_o = 0. \tag{4.26} $$

Inserting these matrix elements into the sums of equation (4.16) yields the second order corrections

$$ E_0^{(2)} = -\frac{\rho L_1^3 L_2^3}{4096 c^2} \left[64\delta^2 + 128\delta\epsilon + 65\epsilon^2 \right], \tag{4.27} $$

$$ E_2^{e,(2)} = -\frac{\rho L_1^3 L_2^3}{1024 c^2} \left[4\delta^2 + 10\delta\epsilon + \frac{19}{3}\epsilon^2 \right], \tag{4.28} $$

$$ E_2^{o,(2)} = -\frac{\rho L_1^3 L_2^3}{1024 c^2} \left[4\delta^2 + 6\delta\epsilon + \frac{7}{3}\epsilon^2 \right], \tag{4.29} $$

$$ E_4^{e,(2)} = -\frac{\rho L_1^3 L_2^3}{128 c^2} \left[\frac{5}{3}(\delta + \epsilon)^2 - \frac{1}{128}\epsilon^2 \right], \tag{4.30} $$

$$ E_4^{o,(2)} = -\frac{\rho L_1^3 L_2^3}{1024 c^2} \left[\frac{1}{3}(\delta + \epsilon)^2 + \frac{1}{128}\epsilon^2 \right], \tag{4.31} $$

$$ E_6^{e,(2)} = -\frac{\rho L_1^3 L_2^3}{1024 c^2} \left[\delta^2 + 3\delta\epsilon + \frac{21}{10}\epsilon^2 \right], \tag{4.32} $$

$$ E_6^{o,(2)} = -\frac{\rho L_1^3 L_2^3}{1024 c^2} \left[\delta^2 + \delta\epsilon + \frac{}{10}\epsilon^2 \right], \tag{4.33} $$

for the lowest few values of m.

4.2.3 Results

As the goal of these calculations is the comparison with the exact diagonalization results, we return now to the notation of section 3.2. The relevant energy differences are

$$ E_+ = E_2^{(0)} + E_2^{e,(1)} + E_2^{e,(2)} - E_0^{(0)} - E_0^{(1)} - E_0^{(2)}, \tag{4.34} $$

$$ E_- = E_2^{(0)} + E_2^{o,(1)} + E_2^{o,(2)} - E_0^{(0)} - E_0^{(1)} - E_0^{(2)}, \tag{4.35} $$

$$ E'_+ = E_4^{(0)} + E_4^{e,(1)} + E_4^{e,(2)} - E_0^{(0)} - E_0^{(1)} - E_0^{(2)}, \tag{4.36} $$

$$ E'_- = E_4^{(0)} + E_4^{o,(1)} + E_4^{o,(2)} - E_0^{(0)} - E_0^{(1)} - E_0^{(2)}, \tag{4.37} $$

$$ E''_+ = E_6^{(0)} + E_6^{e,(1)} + E_6^{e,(2)} - E_0^{(0)} - E_0^{(1)} - E_0^{(2)}, \tag{4.38} $$

$$ E''_- = E_6^{(0)} + E_6^{o,(1)} + E_6^{o,(2)} - E_0^{(0)} - E_0^{(1)} - E_0^{(2)}. \tag{4.39} $$

Inserting the results from the previous sections into these equations yields

$$E_+ = \frac{2c^2}{\rho L_1 L_2} + \frac{L_1 L_2}{4}(\delta+\epsilon) + \frac{\rho L_1^3 L_2^3}{256c^2}\left(3\delta^2 + \frac{11}{2}\delta\epsilon + \frac{119}{48}\epsilon^2\right) + O(\epsilon^3,\, \delta^3), \tag{4.40}$$

$$E_- = \frac{2c^2}{\rho L_1 L_2} - \frac{L_1 L_2}{4}(\delta+\epsilon) + \frac{\rho L_1^3 L_2^3}{256c^2}\left(3\delta^2 + \frac{13}{2}\delta\epsilon + \frac{167}{48}\epsilon^2\right) + O(\epsilon^3,\, \delta^3), \tag{4.41}$$

$$E'_+ = \frac{8c^2}{\rho L_1 L_2} + \frac{L_1 L_2}{16}\epsilon + \frac{\rho L_1^3 L_2^3}{128c^2}\left(\frac{11}{3}(\delta+\epsilon)^2 + \frac{3}{128}\epsilon^2\right) + O(\epsilon^3,\, \delta^3), \tag{4.42}$$

$$E'_- = \frac{8c^2}{\rho L_1 L_2} - \frac{L_1 L_2}{16}\epsilon + \frac{\rho L_1^3 L_2^3}{128c^2}\left(\frac{5}{3}(\delta+\epsilon)^2 + \frac{3}{128}\epsilon^2\right) + O(\epsilon^3,\, \delta^3), \tag{4.43}$$

$$E''_+ = \frac{18c^2}{\rho L_1 L_2} + \frac{\rho L_1^3 L_2^3}{512c^2}\left(9\delta^2 + 19\delta\epsilon + \frac{409}{40}\epsilon^2\right) + O(\epsilon^3,\, \delta^3), \tag{4.44}$$

$$E''_- = \frac{18c^2}{\rho L_1 L_2} + \frac{\rho L_1^3 L_2^3}{512c^2}\left(9\delta^2 + 17\delta\epsilon + \frac{329}{40}\epsilon^2\right) + O(\epsilon^3,\, \delta^3). \tag{4.45}$$

As we have seen in section 3.2, the location and number of the crossing points between the different + and − states depends on m. Let us therefore check what the effective theory predicts for those. The condition for the intersection of the lowest two energy levels is

$$\begin{aligned} E_+ = E_- \quad &\Rightarrow \quad \frac{L_1 L_2}{2}(\delta+\epsilon) = \frac{\rho L_1^3 L_2^3}{256c^2}\epsilon\,[\delta+\epsilon] \\ &\Rightarrow \quad \delta+\epsilon = 0 \quad \text{or} \quad \epsilon = \frac{128c^2}{\rho L_1^2 L_2^2}. \end{aligned} \tag{4.46}$$

For $\epsilon < 0$, the crossing therefore happens at $\delta = -\epsilon$. For the next two energy levels, the crossing condition becomes

$$\begin{aligned} E'_+ = E'_- \quad &\Rightarrow \quad \frac{L_1 L_2}{8}\epsilon = -\frac{2\rho L_1^3 L_2^3}{128c^2}(\delta+\epsilon)^2 \\ &\Rightarrow \quad \epsilon = -\frac{\rho L_1^2 L_2^2}{8c^2}(\delta+\epsilon)^2. \end{aligned} \tag{4.47}$$

As expected, this yields two solutions. Finally, the crossing of the two third excited states occurs for

$$\begin{aligned} E''_+ = E''_- \quad &\Rightarrow \quad \frac{2L_1^3 L_2^3}{512c^2}\epsilon(\delta+\epsilon) = 0 \\ &\Rightarrow \quad \delta = -\epsilon. \end{aligned} \tag{4.48}$$

This crossing again occurs at the transition point. For completeness, the energies at the crossing points are given by

$$E_+ = E_- = \frac{2c^2}{\rho L_1 L_2} - \frac{\rho L_1^3 L_2^3}{256c^2}\epsilon^2, \tag{4.49}$$

$$E'_+ = E'_- = \frac{8c^2}{\rho L_1 L_2} - \frac{L_1 L_2}{6}\epsilon + \frac{\rho L_1^3 L_2^3}{128c^2}\frac{3\epsilon^2}{128}, \tag{4.50}$$

$$E''_+ = E''_- = \frac{18c^2}{\rho L_1 L_2} + \frac{\rho L_1^3 L_2^3}{512c^2}\frac{9\epsilon^2}{40}. \tag{4.51}$$

4.3 Mean-field analysis and interface tension

4.3.1 Minima of the potential

We can analyze the different phases of the theory by applying the Ginsburg-Landau-Wilson paradigm to the δ and ϵ terms in mean field theory. To this end, we consider only the potential of the effective theory, which is given by

$$V(\varphi) = \delta \cos^2(2\varphi) + \epsilon \cos^4(2\varphi). \tag{4.52}$$

From this, we can calculate the extrema of the potential by using

$$\begin{aligned} \frac{\partial V(\varphi)}{\partial \varphi} &= -4\delta \cos(2\varphi)\sin(2\varphi) - 8\epsilon \cos^3(2\varphi)\sin(2\varphi) \\ &= -4\sin(2\varphi)\cos(2\varphi)\left(\delta + 2\epsilon\cos^2(2\varphi)\right). \end{aligned} \tag{4.53}$$

This is zero when we have either

$$\cos(2\varphi) = 0, \qquad \sin(2\varphi) = 0 \qquad \text{or} \qquad \cos^2(2\varphi) = -\frac{\delta}{2\epsilon}. \tag{4.54}$$

At these points, the potential takes the values

- $\cos(2\varphi) = 0$: $V(\varphi) = 0$,
- $\sin(2\varphi) = 0$: $V(\varphi) = \delta + \epsilon$,
- $\cos^2(2\varphi) = -\frac{\delta}{2\epsilon}$: $V(\varphi) = -\frac{\delta^2}{4\epsilon}$.

Additionally, we can read off the masses of the (pseudo-)Goldstone boson in these regions from

$$\begin{aligned} \frac{\partial^2 V(\varphi)}{\partial \varphi^2} &= \frac{\partial}{\partial \varphi}\left(-4\sin(2\varphi)\cos(2\varphi)\left(\delta + 2\epsilon\cos^2(2\varphi)\right)\right) \\ &= 8\delta\sin^2(2\varphi) - 8\delta\cos^2(2\varphi) - 16\epsilon\cos^4(2\varphi) + 16\epsilon\cos^2(2\varphi)\sin^2(2\varphi). \end{aligned} \tag{4.55}$$

At the three extrema, these take the values

- $\cos(2\varphi) = 0$: $m^2c^2 = 8\frac{\delta}{\rho}$,
- $\sin(2\varphi) = 0$: $m^2c^2 = \frac{1}{\rho}(-8\delta - 16\epsilon)$,
- $\cos^2(2\varphi) = -\frac{\delta}{2\epsilon}$: $m^2c^2 = -\frac{8\delta}{\epsilon\rho}(\delta + 2\epsilon)$.

Note the additional factor of ρ due to the (unusual) normalization of the kinetic term in equation (4.1).

Let us now analyze in which parts of the δ-ϵ-plane each of these extrema actually is the global minimum of the potential.

Absolute minimum when $\cos(2\varphi) = 0$

For this to be the absolute minimum, the potential here has to be smaller than the values from the other two extrema. To this end, we first observe that the extrema at $\cos^2(2\varphi) = -\frac{\delta}{2\epsilon}$ only exist when δ and ϵ are of opposite sign. If this is the case, then we need to have

$$\begin{aligned} & 0 < \delta + \epsilon \quad \text{and} \quad 0 < -\frac{\delta^2}{4\epsilon} \\ \Rightarrow \quad & \epsilon < 0, \quad \text{and} \quad \delta > -\epsilon. \end{aligned} \tag{4.56}$$

Otherwise, if δ and ϵ have the same sign, there are only two extrema and the only remaining condition is

$$0 < \delta + \epsilon \qquad \Rightarrow \qquad \delta, \epsilon > 0. \tag{4.57}$$

Absolute minimum when $\sin(2\varphi) = 0$

Again, the third extremum does not exist if δ and ϵ have the same sign. In this case we have the sole condition

$$\delta + \epsilon < 0 \qquad \Rightarrow \qquad \delta, \epsilon < 0. \tag{4.58}$$

Otherwise, if δ and ϵ have different signs, there are two cases. If $\epsilon < 0$, then we get the condition

$$\delta + \epsilon < 0 \qquad \Rightarrow \qquad \delta < -\epsilon. \tag{4.59}$$

For $\epsilon > 0$, we calculate

$$\begin{aligned} & \delta + \epsilon < -\frac{\delta^2}{4\epsilon} \\ \Rightarrow \quad & \delta^2 + 4\epsilon\delta + 4\epsilon^2 < 0. \end{aligned} \tag{4.60}$$

This inequality is satisfied as an equality if

$$\delta = \frac{-4\epsilon \pm \sqrt{16\epsilon^2 - 4 \cdot 4\epsilon^2}}{2} = -2\epsilon. \tag{4.61}$$

Therefore, in this case we obtain the condition

$$\delta < -2\epsilon. \tag{4.62}$$

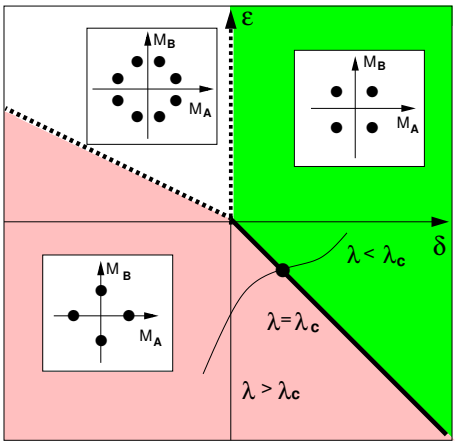

Figure 4.1: Phase diagram as a function of δ and ϵ. The insets indicate the location of the peaks in the distribution $p(M_A, M_B)$. The fat and dashed lines are first and second order phase transitions, respectively. The curved line indicates a possible path taken in the quantum link model when varying λ.

4.3.2 Phase diagram of the effective theory in the δ-ϵ-plane

Figure 4.1 shows the result of putting all the above calculations together. We obtain the two phases that we have already observed with the cluster algorithm as well as an additional mixed phase. As can be easily verified, on the lines connecting the mixed and either of the other two phases, the Goldstone boson mass vanishes, while the one separating the two phases with four peaks is always equal to $m = 8\delta$ and therefore non-zero. The first two lines (the dashed ones in the plot) represent phase transitions of second order, while the last solid one is of first order.

4.3.3 String and interface tension

If we construct a flux configuration where one part is occupied by one of the two phases present in the groundstate, while the other part has the alternative order, then, necessarily, there will be an interface between them. An example for very large, negative values of λ is shown in figure 4.2. The left part consists of one of the two reference configurations, while the right part is in the other reference configuration. From top to bottom there are ordinary periodic boundary conditions, while from left to right we have C-periodic boundary conditions [75, 76]. These are defined by replacing the link variables with their charge conjugates when they are shifted over the boundary (i.e. by flipping the flux arrows). In this special case, the interface becomes a flux $\frac{1}{2}$ string, depicted by the fat line in the middle. Note, however, that this simple situation only occurs for very large negative values of λ, while for smaller values

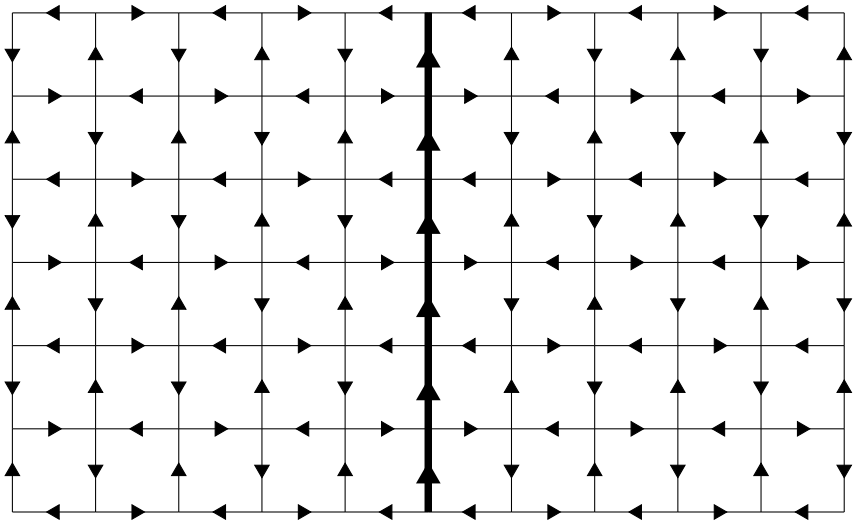

Figure 4.2: Interface at $\lambda \to -\infty$. The fat line is a flux $\frac{1}{2}$ string.

(e.g. where the effective theory is applicable) the interface does not consist of exactly such a state but of a superposition of several configurations. In order to calculate the interface tension, we will now calculate the energy (relative to the groundstate) of a configuration which is defined only by having one kind of order at large negative values of x and the alternative order at large positive values of x in each of the two phases of interest, i.e. in the $\cos(2\varphi) = 0$ and in the $\sin(2\varphi) = 0$ phase. We will do this without specifying exactly how the interface in-between is realized.

In order to calculate the tension, we will add up the energy contribution along the flux string minus the energy of the vacuum V_0, i.e.

$$\alpha = \int_{-\infty}^{\infty} dx \, (E_{kin} + V(\varphi) - V_0) \tag{4.63}$$

The kinetic energy is as usual given by $E_{kin} = \frac{\rho}{2}\partial_x\varphi\partial_x\varphi$. To lowest order, it suffices to calculate the classical solution with minimal energy by inserting the Lagrangian density into the Euler-Lagrange equation

$$-\frac{\partial \, (E_{kin} + V(\varphi) - V_0)}{\partial\varphi} + \frac{d}{dx}\left(\frac{\partial \, (E_{kin} + V(\varphi) - V_0)}{\partial(\partial_x\varphi)}\right) = 0. \tag{4.64}$$

Doing this yields the equation

$$\rho\partial_x^2\varphi - \frac{\partial(V(\varphi) - V_0)}{\partial\varphi} = 0, \tag{4.65}$$

which, up to an overall factor of $\partial_x\varphi$, is the same as

$$\partial_x\left[\frac{\rho}{2}\partial_x\varphi\partial_x\varphi - (V(\varphi) - V_0)\right] = 0. \tag{4.66}$$

In our setup, the two phases at $x \to \pm\infty$ are minima of the potential distinguished by different values of φ which implies that $\partial_x\varphi$ is non-zero and the two equations are therefore equivalent. Equation (4.66) implies that the combination of terms in brackets is constant. In order to evaluate this constant, we consider its value far away from the flux string, e.g. for very large x. There, we have a phase given by a minimum of the potential, and therefore

$$(V(\varphi) - V_0) = 0. \tag{4.67}$$

Additionally, the value of φ in this region is fixed and we therefore get $\partial_x\varphi = 0$. Inserting these values into the constant expression shows that the constant actually vanishes. This yields the equation

$$\frac{\rho}{2}(\partial_x\varphi)^2 = V(\varphi) - V_0. \tag{4.68}$$

Solving this equation for $\partial_x\varphi$ yields

$$\partial_x\varphi = \sqrt{\frac{2}{\rho}(V(\varphi) - V_0)}. \tag{4.69}$$

Interface tension in the $\cos(2\varphi) = 0$ phase

After these preparations, we can now insert the actual values. In the $\cos(2\varphi) = 0$ region, we have a vanishing minimal potential, i.e. $V_0 = 0$. The potential itself is given by

$$V(\varphi) = \delta\cos^2(2\varphi) + \epsilon\cos^4(2\varphi). \tag{4.70}$$

Turning to the calculation of α itself, we can now write

$$\begin{aligned}\alpha &= \int_{-\infty}^{\infty} dx \left[\frac{\rho}{2}\partial_x\varphi\partial_x\varphi + (V(\varphi) - V_0)\right] = \int_{-\infty}^{\infty} dx\rho\partial_x\varphi\partial_x\varphi \\ &= \int_{-\frac{\pi}{4}}^{\frac{\pi}{4}} d\varphi\frac{1}{\partial_x\varphi}\rho\partial_x\varphi\partial_x\varphi = \int_{-\frac{\pi}{4}}^{\frac{\pi}{4}} d\varphi\rho\partial_x\varphi,\end{aligned} \tag{4.71}$$

where we first used equation (4.68) to get rid of the potential terms. In the next equation we performed a substitution in order to be able to actually calculate the integral. With our potential, equation (4.69) now becomes

$$\partial_x\varphi = \sqrt{\frac{2}{\rho}(V(\varphi) - V_0)} = \cos(2\varphi)\sqrt{\frac{2\delta}{\rho} + \frac{2\epsilon}{\rho}\cos^2(2\varphi)}. \tag{4.72}$$

Using this, we write

$$\begin{aligned}
\alpha &= \int_{-\frac{\pi}{4}}^{\frac{\pi}{4}} d\varphi \rho \partial_x \varphi \\
&= \int_{-\frac{\pi}{4}}^{\frac{\pi}{4}} d\varphi \rho \cos(2\varphi) \sqrt{\frac{2\delta}{\rho} + \frac{2\epsilon}{\rho}\cos^2(2\varphi)} \\
&= \rho \left[\frac{1}{4}\sin(2\varphi)\sqrt{\frac{2\delta}{\rho} + \frac{2\epsilon}{\rho}\cos^2(2\varphi)} + \frac{\delta+\epsilon}{2\sqrt{2\rho\epsilon}} \operatorname{atan}\left(\frac{\sqrt{2\epsilon}\sin(2\varphi)}{\sqrt{2\delta + \epsilon\cos(4\varphi) + \epsilon}} \right) \right]_{-\frac{\pi}{4}}^{\frac{\pi}{4}} \\
&= \sqrt{\frac{\rho\delta}{2}} + (\delta+\epsilon)\sqrt{\frac{\rho}{2\epsilon}} \operatorname{atan}\left(\sqrt{\frac{\epsilon}{\rho}} \right). \qquad (4.73)
\end{aligned}$$

As a special case, we can see what happens for $\epsilon \to 0$. There, we obtain

$$\begin{aligned}
\alpha &= \int_{-\frac{\pi}{4}}^{\frac{\pi}{4}} d\varphi \rho \cos(2\varphi) \sqrt{\frac{2\delta}{\rho} + \frac{2\epsilon}{\rho}\cos^2(2\varphi)} \\
&= \sqrt{2\rho\delta} \int_{-\frac{\pi}{4}}^{\frac{\pi}{4}} d\varphi \cos(2\varphi) \\
&= \sqrt{2\rho\delta}. \qquad (4.74)
\end{aligned}$$

Note that this vanishes only for $\delta = 0$ (which would be the transition point without the ϵ-term).

In our simulations, we have seen that a flux string splits into several strands of flux $\frac{1}{2}$ separating different realizations of the bulk phase. These strands therefore manifest themselves as interfaces between these realizations and their string tension is comparable to the interface tension calculated here. For $\lambda < 1$, we never obtain a vanishing string tension in our simulations, even at the phase transition itself. This is consistent with the above result if the ϵ-term is included in the effective theory (and therefore explains the reason for adding it).

In evaluating the integral above, we have implicitly assumed $\epsilon > 0$. However, from our previous calculation, we know that this phase also extends to negative ϵ, provided that we keep $\epsilon > -\delta$. In this regime, we can write

$$\begin{aligned}
\alpha &= \int_{-\frac{\pi}{4}}^{\frac{\pi}{4}} d\varphi \rho \cos(2\varphi) \sqrt{\frac{2\delta}{\rho} + \frac{2\epsilon}{\rho}\cos^2(2\varphi)} \\
&= \int_{-\frac{\pi}{4}}^{\frac{\pi}{4}} d\varphi \rho \cos(2\varphi) \sqrt{\frac{2\delta}{\rho} + \frac{2\epsilon}{\rho}(1 - \sin^2(2\varphi))} \\
&= \int_{-\frac{\pi}{4}}^{\frac{\pi}{4}} d\varphi \rho \cos(2\varphi) \sqrt{\frac{2(\delta+\epsilon)}{\rho} - \frac{2\epsilon}{\rho}\sin^2(2\varphi)} \\
&= \sqrt{\frac{\rho\delta}{2}} + (\delta+\epsilon)\sqrt{-\frac{\rho}{2\epsilon}} \operatorname{atanh}\left(\sqrt{-\frac{\epsilon}{\rho}} \right), \qquad (4.75)
\end{aligned}$$

which is identical to the previous expression up to a replacement of ϵ by $-\epsilon$ and atan by atanh. With this we now calculate the string tension at the phase transition, i.e. at $\delta_c + \epsilon_c = 0$. This trivially yields

$$\alpha = \sqrt{\frac{\rho\delta_c}{2}}, \tag{4.76}$$

which shows that the string tension indeed does not vanish at the phase transition even though it may become rather small.

Interface tension in the $\sin(2\varphi) = 0$ phase

In the second region, where $\sin(2\varphi) = 0$, the minima of the potential are at $\varphi_1 = 0$ and $\varphi_2 = \frac{\pi}{2}$, the vacuum value is $V_0 = \delta + \epsilon$ instead of zero and we have either $\epsilon < 0$, $\delta > -\epsilon$ or $\epsilon > 0$, $\delta < -2\epsilon$. The value of the potential relative to the vacuum can be written as

$$\begin{aligned} V(\varphi) - V_0 &= \delta\cos^2(2\varphi) + \epsilon\cos^4(2\varphi) - (\delta + \epsilon) \\ &= \delta(1 - \sin^2(2\varphi)) + \epsilon(1 - \sin(2\varphi)^2)^2 - \delta - \epsilon \\ &= \sin^2(2\varphi)\left[-(\delta + \epsilon) - \epsilon\cos^2(2\varphi)\right]. \end{aligned} \tag{4.77}$$

Inserting this potential into equation (4.69), we obtain

$$\partial_x\varphi = \sin(2\varphi)\sqrt{-\frac{2}{\rho}(\delta + \epsilon) - \frac{2\epsilon}{\rho}\cos^2(2\varphi)}. \tag{4.78}$$

With this and for negative values of ϵ, α becomes

$$\begin{aligned} \alpha &= \int_0^{\frac{\pi}{2}} d\varphi\rho\partial_x\varphi \\ &= \int_0^{\frac{\pi}{2}} d\varphi\rho\sin(2\varphi)\sqrt{-\frac{2}{\rho}(\delta + \epsilon) - \frac{2\epsilon}{\rho}\cos^2(2\varphi)} \\ &= \sqrt{-\frac{\rho}{2}(\delta + 2\epsilon)} - (\delta + \epsilon)\sqrt{-\frac{\rho}{2\epsilon}}\operatorname{atanh}\left(\sqrt{\frac{\epsilon}{\delta + 2\epsilon}}\right). \end{aligned} \tag{4.79}$$

At the phase transition $\delta_c = -\epsilon_c$, we again obtain the result

$$\alpha = \sqrt{\frac{\rho\delta_c}{2}}, \tag{4.80}$$

in agreement with the previous calculation. For $\epsilon > 0$, $\delta < -2\epsilon$, we write

$$V(\varphi) - V_0 = \sin^2(2\varphi)\left[-(\delta + 2\epsilon) + \epsilon\sin^2(2\varphi)\right] \tag{4.81}$$

and α now becomes

$$\begin{aligned} \alpha &= \int_0^{\frac{\pi}{2}} d\varphi\rho\partial_x\varphi \\ &= \int_0^{\frac{\pi}{2}} d\varphi\rho\sin(2\varphi)\sqrt{-\frac{2}{\rho}(\delta + 2\epsilon) + \frac{2\epsilon}{\rho}\sin^2(2\varphi)} \\ &= \sqrt{-\frac{\rho}{2}(\delta + 2\epsilon)} - (\delta + \epsilon)\sqrt{\frac{\rho}{2\epsilon}}\operatorname{atan}\left(\sqrt{-\frac{\epsilon}{\delta + 2\epsilon}}\right). \end{aligned} \tag{4.82}$$

4.4 Global fit to exact diagonalization results

Using the perturbative results for the energy spectrum calculated previously, we can match them with the numerical results from exact diagonalization in order to obtain the values for the low-energy parameters $\frac{\rho}{c^2}$, δ, and ϵ. In terms of the parameters of the quantum link model, we represent them as

$$\frac{\rho}{c^2} = c_1, \qquad \delta + \epsilon = c_2(\lambda - \lambda_c), \qquad \epsilon = (c_3 + \lambda c_4), \tag{4.83}$$

where c_1, c_2, c_3, c_4 and λ_c are five new parameters to be extracted from the rotor spectrum. The value of λ_c can be extracted from the crossing of the energy levels E_+, E_- and E''_+, E''_-, respectively. As shown previously, they are volume-independent up to the order considered. We have taken into account higher order effects in the fits by assuming

$$\lambda_{pc}^{\pm 2} = \lambda_c + \frac{A}{V^2}, \qquad \lambda_{pc}^{\pm 6} = \lambda_c + \frac{B}{V^2}. \tag{4.84}$$

Here, A and B are additional parameters to be fitted. Moreover, the crossing of E'_+ and E'_-, i.e. $\lambda_{pc}^{\pm 4}$, can be used as well. Starting from the expression for the crossing points and inserting the representations above, we obtain

$$\begin{aligned} \epsilon &= -\frac{\rho L_1^2 L_2^2}{8c^2}(\delta + \epsilon)^2 \\ \Rightarrow c_3 + \lambda_{pc}^{\pm 4} c_4 &= -\frac{c_1 L_1^2 L_2^2}{8} c_2^2 (\lambda_{pc}^{\pm 4} - \lambda_c)^2. \end{aligned} \tag{4.85}$$

Solving this equation for $\lambda_{pc}^{\pm 4}$ yields

$$\lambda_{pc}^{\pm 4} = \lambda_c \pm \frac{1}{L_1 L_2} \sqrt{-\frac{8}{c_1 c_2^2}(c_3 + \lambda_c c_4) + \frac{16 c_4^2}{c_1^2 c_2^4 L_1^4 L_2^4}} - \frac{4 c_4}{c_1 c_2^2 L_1^2 L_2^2}. \tag{4.86}$$

Expanding this out, one can fit these crossings as

$$\lambda_{pc}^{\pm 4} = \lambda_c \pm \frac{C}{L_1 L_2} + \frac{D_\pm}{L_1^2 L_2^2}, \qquad C = \sqrt{-\frac{8\,(c_3 + \lambda_c c_4)}{c_1 c_2^2}}, \tag{4.87}$$

where $D_\pm$ are two additional fit parameters.

4.4.1 Momentum states

At the phase transition $\delta_c + \epsilon_c = 0$, we previously calculated the (pseudo-)Goldstone boson mass to be

$$mc = 2\sqrt{\frac{2\,|\delta|}{\rho}}. \tag{4.88}$$

The energy of a state with momentum $p = (\frac{2\pi n_1}{L_1}, \frac{2\pi n_2}{L_2})$ is then given by

$$E(p) = \sqrt{(pc)^2 + (mc^2)^2} = c\sqrt{p^2 + \frac{8\delta_c}{\rho}}. \tag{4.89}$$

If we have a value for $\frac{\rho}{c^2}$ from a global fit as explained above, we can then use this energy relation to calculate c itself by writing

$$c^2 = \frac{E^2 - 8\delta_c \frac{c^2}{\rho}}{p^2}. \tag{4.90}$$

4.4.2 Results

Using the representations described above, we now perform a global fit to the relevant energy eigenstates $E_\pm$, $E'_\pm$ and $E''_\pm$ as well as the crossing points λ_{pc}, λ'_{pc} and λ''_{pc} on the 4×4, 4×6, 6×6, and 6×8 lattices. This yields

$$\begin{aligned}
\lambda_c &= -0.3628 \pm 0.0009, & D_+ &= 24.5 \pm 5.6,\\
c_1 &= 0.2049 \pm 0.0001, & D_- &= -36.1 \pm 30.7,\\
c_2 &= -0.1647 \pm 0.0044, & A &= 4.4 \pm 3.8,\\
c_3 &= 0.0193 \pm 0.0070, & B &= 126.5 \pm 18.7,\\
c_4 &= 0.0723 \pm 0.0201.
\end{aligned} \tag{4.91}$$

With these results and the representations from equation (4.83), we can then calculate the parameters from the effective theory, which results in

$$\frac{\rho}{c^2} = c_1 = 0.2049 \pm 0.0001 \frac{1}{Ja^2}, \tag{4.92}$$

$$\delta_c = -\epsilon_c = -c_3 - \lambda_c c_4 = 0.0069 \pm 0.0101 \frac{J}{a^2}. \tag{4.93}$$

Using these and the energies of the states with a small momentum relative to the groundstate from exact diagonalization, we calculate c (and therefore ρ as well) using equation (4.90). This yields

$$c = 1.48 \pm 0.09\, Ja, \tag{4.94}$$

$$\rho = 0.449 \pm 0.05\, J. \tag{4.95}$$

At the phase transition, we use these values to calculate the pseudo-Goldstone boson mass

$$mc = 2\sqrt{\frac{2\,|\delta_c|}{\rho}} = 0.35 \pm 0.26\,\frac{1}{a} \tag{4.96}$$

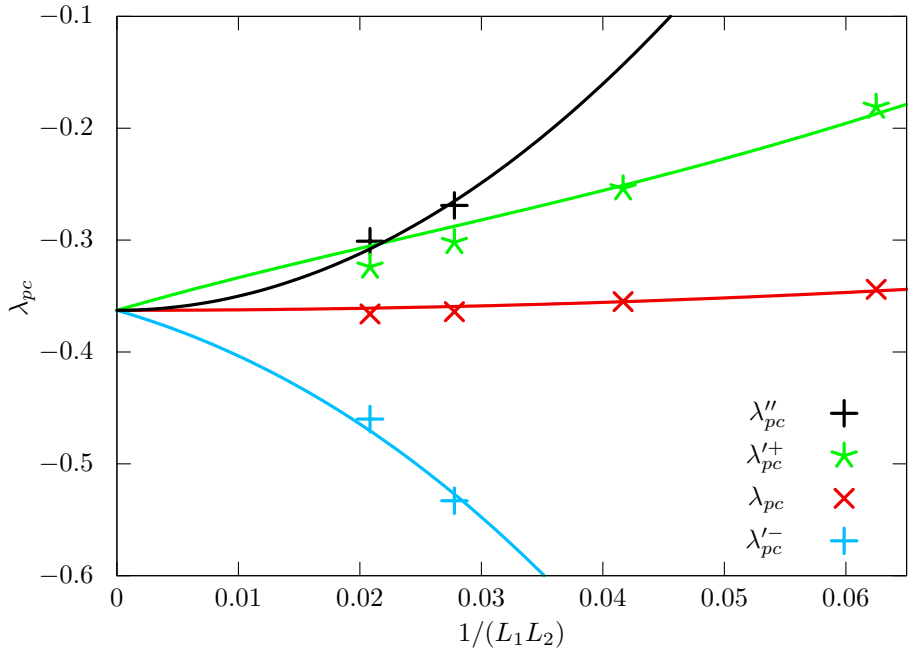

Figure 4.3: Global fit results for the L_1L_2-dependence of the crossing points λ_{pc}, λ'^{+}_{pc}, λ'^{-}_{pc} and λ''_{pc}.

and the string tension

$$\alpha = \sqrt{\frac{\rho\delta_c}{2}} = 0.04 \pm 0.01 \, \frac{J}{a}. \tag{4.97}$$

Figure 4.3 shows the crossing points from exact diagonalization together with the fitted functions for λ_{pc}, $\lambda'^{\pm}_{pc}$ and λ''_{pc}. All the crossing points shown have been taken into account in the fit, while the missing ones are too far away from λ_c to be valid within the effective theory. Figure 4.4 shows the same comparison between exact diagonalization results and the fitted functions for the energy gaps based on equation (4.45).

Comparison of string tension values from the different calculations

We have calculated the string tension using exact diagonalization (at $\lambda = 0, -1$), the cluster algorithm (at $\lambda = -1, \lambda_c, 0$) and the effective theory (at λ_c). Note that with the cluster algorithm, we calculated the energy between a pair of charges ± 2, while the other methods calculate the energy between charges ± 1. This fact together with the observation that the string is repulsive, leads to a factor greater than two between the corresponding values. Taking into account this factor, the results from the different methods summarized in table 4.5 are in good agreement.

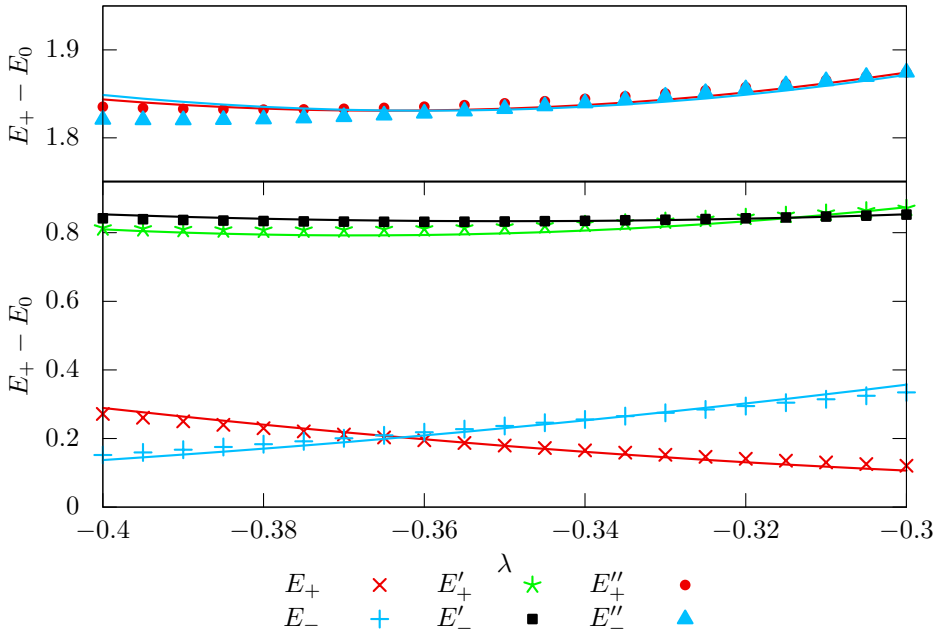

Figure 4.4: Global fit results for the energy gaps near λ_{pc} for $E_\pm$ and $E'_\pm$.

	$\lambda = -1$	$\lambda = \lambda_c$	$\lambda = 0$
Exact diag.	$\sigma_1 = 0.87 \pm 0.01\, J/a$	–	$\sigma_1 = 0.22 \pm 0.01\, J/a$
Effective theory	–	$\sigma_1 = 0.04 \pm 0.01\, J/a$	–
Cluster algorithm	$\sigma_2 = 1.91 \pm 0.01\, J/a$	$\sigma_2 = 0.16 \pm 0.01\, J/a$	$\sigma_2 = 0.46 \pm 0.01\, J/a$

Figure 4.5: Comparison of our results for the string tension from the different methods. Note that the cluster algorithm measures the string tension between charges ± 2 (and therefore σ_2) instead of ± 1 (and σ_1). This accounts for at least a factor of two difference between the results.

5 The Quantum Dimer Model

As mentioned in the introduction, quantum dimer models implement Anderson's ideas of resonating valence bonds [11] as a potential route towards understanding high-temperature superconductivity and have been investigated extensively already. However, several approaches have led to different conjectures for the phase diagram. As quantum dimer models can be described using the language of quantum link models, we will use our previously developed tools and methods to investigate them and settle some of the questions raised in previous works.

This chapter will follow a similar structure as our discussion of the $U(1)$ quantum link model. After defining the model and showing the connection to quantum link models, we will present exact diagonalization results, followed by results based on simulations with a Metropolis algorithm working again in a dual formulation. Finally, this leads to the formulation of an effective theory similar to the one presented in chapter 4.

5.1 Definition and relation to quantum link models

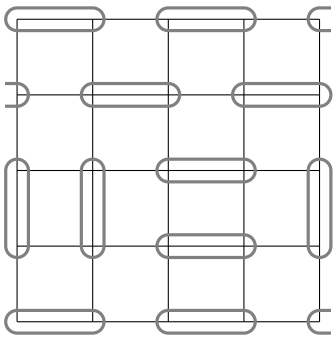

Figure 5.1: Example of a valid configuration of dimers in the quantum dimer model.

The quantum dimer and the $U(1)$ quantum link model actually share the same Hamiltonian, even though they are usually expressed with different variables. The dimer model is usually defined in terms of dimers connecting neighboring lattice sites and representing spin $\frac{1}{2}$ singlet pairs. We therefore work with a variable $D_{x,i} \in \{0, 1\}$ indicating the absence or presence of a dimer on the link starting at x in direction i. Additionally, there is a Gauss law that prevents

multiple dimers from connecting to the same point x, i.e. each lattice point is touched by exactly one dimer (in the absence of additional static charges). A sample configuration is depicted in figure 5.1.

In this formulation, the Hamiltonian again acts on flippable plaquettes. Here, they are pairs of parallel dimers on opposite links of a plaquette. The first term of the Hamiltonian flips them, i.e. changes them from a horizontal to a vertical configuration or vice versa. To put it differently, this part of the Hamiltonian rotates the two dimers by 90 degree. The second term counts the number of such flippable plaquettes. In dimer notation, the Hamiltonian can be written as

$$H = -J \sum_{\square} \Big[\; \Big| \; \Big\rangle \Big\langle \; \Big| + \Big| \; \Big\rangle \Big\langle \; \Big| \; \Big] \\ +J\lambda \sum_{\square} \Big[\; \Big| \; \Big\rangle \Big\langle \; \Big| + \Big| \; \Big\rangle \Big\langle \; \Big| \; \Big] . \tag{5.1}$$

From the description it is obvious that the quantum dimer model and the quantum link model Hamiltonian are actually the same, even though they act in different sectors of the Hilbert space (as will be shown below). The relation between flux and dimer variables is actually rather simple,

$$E_{x,\mu} = (-1)^{x_1+x_2} \left(D_{x,\mu} - \frac{1}{2} \right) . \tag{5.2}$$

With this, the Hamiltonian again becomes

$$H = -J \sum_{\square} \left[U_{\square} + U_{\square}^{\dagger} - \lambda \left(U_{\square} + U_{\square}^{\dagger} \right)^2 \right] . \tag{5.3}$$

As before, the Hamiltonian still commutes with the generators G_x of infinitesimal $U(1)$ gauge transformations. In allowed configurations, where every site is touched by exactly one dimer,

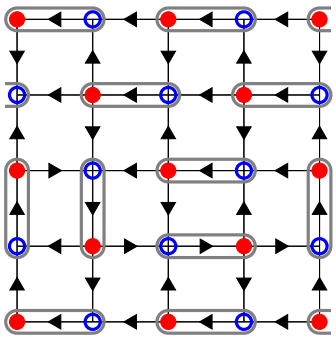

Figure 5.2: Example of a valid configuration of dimers including the corresponding flux configuration and charges.

the generators become

$$G_x = \sum_i \left(E_{x,i} - E_{x-\hat{i},i} \right) = (-1)^{x_1+x_2} \sum_i \left(D_{x,i} - D_{x-\hat{i},i} \right) = (-1)^{x_1+x_2}. \tag{5.4}$$

Therefore, the Gauss law in the dimer formulation is equivalent to a staggered background of charges ± 1 in the framework of quantum link models. While physical states in the quantum link model obey $G_x|\psi\rangle = 0$, in the quantum dimer model they obey $G_x|\psi\rangle = (-1)^{x_1+x_2}|\psi\rangle$. Figure 5.2 illustrates this by showing a dimer configuration and the corresponding flux configuration including the staggered background of charges. This also changes the possible configurations surrounding a given site. Figure 5.3 shows all configurations obeying Gauss' law locally. Additionally, we can add charges relative to this background. This leads to different numbers of dimers touching a given site, e.g. charges ± 2 lead to 3 dimers touching this specific site. Note that because of the background charges, not every charge can be placed on any site (e.g. on a site with background charge -1, only a charge $+2$ can be placed, while a charge -2 cannot).

Note that the fact that the quantum link and the quantum dimer model share a Hamiltonian also means that the RK point at $\lambda = 1$ remains as described in section 3.2.2 as will be shown below.

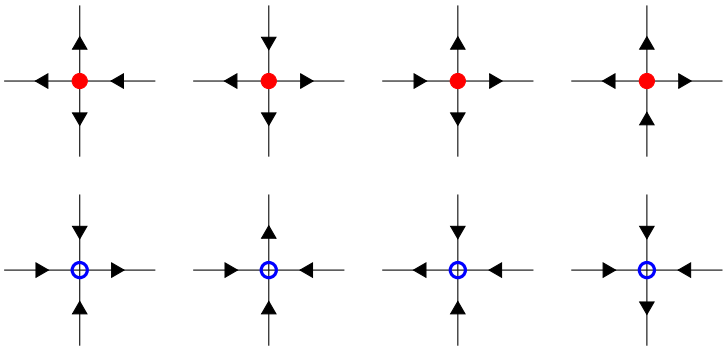

Figure 5.3: Allowed flux configurations locally at a site x for even (top) and odd (bottom) sites. Note that the ones on top lead to a charge $+1$, while the bottom row has charge -1.

5.1.1 Symmetries

As the quantum dimer model and the quantum link model share they same Hamiltonian, one would expect them to also share the same symmetries. However, due to the fact that the dimer model lives in another sector of the link model, some of the symmetries are explicitly broken by the background charges. Additionally, in the quantum link model we focused on the symmetries most relevant for the physics of the model. As the phase structure is different

in the quantum dimer model (as will be shown below), a few additional symmetries become relevant, which will be explained below. As the symmetries can be described more easily in the link formulation, we will first consider the symmetries in this formulation. Afterwards, we offer an explanation for how the relevant symmetries are represented in the dimer formulation.

Translations

Translating the lattice by one lattice spacing in either one of the two spatial directions is a symmetry of the Hamiltonian. However, due to the background of staggered charges, a translated configuration does not obey Gauss' law any longer. Note though, that translations by two lattice spacings leave the background charges intact. Therefore, the background charges explicitly break this symmetry from $\mathbb{Z}_{L_x} \times \mathbb{Z}_{L_y}$ down to $\mathbb{Z}_{L_x/2} \times \mathbb{Z}_{L_y/2}$.

Charge conjugation

In $U(1)$ quantum link models, charge conjugation is equivalent to flipping every flux to the opposite direction. Locally, this also inverts the sign of the charge at every site. Again, this means that after applying the charge conjugation transformation, the lattice does not obey Gauss' law anymore and charge conjugation alone is not a symmetry of the quantum dimer model.

Combined translations and charge conjugation

As explained before, translations as well as charge conjugation both invert the background charge at each site. This implies that the combination of both actually leaves the background intact and produces a state obeying the quantum dimer model's Gauss law. Therefore, we will consider the combinations CT_x and CT_y. In the dimer formulation, these are equivalent to ordinary lattice translations of the dimers as can be easily worked out. Therefore, from here on, we will call this combination "translations" of the quantum dimer model.

Rotations

In the quantum dimer model we can distinguish two different rotational symmetries: 90 degrees rotations around either a site of the lattice or the center of a plaquette. The first ones preserve the static background charges. The latter ones change the pattern of background charges and have to be combined with charge conjugation to be a symmetry of the system. We will therefore consider rotations O around a lattice site and rotations CO' around the center of plaquettes.

Reflections

Reflections of the lattice on either the $x-$ or the $y-$ axis preserve the background charges and commute with the Hamiltonian. We will therefore also consider reflections R_x and R_y.

$U(1)$ center symmetry and conserved global fluxes

Even though charges have an influence on the conserved global fluxes stemming from the $U(1)$ center symmetry, the specific staggered, but symmetric way the background charges are present in the dimer model still preserves this symmetry. It actually remains exactly the same as in the quantum link model. Therefore, we can still categorize the states by their global fluxes (E_x, E_y).

5.1.2 Conjectured phases

As the quantum dimer model has been studied quite extensively already, people have come up with different possible phases. They all differ by the patterns of dimer coverings they produce. However, the question which of these is actually realized for certain values of the parameter λ had not been conclusively answered before our own investigations. Figure 5.4 shows cartoon pictures of these phases.

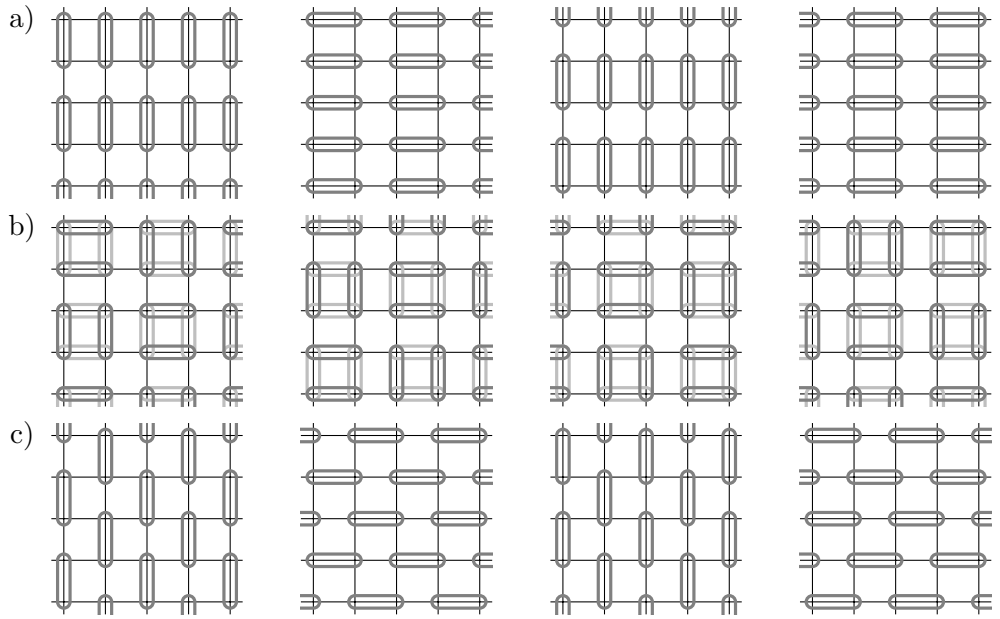

Figure 5.4: Possible phases of the quantum dimer model: a) Columnar, b) plaquette, and c) staggered order. Additionally a mixed phase that shares features of both columnar and plaquette phase was conjectured.

a) Columnar phase

The first one (in figure 5.4) is called the columnar phase. It breaks the translation symmetry in either the x- or the y-direction (but not both) as can be seen from its transformation properties listed in table 5.5. The same is true for the reflections R_x and R_y, while the rotations O and CO' are both broken. Additionally, it maximizes the number of flippable plaquettes. Note that in the quantum dimer model at most half the plaquettes can be flippable. They can be arranged either horizontally or vertically and on either the even or the odd sublattice. Therefore, there are four ways to realize this phase.

S	CT_x	CT_y	O	CO'	R_x	R_y
${}^S1$	1	3	2	4	3	1
${}^S2$	4	2	3	3	2	4
${}^S3$	3	1	4	2	1	3
${}^S4$	2	4	1	1	4	2

Figure 5.5: Transformation properties of the four columnar phases 1, 2, 3, 4 under the symmetries $S = CT_x$, CT_y, O, CO', R_x and R_y.

b) Plaquette phase

The plaquette phase breaks the translation symmetry in both directions, CT_x and CT_y, as shown in table 5.6. Additionally it also breaks R_x and R_y, as well as O and CO'. The dimers are arranged to produce flippable plaquettes in a staggered fashion, in such a way that only every fourth plaquette is flippable and in a state resonating between the two flippable configurations on each of those plaquettes. Figure 5.4 b) shows the four cartoon configurations belonging to this phase.

S	CT_x	CT_y	O	CO'	R_x	R_y
^{S}A	D	B	B	C	B	D
^{S}B	C	A	C	B	A	C
^{S}C	B	D	D	A	D	B
^{S}D	A	C	A	D	C	A

Figure 5.6: Transformation properties of the four plaquette phases A, B, C, D (right) under the symmetries $S = CT_x$, CT_y, O, CO', R_x and R_y.

c) Staggered phase

The main difference of the staggered phase compared to the other ones is that it breaks the $U(1)$ center symmetry as its favored configurations carry non-zero flux. Additionally, it also breaks translation symmetry in both the x- and y-direction (but, in contrast to the above phases, not their product CT_xCT_y) and it minimizes the number of flippable plaquettes. This leads to the staggering of the dimers shown in figure 5.4 c).

d) Mixed phase

The mixed phase shares features of both the columnar and the plaquette phases, leading to the transformation properties shown in table 5.7. It breaks all the symmetries mentioned above, except for the $U(1)$ center symmetry.

S	CT_x	CT_y	O	CO'	R_x	R_y
^{S}A1	D1	B3	B2	C4	B3	D1
^{S}A2	D4	B2	B3	C3	B2	D4
^{S}B2	C4	A2	C3	B3	A2	C4
^{S}B3	C3	A1	C4	B2	A1	C3
^{S}C3	B3	D1	D4	A2	D1	B3
^{S}C4	B2	D4	D1	A1	D4	B2
^{S}D4	A2	C4	A1	D1	C4	A2
^{S}D1	A1	C3	A2	D4	C3	A1

Figure 5.7: Transformation properties of the eight mixed phases A1, A2, B2, B3, C3, C4, D4, D1 under the symmetries $S = CT_x$, CT_y, O, CO', R_x and R_y.

Possible phase structures

In the limit $\lambda \to -\infty$, the system maximizes the number of flippable plaquettes, thus leading to one of the four columnar phases depicted in figure 5.4(a). In the opposite limit, $\lambda \to \infty$, the system minimizes the number of flippable plaquettes, which leads to one of the four staggered phases. This observation still leaves the question of what happens in between. Three possible scenarios are shown in figure 5.8. There can either be a direct transition from the columnar to the staggered phase at the RK point as shown in figure 5.8(a) or there can be other phases in-between. This question has been discussed controversially in the literature and several different claims have been made. While, based on Green's function Monte Carlo, [66] reported evidence for a phase transition separating the columnar from the plaquette phase near $\lambda \approx 0.6$, using exact diagonalization as well as Green's function Monte Carlo simulations

on moderate-size lattices, [67] suggested the possible existence of a mixed phase for $0 \lesssim \lambda < 1$. These two scenarios are shown in figure 5.8(b) and (c), respectively. Apart from also using exact diagonalization, we will settle this question by applying a Monte Carlo method on much larger systems than what was previously possible, showing the first scenario to actually be realized.

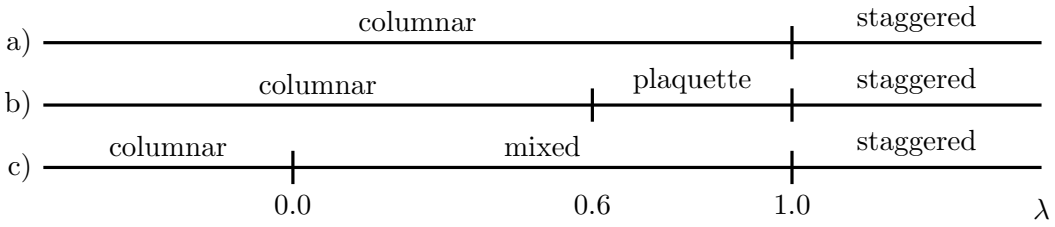

Figure 5.8: Possible phase structures of the quantum dimer model as a function of λ with either a direct transition from the columnar to the staggered phase (a), an intermediate plaquette (b) or mixed phase (c).

5.2 Exact diagonalization results

As the quantum dimer model actually is a special kind of $U(1)$ quantum link model, the exact diagonalization works exactly as before with the only change being the addition of the background of staggered static charges. Therefore, we can again consider the spectrum as a function of λ to identify the symmetry properties of the groundstate and the states degenerate with it. Additionally, we can also examine if there is a phase transition at some point and whether we can formulate an effective theory for it. Remarkably, due to the background of staggered static charges, on a given lattice, there are fewer states for the quantum dimer model than for the quantum link model (though the number still grows exponentially). This can be seen by comparing the number of allowed configurations locally at a site in the quantum dimer model (c.f. figure 5.3) and the quantum link model (c.f. figure 2.3). For the link model, there are six allowed configurations, while for the dimer model one can only chose between four possibilities. In exact diagonalization calculations, this implies that we can reach somewhat larger lattices, i.e. instead of only 6×8 lattices, we were able to reach 8×8 lattices.

Note that for all results for the quantum dimer model (independent of whether they are from exact diagonalization or from simulations), we only consider square lattices with even by even lattice extents. The restriction to even lattice is the same (and for the same reasons) as in the quantum link model, while the restriction to square lattices is due to the fact that we will be interested in the momentum sectors with $(CT_x, CT_y) = (\pi, 0)$ and $(0, \pi)$ which are

exactly degenerate on square lattices, but non-degenerate on other lattices.

5.2.1 Phase diagram

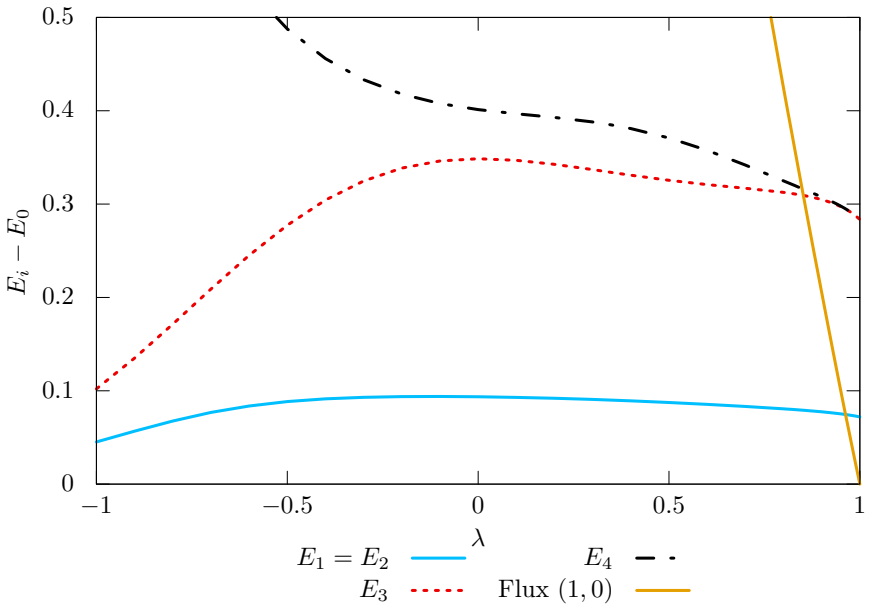

Figure 5.9: Energy gaps of the lowest lying eigenstates on an 8×8 lattice as a function of λ. Notably, the RK point at $\lambda = 1$ is present also in the quantum dimer model as evidenced by the vanishing energy gap of the state carrying flux $(1, 0)$ at $\lambda = 1$.

As for the quantum link model, the first step is to consider the states that might be degenerate with the vacuum for some values of λ. To achieve this, figure 5.9 shows the lowest energy states as a function of λ on an 8×8 lattice. As one might expect, the groundstate is non-degenerate for $\lambda < 1$ and a singlet under all symmetry operations, i.e. it has momentum $(CT_x, CT_y) = (0, 0)$ and zero flux in both directions. The first excited state in this whole region is the two-fold degenerate state with energies $E_1 = E_2$, zero flux and momenta $(CT_x, CT_y) = (\pi, 0)$ and $(CT_x, CT_y) = (0, \pi)$, respectively. After this, the third state with energy E_3 has zero flux and momentum $(CT_x, CT_y) = (\pi, \pi)$, while the fourth state has again the same quantum numbers as the groundstate, i.e. it has momentum $(CT_x, CT_y) = (0, 0)$ and no flux. The last state in figure 5.9 shows the lowest lying state with non-zero flux. It shows that the RK point is also present in the quantum dimer model and that it displays the same behavior as already described in section 3.2.2, i.e. states carrying non-zero flux become exactly degenerate with the groundstate at $\lambda = 1$ and the system becomes exactly solvable.

Let us consider the behavior of the relevant states as a function of the volume at $\lambda = -1$. This is shown in figure 5.10, which shares the coloring with the previous plot. We see that

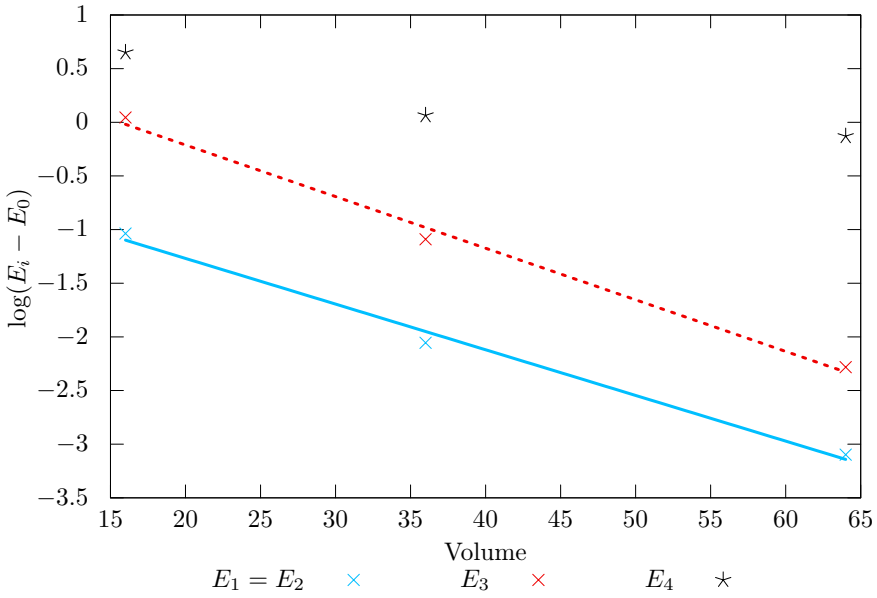

Figure 5.10: Logarithm of energy gaps of the lowest few states as a function of the volume at $\lambda = -1$. The gaps of the states with energies E_1, E_2 and E_3 decay exponentially, while the one with E_4 does not. This is again an indication of spontaneous symmetry breaking.

at $\lambda = -1$ the groundstate is most probably four-fold degenerate as the plot implies that the energy differences of both $E_1 = E_2$ and E_3 to the groundstate decay exponentially with the volume. Thus, the translation symmetry CT_i in either direction (as well as their combination) is spontaneously broken. Comparing this result with the possible phases shown in figure 5.4, this is evidence for a columnar phase, in agreement with previous findings. This phase seems to extend until around $\lambda \approx -0.2$. For larger values of λ, the situation is described in the next section as the symmetry breaking pattern is not the only important observation in this phase as another phenomenon emerges.

5.2.2 Rotor spectrum

In the quantum link model, we had two distinct phases with a phase transition in between which showed a rotor spectrum only at this specific point. In the quantum dimer model, the situation is quite different. One could say that here this single point has been turned into an elongated phase extending from around $\lambda \approx -0.2$ (almost) up to the RK point. This is evidenced by figure 5.11. After the first four states already described before, we again have a degenerate pair of states with energies $E_5 = E_6$ with the same quantum numbers as the states with $E_1 = E_2$. Afterwards, there is again a non-degenerate pair of states with energies E_7, E_8

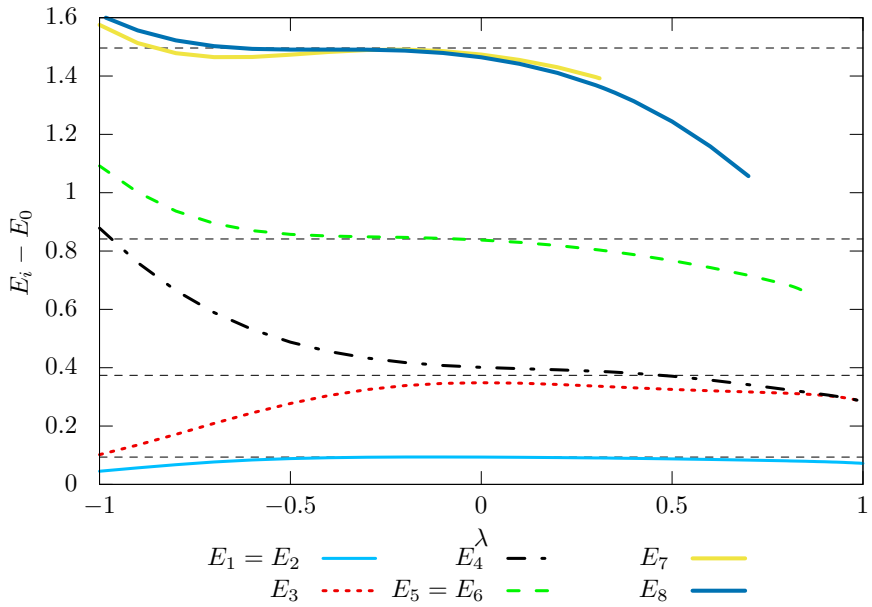

Figure 5.11: Energy gaps of the lowest states on an 8×8 lattice as a function of λ. The dashed lines have the ratios $1 : 4 : 9 : 16$, hinting at a rotor spectrum similar to what is present in the quantum link model, though here it is not only realized at one specific point, but in a larger region.

and momentum eigenvalues $(CT_x, CT_y) = (0, 0)$, $(CT_x, CT_y) = (\pi, \pi)$, respectively. These are again the same as the quantum numbers of the states with energies E_3 and E_4. Note also that both of these pairs of non-degenerate states become almost degenerate in the region specified above. While in the quantum link model we found a pattern of two alternating states that kept repeating, we now have a pattern of four such states. Additionally, the straight lines in the plot indicate ratios of $E_{1,2} : E_{3,4} : E_{5,6} : E_{7,8} \approx 1 : 4 : 9 : 16$. All this together is again evidence for a (spontaneously broken) $\mathbb{R}P(1)$ rotor symmetry. Here, however, the pattern of four states actually indicates that the symmetry is broken down to $\mathbb{Z}(8)$ instead of $\mathbb{Z}(4)$. In the next sections we will take a look at this in more detail with data from simulations based on a Metropolis algorithm as well as an effective theory similar to the one we developed for the quantum link model. Additionally, these results do not indicate the emergence of another phase before the RK point at $\lambda = 1$. However, this question cannot be settled on the small lattices accessible by exact diagonalization and will also be considered in more detail below.

5.3 Monte Carlo simulations

As the quantum dimer model can be expressed in the same language as the quantum link model, we expect that a dual representation very similar to what we have developed previously

exists. However, as will be explained in the next section, some modifications are necessary. This is because the formulation for the link model only allows charges 0 and ± 2, which would prevent us from implementing the background of staggered charges ± 1. However, with a small modification, it is possible to change this. A simple but efficient Metropolis algorithm is then constructed using dual height variables, which we will use to explore the phase structure of the model in more detail.

5.3.1 Dualization

In order to formulate a dual theory of the quantum dimer model, we start with what we already have: The representation of the dimer model in terms of the quantum link model and a dual theory to the latter one. However, as explained previously, the dual theory needs to be modified as in its current form it only allows for charges 0 and ± 2, while the dimer model requires charges ± 1. Comparing figures 5.3 and 2.3 reveals that the allowed configurations per site differ by one link being flipped relative to each other. Therefore, the transformation rules have to be changed for exactly one link per site. We will do this by adding so-called Dirac strings to these configurations. Figure 5.12 shows the configuration of Dirac strings we use. They are depicted by the rectangles shown on every second link in the horizontal direction.

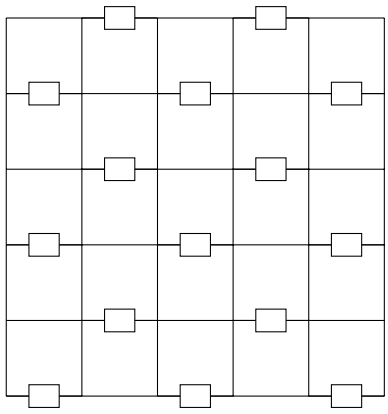

Figure 5.12: Positioning of the Dirac strings (shown as rectangles on the links) we use in formulating the dual representation. Note that every site is touched by exactly one link with a Dirac string.

The Dirac strings have one simple effect: They invert the rules connecting flux and height variables. This means that for a link carrying a Dirac string, the adjoining height variables have the same value if the flux on the link is positive, while they are different otherwise. The rules for links without Dirac string are unchanged, i.e. figures 3.10 and 3.11 are still valid for those links. Figure 5.13 shows the additional rules for links carrying a Dirac string.

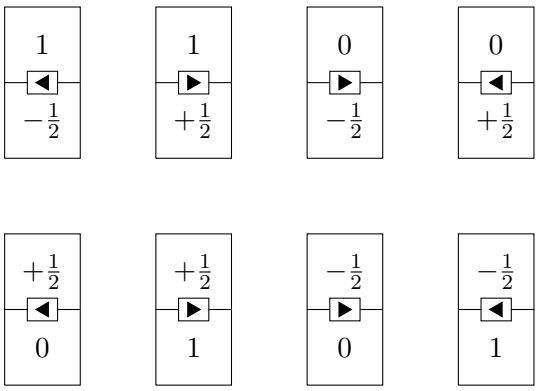

Figure 5.13: Relation between the height and the flux variables on even-odd (first row) and odd-even (second row) plaquette pairs enclosing a Dirac string.

Mathematically, the relations between height and flux variables get slightly changed and we now have to differentiate between the two lattice directions. This yields

$$E_{x,\hat{1}} = \left[h^X_{\widetilde{x}} - h^{X'}_{\widetilde{x}+\hat{2}}\right] \mod 2 = \pm\frac{1}{2}, \tag{5.5}$$

$$E_{x,\hat{2}} = (-1)^{x_1+x_2}\left[h^X_{\widetilde{x}} - h^{X'}_{\widetilde{x}+\hat{1}}\right] \mod 2 = \pm\frac{1}{2}. \tag{5.6}$$

Apart from these modifications, the rest of the dualization works just as before. We still have 16 possible height configurations which correspond to the 8 allowed configurations presented above when one takes into account the double counting of states in the height formulation.

5.3.2 Boltzmann weights and algorithm

As the quantum link model and the quantum dimer model share the same Hamiltonian, we can again use the transfer matrix 3.13 to calculate the Boltzmann weights for the height variables. We just have to identify how the flippable plaquettes are now represented. The only difference is due to the Dirac strings we had to introduce on certain links. Contrary to the previous considerations, we now have to distinguish between even and odd dual sites (plaquettes) as they differ by the relative position of the Dirac strings. Figure 5.14 shows the results of working this out for even lattices, while 5.15 shows odd plaquettes. Note that with our definition, all plaquettes on the even sublattice have a Dirac string on the bottom link, while the ones on the odd sublattice have them on their upper horizontal link. As can be easily seen, these configurations differ from the ones for the quantum link model by exactly one height variable, namely the one that is next to the Dirac string.

Similar to the quantum link model, we again Trotterize the lattice and split each timeslice into two separate slices, containing the even and odd height variables, respectively. With this, a plaquette is again defined by six heights, where four of them are arranged in one

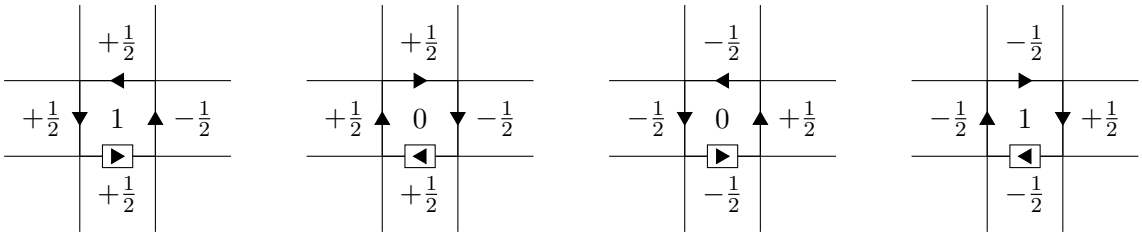

Figure 5.14: Flippable plaquettes on even sites and their representation with the dual height variables in the quantum dimer model. Note the Dirac string on the lower horizontal link, which leads to a different height configuration than what we had for the quantum link model.

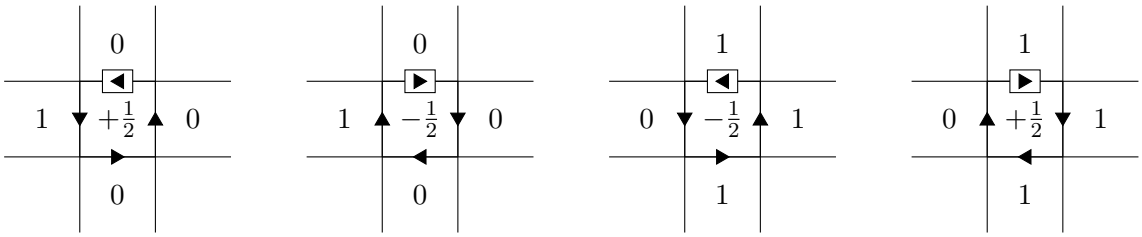

Figure 5.15: Flippable plaquettes on odd sites and their representation with the dual height variables in the quantum dimer model. Note the Dirac string on the upper horizontal link, which leads to a different height configuration than what we had for the quantum link model.

timeslice, while another one is located on the previous timeslice and the last one is on the next timeslice. The plaquette is flippable if the four in-plane height variables are in one of the two configurations shown above. If the remaining two height variables have the same value, then this plaquette is not flipped in this time step. If they differ, then the flux around the plaquette changes direction. Figure 5.16 shows the two possibilities for a flipping plaquette for even and odd plaquettes, respectively.

We found that a simple, local Metropolis algorithm in the dual height formulation actually works surprisingly efficiently and allows us to reach large lattice sizes. As explained before, this is the major difference of our approach to previous attempts. It works well in part because flipping a single height variable with the Metropolis algorithm actually corresponds to a non-trivial configuration change in the link (and dimer) representation. The simulations thus allow us to carefully investigate the phase structure while having the (rather) strong finite size effects under control. The algorithm works by using the weights calculated in section 3.3.1 to calculate the effect of a single height flip on the action and, based on this, to either accept or reject this step. As we have seen, such a flip is allowed only, if the relevant heights are in one of the configurations shown in figure 5.16. This leads to an acceptance rate

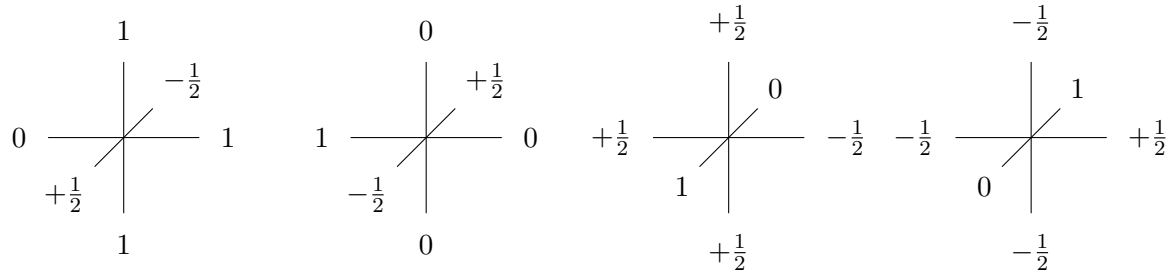

Figure 5.16: Possible realizations of plaquettes that flip in a time step in the dual formulation with height variables in the quantum dimer model for even (left) and odd (right) plaquettes.

of only a few percent. However, when a sufficiently large statistics is collected, the method works very well and easily outperforms the previously used Green's function Monte Carlo algorithm. In particular, it allows us to access volumes as large as 144^2 and temperatures as low as $T = J/500$. As this algorithm is based on local updates only, it cannot change from one flux sector to another, but this is not a problem as we know that the groundstate has zero flux (up to the RK point).

5.3.3 Order parameters

In the quantum link model, the height variable formulation leads to two different reference configurations, one for the even and one for the odd sublattice. This naturally leads to a two dimensional order parameter. As we have seen, in the quantum dimer model we have four different reference configurations, two on each sublattice. Therefore, the same construction as before leads to a set of four order parameters. In order to define them, we split both sublattices again, ending up with four sublattices A, B, C and D, arranged as shown in figure 5.17.

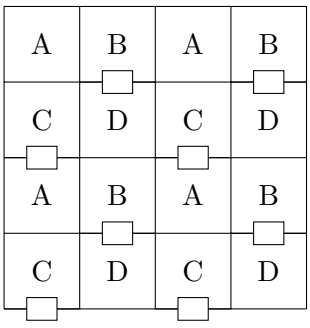

Figure 5.17: Definition of the four sublattices on which the order parameters are defined.

Using this, the order parameters can be written in a form very similar to what we have for

the quantum link model, by defining

$$M_X = \sum_{\widetilde{x}\in X} s^X_{\widetilde{x}} h^X_{\widetilde{x}}, \quad X \in \{A, B, C, D\}, \tag{5.7}$$

where

$$s^A_{\widetilde{x}} = \frac{1}{2}\left((-1)^{(\widetilde{x}_1+\frac{1}{2})/2} - 1\right), \qquad s^B_{\widetilde{x}} = (-1)^{(\widetilde{x}_1-\frac{1}{2})/2}, \tag{5.8}$$

$$s^C_{\widetilde{x}} = \frac{1}{2}\left((-1)^{(\widetilde{x}_1+\frac{1}{2})/2} - 1\right), \qquad s^D_{\widetilde{x}} = (-1)^{(\widetilde{x}_1-\frac{1}{2})/2}. \tag{5.9}$$

Figure 5.18 shows a graphical representation of the four sign variables $s^X_{\widetilde{x}}$ and their location on the four sublattices.

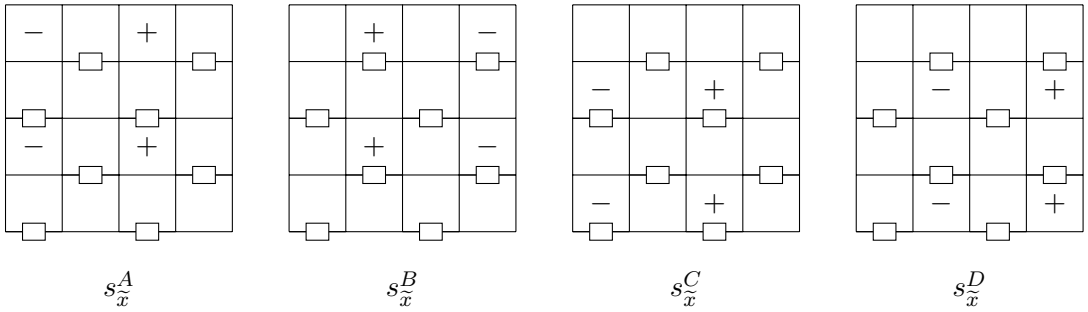

Figure 5.18: Signs of the four reference configurations and their arrangement on the four sublattices.

The fact that we now have a four-dimensional order parameter leaves us with a more extensive choice of basis. In the quantum link model this choice was unimportant as we were limited to rotations within a two-dimensional space which do not change the expected peak structure in any non-trivial way. Here, however, we work with two-dimensional projections of the four-dimensional space and this degree of freedom becomes relevant. Analyzing the symmetry transformation properties of the four order parameter suggests that a linear combination of them is more appropriate for distinguishing the different candidate phases. We therefore define

$$M_{11} = M_A - M_B - M_C + M_D = M_1 \cos(\varphi_1), \tag{5.10}$$

$$M_{22} = M_A + M_B - M_C - M_D = M_1 \sin(\varphi_1), \tag{5.11}$$

$$M_{12} = M_A - M_B - M_C - M_D = M_2 \cos(\varphi_2), \tag{5.12}$$

$$M_{21} = -M_A + M_B - M_C - M_D = M_2 \sin(\varphi_2). \tag{5.13}$$

Table 5.19 lists the transformation properties of these order parameters under the relevant symmetries. The angles φ_1 and φ_2 can be combined to

$$\varphi = \frac{1}{2}\left(\varphi_1 + \varphi_2 + \frac{\pi}{4}\right). \tag{5.14}$$

S	CT_x	CT_y	O	CO'	R_x	R_y
$M_{11}[{}^S\mathcal{C}]$	-$M_{11}[\mathcal{C}]$	-$M_{22}[\mathcal{C}]$	$M_{21}[\mathcal{C}]$	-$M_{21}[\mathcal{C}]$	-$M_{22}[\mathcal{C}]$	-$M_{11}[\mathcal{C}]$
$M_{12}[{}^S\mathcal{C}]$	$M_{21}[\mathcal{C}]$	-$M_{12}[\mathcal{C}]$	-$M_{11}[\mathcal{C}]$	-$M_{22}[\mathcal{C}]$	-$M_{12}[\mathcal{C}]$	$M_{21}[\mathcal{C}]$
$M_{21}[{}^S\mathcal{C}]$	$M_{12}[\mathcal{C}]$	$M_{21}[\mathcal{C}]$	-$M_{22}[\mathcal{C}]$	-$M_{11}[\mathcal{C}]$	$M_{21}[\mathcal{C}]$	$M_{12}[\mathcal{C}]$
$M_{22}[{}^S\mathcal{C}]$	$M_{22}[\mathcal{C}]$	-$M_{11}[\mathcal{C}]$	-$M_{12}[\mathcal{C}]$	-$M_{12}[\mathcal{C}]$	-$M_{11}[\mathcal{C}]$	$M_{22}[\mathcal{C}]$

Figure 5.19: Transformation properties of the order parameters M_{ij} under the symmetries $S = CT_x$, CT_y, O, CO', R_x, R_y. The order parameter $M_{ij}[{}^S\mathcal{C}]$ evaluated in the transformed configuration ${}^S\mathcal{C}$ as a function of the order parameters $M_{ij}[\mathcal{C}]$ evaluated in the original configuration $\mathcal{C}$.

As in the quantum link model, changing the sign of all order parameters at the same time has no physical effect due to the 2 : 1 relation between height and flux variables. This means that also $\pm(M_{11}, M_{22}, M_{12}, M_{21})$ (and thus φ and $\varphi+\pi$) represent the same physical configuration. In the columnar phase, we have $\varphi = 0 \mod \frac{\pi}{4}$, while in the plaquette phase $\varphi = \frac{\pi}{8} \mod \frac{\pi}{4}$. A mixed phase has eight different realizations related by symmetry transformations. All four components of the order parameters vanish in the four staggered phases, which thus cannot be distinguished from one another by this order parameter. These characteristic order parameter distributions are illustrated in figure 5.20. The mixed phases A1, A2, B2, B3, C3, C4, D4, and D1 share features of both columnar and plaquette phases. In particular, at a phase transition separating the columnar and the mixed phase, the peaks in the order parameter distribution corresponding to the four columnar phases 1, 2, 3, and 4 would each split into two separate peaks. For example, 1 would split into D1 and A1, and 2 would split into A2 and B2. Similarly, at a phase transition separating a mixed from a plaquette phase, the peaks in the order parameter distribution corresponding to the eight mixed phases would merge pairwise to form the peaks corresponding to the four plaquette phases A, B, C, and D. For example, A1 and A2 would merge to A, and B2 and B3 would merge to B. However, no such merging or splitting of peaks is observed in any of our simulations.

5.3.4 Results

Green's function Monte Carlo simulations of quantum dimer models have been performed in [65, 66, 67] on systems of size up to 48^2. While [66] reached the conclusion that the columnar phase turns into the plaquette phase near $\lambda \approx 0.6$, [67] interpreted the data in terms of a mixed phase that shares features of the columnar and the plaquette phase. Here we apply our new numerical method on volumes up to 144^2, and will conclude that the columnar phase extends all the way to the RK point.

Figure 5.21 shows the probability distribution $p(M_{11}, M_{22})$ for $L_1 = L_2 = 24$ at $\lambda = -0.5$

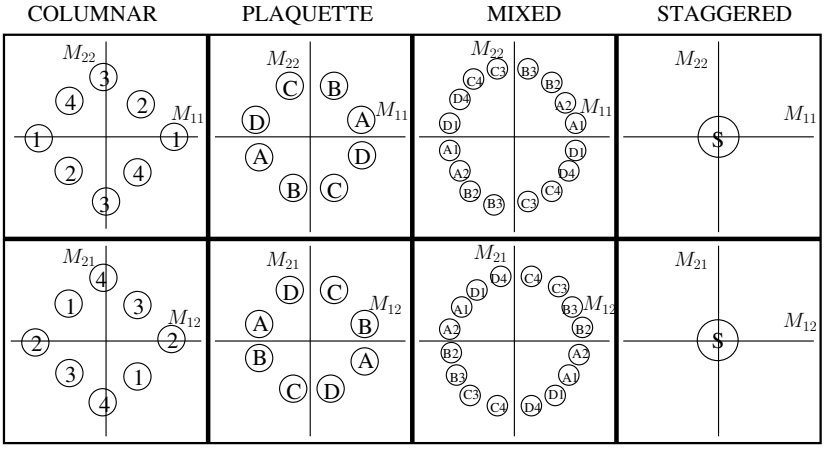

Figure 5.20: Characteristic order parameter distributions of the various candidate phases: columnar, plaquette, mixed and staggered.

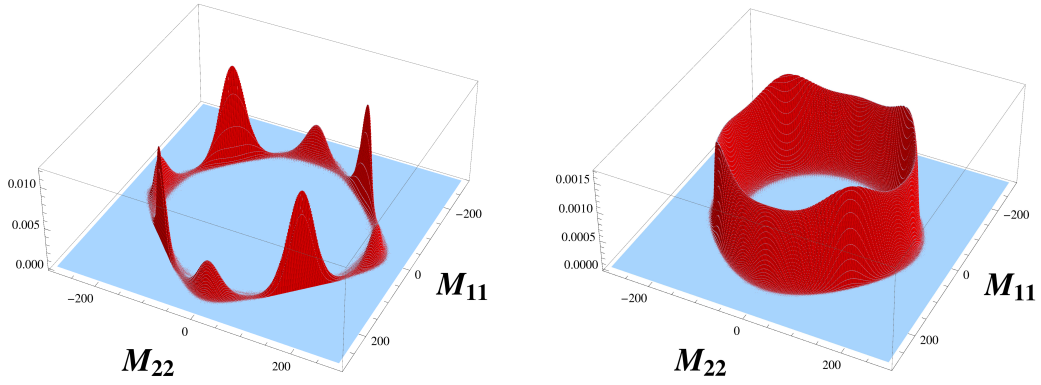

Figure 5.21: Probability distribution $p(M_{11}, M_{22})$ at $\lambda = -0.5$, $\beta J = 50$ (left) and $\lambda = 0.8$, $\beta J = 100$ (right) on a lattice with $L_1 = L_2 = 24$.

and 0.8, respectively. While the left plot clearly shows an 8 peak structure, the one on the right reveals an emergent approximate spontaneously broken $SO(2)$ symmetry similar to what we have seen at the phase transition in the quantum link model. From the exact diagonalization results shown previously, we can estimate that this effect begins to occur around $\lambda \approx -0.2$.

As will be described in more detail in the next section, the spontaneously broken $SO(2)$ symmetry again leads to an effective theory of a (pseudo-)Goldstone boson. However, it is important to note that this soft mode obscures the peak structure at moderate spatial volumes. In particular, the exact diagonalization studies which are limited to system sizes up to 8×8 cannot distinguish between the different phases, at least in the relevant regime $0 \lesssim \lambda < 1$. The previous Green's function Monte Carlo studies reached sizes up to 48^2, but did not analyze optimally suited observables to correctly identify the phase structure.

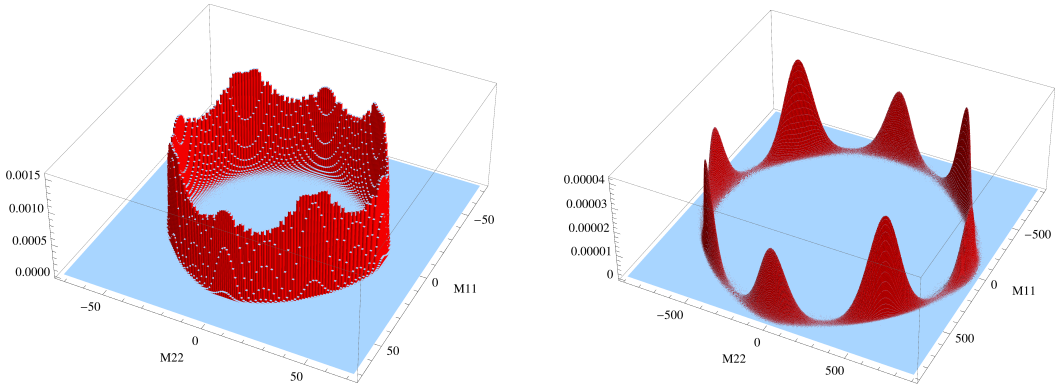

Figure 5.22: Finite-size behavior of probability distribution $p(M_{11}, M_{22})$ at $\beta J = 50$, $L_1 = L_2 = 12$ (left) and $L_1 = L_2 = 48$ (right) for $\lambda = 0.5$.

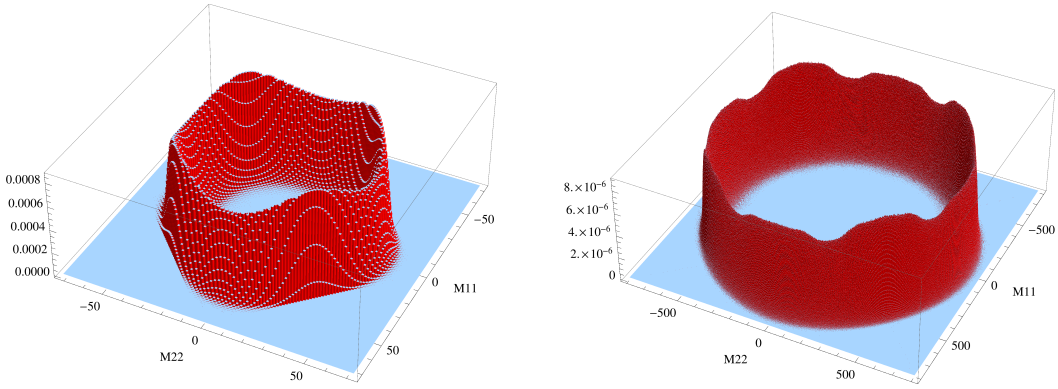

Figure 5.23: Finite-size behavior of the probability distribution $p(M_{11}, M_{22})$ at $\beta J = 50$, $L_1 = L_2 = 12$ (left) and $L_1 = L_2 = 48$ (right), for $\lambda = 0.9$.

Even with an optimally suited order parameter that is capable of distinguishing columnar, plaquette, and mixed phases, one must access sufficiently large volumes in order to draw correct conclusions about the phase diagram. As illustrated in figure 5.22, the finite size effects due to this are large. At a small temperature $\beta J = 50$, the differences between a small 12^2 system and a larger 48^2 lattice in the order parameter distributions we see are very noticeable. On the smaller lattice, we still see that the peaks are obscured by the soft mode, while on the larger system the 8 peaks structure characteristic for the columnar phase begins to stand out, especially for smaller values of λ. As shown in figure 5.23, for values closer to $\lambda = 1$, these effects are even stronger and the peak structure only begins to show, even on the 48^2 lattice.

In order to further confirm that there is no phase transition separating the columnar phase from a plaquette phase near $\lambda \approx 0.6$, we have also measured the energy density, which is shown in figure 5.24. Indeed, it is a smooth curve as a function of λ, which shows no indications of

a phase transition.

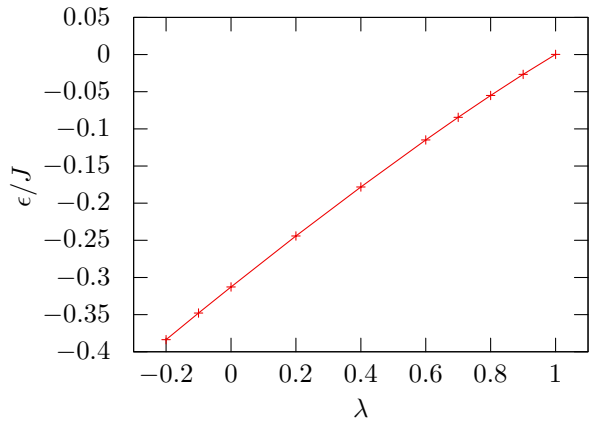

Figure 5.24: Energy density ϵ (in units of J) as a function of λ for $\beta J = 50$, $L_1 = L_2 = 48$.

Of course, one must admit that even our method, applied to systems up to about 144^2, will not be able to detect a potential phase transition very close to the RK point (e.g. for $0.95 \lesssim \lambda < 1$). It seems highly unlikely that such a phase transition could happen, simply because this regime is already very strongly dominated by the soft mode physics of the RK point. While this unlikely scenario can not be strictly ruled out, we have no numerical evidence whatsoever supporting it. We thus conclude that, at zero temperature, the columnar phase indeed extends all the way to the RK point. Only the combination of an optimally suited order parameter and a more efficient numerical method allowed us to settle the long-standing controversies related to [66, 67].

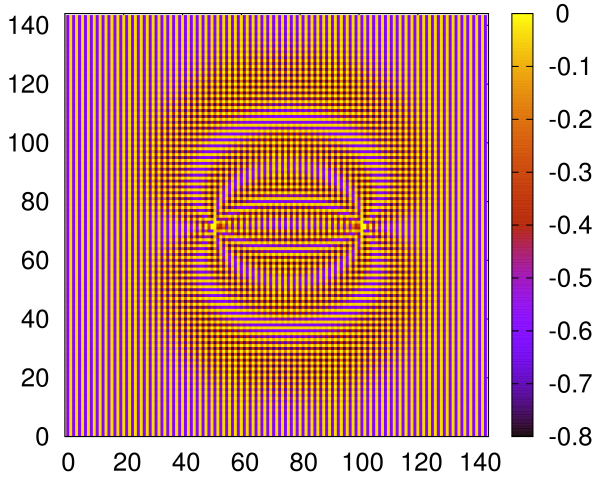

Figure 5.25: Energy density $-J\langle U_\square + U_\square^\dagger \rangle$ in the presence of two charges ± 2 (separated by 49 lattice spacings) for $\lambda = -0.2$, $\beta J = 72$, on a 144^2 lattice.

Similar to the quantum link model, we can again investigate the energy distribution on configurations with two external static charges ± 2 relative to the staggered charge background, i.e. with $G_x = -(-1)^{x_1+x_2}$ at two positions separated by an odd number of lattice spacings. This violation of the dimer covering constraint implies that three dimers touch each of those two sites, while all other sites are still touched by exactly one dimer. As in the quantum link model, the two external charges are confined by an electric flux string. Again, the total flux 2 connecting the external charges ± 2 fractionalizes into several strands. Here, however, we have not only four, but eight strands, each carrying electric flux $\frac{1}{4}$. The interior of the strands displays plaquette order and represents interfaces separating distinct columnar phases whose columns are oriented in orthogonal directions. The strands are a topological manifestation of the relevant order parameter variations. Figure 5.25 shows the energy distribution between two charges separated by 40 lattice spacings on a 144^2 lattice at $\lambda = -0.2$. The energy of the string plays the role of a confining charge-anti-charge potential $V(r) \sim \sigma r$, which is shown in figure 5.26. Deep in the columnar phase, the string tension is given by $\sigma(\lambda = -0.5) = 0.370(1)J/a$. With increasing λ, it is greatly reduced to $\sigma(\lambda = 0.5) = 0.057(1)J/a$, $\sigma(\lambda = 0.8) = 0.029(1)J/a$, and it finally vanishes at the deconfined RK point.

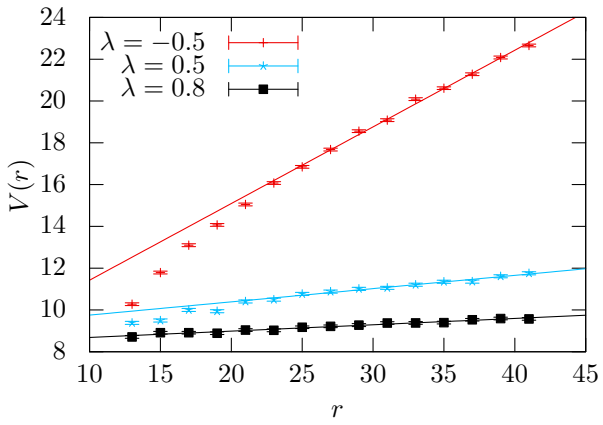

Figure 5.26: Potential between two static charges ± 2 separated by a distance r along a lattice axis, on a 120^2 lattice at $\beta J = 100$ and $\lambda = -0.5, 0.5, 0.8$.

5.4 Effective theory

As discussed previously, our exact diagonalization and simulation results both show a spontaneously broken approximate global $SO(2)$ symmetry emerging dynamically (again reduced to $\mathbb{R}P(1)$ for symmetry reasons) similar to the one found in the quantum link model. However, they differ by two important facts: First, in the quantum link model, this phenomenon

occurs at a single phase transition point, while here it is extended into a whole phase between $-0.2 \lesssim \lambda < 1$. This implies that the effects of the deconfined RK point have to be taken into account near $\lambda = 1$. Second, the degeneracy of the groundstate is twice as large, which leads to a different symmetry breaking term. With these observations, the pseudo-Goldstone boson emerging in this phase can be described by the effective action

$$S[\varphi] = \int d^3x \left[\frac{\rho}{2}\partial_i\varphi\partial_i\varphi + \frac{\rho}{2c^2}\partial_t\varphi\partial_t\varphi + \kappa\left(\partial_i\partial_i\varphi\right)^2 + \delta\cos^2(4\varphi)\right]. \tag{5.15}$$

Again, the derivative terms describe a "particle" on a circle and lead to the rotor spectrum seen in our exact diagonalization results, while the δ terms break the symmetry down to $\mathbb{Z}(8)$ (instead of $\mathbb{Z}(4)$ as was the case in the quantum link model).

5.4.1 Hamiltonian formulation and rotor spectrum

As before, we are most interested in the vacuum effects of the theory. Assuming a periodic volume $L_1 \times L_2$, we can assume (to lowest order), that φ is constant in space, i.e. $\varphi(x,t) = \varphi(t)$, which implies

$$S[\varphi] = \int dt \left[\frac{\rho L1 L_2}{2c^2}\partial_t\varphi\partial_t\varphi + \delta L_1 L_2\cos^2(4\varphi)\right]. \tag{5.16}$$

In order to calculate the spectrum of the theory, it is advisable to go to the Hamiltonian formulation of the theory. Performing the necessary transformations (while keeping in mind that the above action refers to Euclidean time) leads to the Hamiltonian

$$H = -\frac{c^2}{2\rho L_1 L_2}\partial_\varphi^2 + \delta L_1 L_2\cos^2(4\varphi). \tag{5.17}$$

Ignoring the small perturbations, i.e. setting $\delta = 0$, this describes a free particle on a circle whose eigenfunctions and energy eigenvalues are again given by

$$\psi_m(\varphi) = \frac{1}{\sqrt{2\pi}}\exp(im\varphi), \qquad E_m = \frac{m^2c^2}{2\rho L_1 L_2}. \tag{5.18}$$

As in the quantum link model, shifts by π lead again to the same configuration, because of the symmetry properties of the order parameters as φ is equivalent to the phase introduced in equations (5.13) and (5.14). Therefore, φ and $\varphi + \pi$ are physically equivalent, which implies that we should have

$$[m\varphi - m(\varphi + \pi)] = m\pi = 0 \mod 2\pi. \tag{5.19}$$

Consequently, m is restricted to even integers.

Calculating the (CT_x, CT_y) quantum numbers of the first few states (to lowest order) and comparing them to the spectrum shown in figure 5.11, we confirm that the nine states with $m = 0, \pm2, \pm4, \pm6, \pm8$ agree in both of our results. As mentioned before, these states from exact diagonalization also show the same ratios of $E_m : E_n = m^2 : n^2$.

5.4.2 Perturbative corrections to the energy spectrum

In order to be able to compare the results from the two methods in more detail, we again treat the Hamiltonian of the effective theory perturbatively and expand the energy eigenvalues in orders of δ. In contrast to the quantum link model, we will see that in this case it is enough to restrict ourselves to first order calculations only (though a more detailed calculation is in progress [71]).

Using the eigenfunctions from equation (4.4), the corrections to the (non-degenerate) groundstate in first order perturbation theory are given by

$$\begin{aligned} E_0^{(1)} &= \langle 0 \left| \delta L_1 L_2 \cos^2(2\varphi) \right| 0 \rangle \\ &= \frac{\delta L_1 L_2}{2\pi} \int_0^{2\pi} d\varphi \cos^2(4\varphi) \\ &= \frac{\delta L_1 L_2}{2\pi} \frac{1}{4} \int_0^{8\pi} d\varphi \cos^2(\varphi) \\ &= \frac{\delta L_1 L_2}{2}. \end{aligned} \tag{5.20}$$

For non-zero values of m, the states are degenerate. In order to lift this degeneracy, we will switch to using even and odd eigenfunctions, i.e. we split ψ_m into the two functions

$$\psi_m^e = \frac{1}{\sqrt{\pi}} \cos(m\varphi), \qquad \psi_m^o = \frac{1}{\sqrt{\pi}} \sin(m\varphi). \tag{5.21}$$

As we will see, in this basis the two energy eigenvalues are non-degenerate when adding the effects of the perturbations. With this we can now calculate the corrections

$$E_m^{e,(1)} =_e \langle m \left| \delta L_1 L_2 \cos^2(2\varphi) \right| m \rangle_e = \frac{\delta L_1 L_2}{2\pi} \int_0^{2\pi} d\varphi \cos^2(4\varphi) \cos^2(m\varphi) \tag{5.22}$$

and

$$\begin{aligned} E_m^{o,(1)} &=_o \langle m \left| \delta L_1 L_2 \cos^2(2\varphi) \right| m \rangle_o +_o \langle m \left| \epsilon L_1 L_2 \cos^4(2\varphi) \right| m \rangle_o \\ &= \frac{\delta L_1 L_2}{2\pi} \int_0^{2\pi} d\varphi \cos^2(2\varphi) \sin^2(2\varphi) + \frac{\epsilon L_1 L_2}{2\pi} \int_0^{2\pi} d\varphi \cos^4(2\varphi) \sin^2(2\varphi). \end{aligned} \tag{5.23}$$

When evaluating the integral, one finds a dependence of the results on m. Expressed in terms of the energy differences to the groundstate, the calculation yields

$$E_m^{e/o,(1)} + E_m^{e/o,(0)} - E_0^{(1)} - E_0^{(0)} = \frac{m^2 c^2}{2\rho L_1 L_2}, \qquad m \neq 4, \tag{5.24}$$

$$E_4^{e,(1)} + E_4^{e,(0)} - E_0^{(1)} - E_0^{(0)} = \frac{8c^2}{\rho L_1 L_2} + \frac{\delta L_1 L_2}{4}, \tag{5.25}$$

$$E_4^{o,(1)} + E_4^{o,(0)} - E_0^{(1)} - E_0^{(0)} = \frac{8c^2}{\rho L_1 L_2} - \frac{\delta L_1 L_2}{4}, \tag{5.26}$$

where the last line is valid for all $|m| > 4$. Returning to the notation from section 5.2, the relevant energy differences then become

$$E_1 = E_2 = \frac{2c^2}{\rho L_1 L_2}, \tag{5.27}$$

$$E_3 = \frac{8c^2}{\rho L_1 L_2} + \frac{\delta L_1 L_2}{4}, \tag{5.28}$$

$$E_4 = \frac{8c^2}{\rho L_1 L_2} - \frac{\delta L_1 L_2}{4}, \tag{5.29}$$

$$E_5 = E_6 = \frac{18c^2}{\rho L_1 L_2}. \tag{5.30}$$

This is consistent with our exact diagonalization results as it also shows that only the states with energies E_3 and E_4 actually split.

5.4.3 Fit to exact diagonalization results

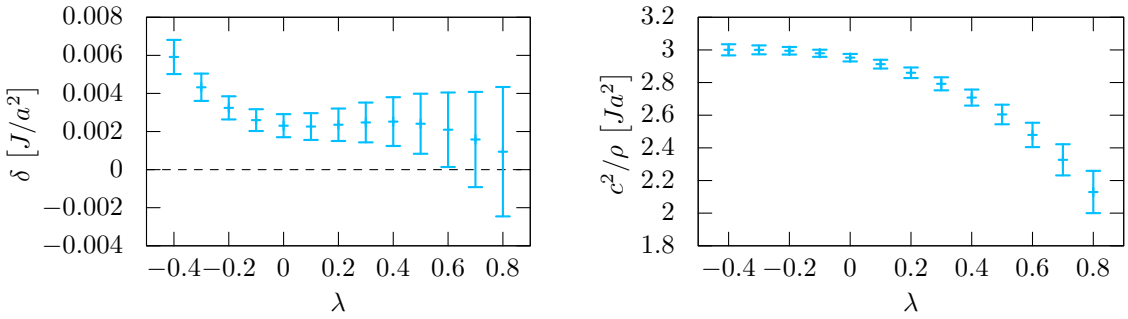

Figure 5.27: Results for the parameter δ (left) and the combination $\frac{c^2}{\rho}$ (right) of the effective theory from a fit to the exact diagonalization data for different λ for the lattice sizes 6×6 and 8×8.

Figure 5.27 shows the results for the symmetry breaking parameter δ (left) and the combination $\frac{c^2}{\rho}$ (right) of a global fit using data from 6×6 and 8×8 lattices for different values of λ. Note, that $\frac{c^2}{\rho}$ clearly remains larger than zero for all λ, while δ approaches zero near the RK point. Remarkably, the fit works rather well up to values of $\lambda \approx 0.6$, clearly showing $\delta > 0$. Even though the errors are growing large afterwards, the results are still consistent with positive values of δ, thus indicating the absence of a phase transition before the RK point. This indicates that the columnar phase exists up to $\lambda = 1$. However, the precision reachable with the small volumes from exact diagonalization is not sufficient to definitively settle this question. The next section shows different techniques based on comparing the effective theory with the results from our simulations where we can reach much larger lattices. However, this is partially still work in progress.

5.4.4 Calculations with the Metropolis algorithm for quantities of the effective theory

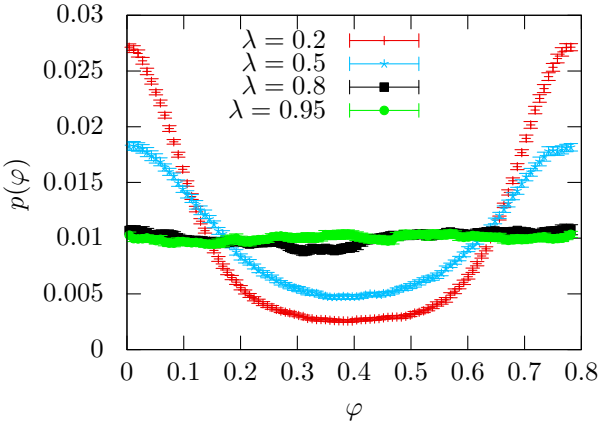

Figure 5.28: Probability distribution $p(\varphi)$ for different values of λ in the range $\varphi \in [0, \frac{\pi}{4}]$ (for symmetry reasons, this pattern repeats itself periodically).

A different approach for obtaining the value of δ uses a finite-size analysis of the probability distribution $p(\varphi)$ illustrated in figure 5.28 (work in progress).

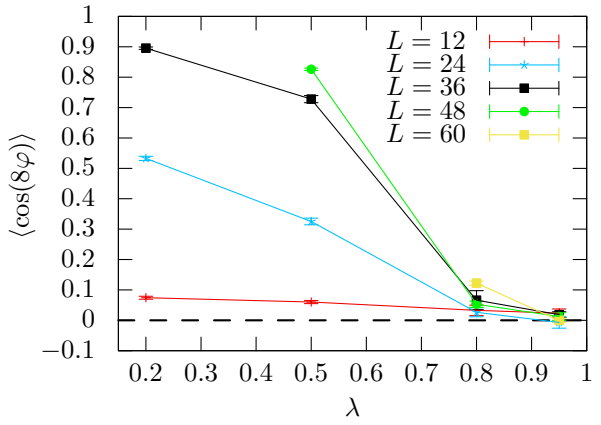

Figure 5.29: $\langle\cos(8\varphi)\rangle$ on lattices with $L_1 = L_2 = 12$ ($\beta J = 40$), 24 ($\beta J = 80$), 36 ($\beta J = 120$), 48 ($\beta J = 80$) and 60 ($\beta J = 120$), respectively.

Inspired by [77], we have determined the moment $\langle\cos(8\varphi)\rangle = \int_{-\pi}^{\pi} d\varphi \; p(\varphi)\cos(8\varphi)$ for different λ (cf. figure 5.29). We find that $\langle\cos(8\varphi)\rangle > 0$ for $\lambda < 1$, indicating that the system remains in the columnar phase all the way to the RK point.

6 Conclusions

In this thesis we investigated the (2+1)-d $U(1)$ quantum link and quantum dimer models. The framework of quantum link models provides an extension of Wilson's lattice gauge theory that may help to solve some problems in the standard approach to lattice quantum chromodynamics and in condensed matter physics in the long term. These problems include among others calculations of the physics at non-zero baryon density and of the real-time evolution of quantum systems. On the one hand, as we successfully showed here, quantum link models provide an opportunity to develop new algorithms. On the other hand, they are also suitable to be used for quantum simulations with optical lattices, which is very difficult with Wilson's lattice gauge theory.

Specifically, we investigated the (2+1)-d $U(1)$ quantum link model, calculating its phase diagram and providing further numerical results which may in the future be used to check quantum simulations as a first step towards quantum simulating quantum chromodynamics. In order to do this, we used exact diagonalization and a newly developed, efficient cluster algorithm based on the dual theory. This led to the formulation of an effective theory which we were able to match numerically with our other calculations. The results we obtained are highly non-trivial and are therefore interesting on their own as well. We have observed an emergent $SO(2)$ symmetry with an associated pseudo-Goldstone boson described by the effective theory. Interfaces separating phases with spontaneously broken C or T symmetry manifest themselves as strings carrying fractional electric flux $\frac{1}{2}$. Finally, our results also encourage the application of dualization techniques to quantum Hamiltonians for other theories, and, in particular, to Hamiltonians of quantum link models in higher dimensions.

In the last part of this thesis, we investigated the square lattice (2+1)-d quantum dimer model, which can be expressed as a quantum link model. This allowed us to use the techniques developed previously in order to provide new results for the phase diagram as previous results were inconclusive. We found that the model exists in a columnar phase for all values of the RK coupling $\lambda < 1$, without ever going into a plaquette phase. It will be interesting to apply our method also to other lattice geometries. As in the quantum link model, at $\lambda = 1$, the electric fluxes condense in the vacuum, thus leading to deconfinement even at zero temperature. This corresponds to the spontaneous breakdown of the $U(1)^2$ center symmetry. In the confining columnar phase, the string connecting two external static charges separates into distinct strands, each carrying a fractionalized flux $\frac{1}{4}$. The interior of the flux strands

consists of plaquette phase which does, however, not exist as a stable bulk phase. Also in this model, we have observed an approximate emergent $SO(2)$ symmetry with an associated pseudo-Goldstone boson. At $\lambda = 1$ this Goldstone boson becomes exactly massless, and can be identified with a dual photon. Remarkably, as indicated by the rotor spectrum in figure 5.11, the pseudo-Goldstone mode, which represents a soft phonon-like mode of the crystalline columnar valence bond solid, exists even away from the RK point at $\lambda \approx 0$ (in contrast to the quantum link model, where it exists only near a phase transition). It will be interesting to investigate whether this "phonon" mode persists in doped systems and whether it may be related to the formation of Cooper pairs in high-T_c superconductors.

Acknowledgements

First and foremost, I would like to thank my advisor Uwe-Jens Wiese for giving me the opportunity to work on my PhD these last four years. His support was invaluable and his advice contributed a lot to my research and this thesis. I would also like to thank Andreas Läuchli for accepting the responsibility of being the co-referee for this thesis.

A large thanks goes to Debasish Banerjee with whom I collaborated closely on most of my projects leading to this thesis. I am thankful for our countless discussions, his willingness to help with my problems and his enthusiasm.

I would also like to thank all other members of our group, especially Pascal Stebler and Michael Bögli for many discussions and the sharing of the experience of working on a PhD. A large thanks goes to my long-time office mate Kyle Steinhauer for many helpful and interesting discussions. He always listened to my questions, even while he was busy finishing his own thesis. Furthermore, I would like to thank my friends and fellow physics students Lorena Rothen, Olivier Eicher, Ramon Stucki and Martti Nirkko for sharing the way from our first physics lecture up to now.

Special thanks also to our external collaborateurs who contributed a lot to the research presented here, including Fu-Jiun Jang, Christoph Hofmann, as well as Peter Zoller and his group in Innsbruck. I would also like to express my gratitude to the secretary of our institute, Esther Fiechter, for her help with all administrative issues.

Last but not least, I thank all my friends and my family who supported me along the way.

Bibliography

[1] K. G. Wilson, *Confinement of quarks*, *Phys. Rev. D* **10** (1974) 2445.

[2] A. M. Polyakov, *Compact gauge fields and the infrared catastrophe*, *Phys. Lett. B* **59** (1975) 82.

[3] A. M. Polyakov, *Quark confinement and topology of gauge theories*, *Nucl. Phys. B* **120** (1977) 429.

[4] M. Göpfert and G. Mack, *Proof of confinement of static quarks in 3-dimensional $U(1)$ lattice gauge theory for all values of the coupling constant*, *Commun. Math. Phys.* **82** (1982) 545.

[5] M. Constantinou, *Hadron Structure*, *PoS(LATTICE 2014)* **001** (2014).

[6] T. Yamazaki, *Hadronic Interactions*, *PoS(LATTICE 2014)* **009** (2014).

[7] F. Sanfilippo, *Quark Masses from Lattice QCD*, *PoS(LATTICE 2014)* **014** (2014).

[8] S. Prelovsek, *Hadron Spectroscopy*, *PoS(LATTICE 2014)* **015** (2014).

[9] J. Hubbard, *Electron correlations in narrow energy bands*, *Proc. Roy. Soc. (London)* **A276** (1963) 238.

[10] D. S. Rokhsar and S. A. Kivelson, *Superconductivity and the Quantum Hard-Core Dimer Gas*, *Phys. Rev. Lett.* **61** (1988) 2376.

[11] P. Anderson, *The resonating valence bond state in LA_2CUO_4 and superconductivity*, *Science* **235** (1987) 1196.

[12] S. Sachdev, *Spin-Peierls ground states of the quantum dimer model: A finite-size study*, *Phys. Rev. B* **40** (1989) 5204.

[13] L. Levitov, *Equivalence of the dimer resonance-valence-bond problem to the quantum roughening problem*, *Phys. Rev. Lett.* **64** (1990) 92.

[14] P. Leung, K. Chiu, and K. Runge, *Columnar dimer and plaquette resonating-valence-bond orders in the quantum dimer model*, *Phys. Rev. B* **54** (1996) 12938.

[15] T. Moessner, S. L. Sondhi, and E. Fradkin, *Short-ranged RVB physics, quantum dimer models and Ising gauge theories*, *Phys. Rev. Lett.* **65** (2002) 024504.

[16] C. Henley, *From classical to quantum dynamics at Rokhsar–Kivelson points*, *J. Phys.: Condens. Matter* **16** (2004) 891.

[17] F. Alet, J. Jacobsen, G. Misguich, V. Pasquier, F. Mila, and M. Troyer, *Interacting classical dimers on the square lattice*, *Phys. Rev. Lett.* **94** (2005) 235702.

[18] F. Alet, Y. Ikhlef, J. Jacobsen, G. Misguich, and V. Pasquier, *Classical dimers with aligning interactions on the square lattice*, *Phys. Rev. E* **74** (2006) 041124.

[19] D. Charrier and F. Alet, *Phase diagram of an extended classical dimer model*, *Phys. Rev. B* **82** (2010) 014429.

[20] J. Cano and P. Fendley, *Spin Hamiltonians with Resonating-Valence-Bond Ground States*, *Phys. Rev. Lett.* **105** (2010) 067205.

[21] A. Albuquerque and F. Alet, *Critical correlations for short-range valence-bond wave functions on the square lattice*, *Phys. Rev. B* **82** (2010) 180408(R).

[22] Y. Tang, A. Sandvik, and C. Henley, *Properties of resonating-valence-bond spin liquids and critical dimer models*, *Phys. Rev. B* **84** (2011) 174427.

[23] C. Lamas, A. Ralko, M. Oshikawa, D. Poilblanc, and P. Pujol, *Hole statistics and superfluid phases in quantum dimer models*, *Phys. Rev. B* **87** (2013) 104512.

[24] L. Balents, *Spin liquids in frustrated magnets*, *Nature* **464** (2010) 199.

[25] M. Hermele, M. Fisher, and L. Balents, *Pyrochlore Photons: The $U(1)$ Spin-Liquid in a S=1/2 Three Dimensional Frustrated Magnet*, *Phys. Rev. B* **69** (2004) 064404.

[26] R. P. Feynman, *Simulating Physics with Computers*, *Int. J. Theor. Phys.* **21** (1982) 467.

[27] J. I. Cirac and P. Zoller, *Quantum Computations with Cold Trapped Ions*, *Phys. Rev. Lett.* **74** (1995) 4091.

[28] S. Lloyd, *Universal Quantum Simulators*, *Science* **273** (1996) 1073.

[29] D. Jaksch, C. Bruder, J. I. Cirac, C. W. Gardiner, and P. Zoller, *Cold Bosonic Atoms in Optical Lattices*, *Phys. Rev. Lett.* **81** (1998) 3108.

[30] E. Zohar and B. Reznik, *Confinement and Lattice Quantum-Electrodynamic Electric Flux Tubes Simulated with Ultracold Atoms*, *Phys. Rev. Lett.* **107** (2011) 275301.

[31] G. Szirmai, E. Szirmai, A. Zamora, and M. Lewenstein, *Gauge fields emerging from time-reversal symmetry breaking for spin-5/2 fermions in a honeycomb lattice*, *Phys. Rev. A* **84** (2011) 011611.

[32] Y. Liu, Y. Meurice, and S.-W. Tsai, *Local gauge symmetry on optical lattices?*, *PoS(LATTICE 2012)* **246** (2012).

[33] E. Zohar, J. Cirac, and B. Reznik, *Simulating Compact Quantum Electrodynamics with Ultracold Atoms: Probing Confinement and Nonperturbative Effects*, *Phys. Rev. Lett.* **109** (2012) 125302.

[34] D. Banerjee, M. Dalmonte, M. Müller, E. Rico, P. Stebler, U.-J. Wiese, and P. Zoller, *Atomic Quantum Simulation of Dynamical Gauge Fields coupled to Fermionic Matter: From String Breaking to Evolution after a Quench*, *Phys. Rev. Lett.* **109** (2012) 175302.

[35] D. Banerjee, M. Bögli, M. Dalmonte, E. Rico, P. Stebler, U.-J. Wiese, and P. Zoller, *Atomic Quantum Simulation of $U(N)$ and $SU(N)$ Non-Abelian Lattice Gauge Theories*, *Phys. Rev. Lett.* **110** (2013) 125303.

[36] E. Zohar, J. Cirac, and B. Reznik, *Cold-Atom Quantum Simulator for SU(2) Yang-Mills Lattice Gauge Theory*, *Phys. Rev. Lett.* **110** (2013) 125304.

[37] E. Zohar, J. Cirac, and B. Reznik, *Quantum simulations of gauge theories with ultracold atoms: Local gauge invariance from angular-momentum conservation*, *Phys. Rev. A* **88** (2013) 023617.

[38] U.-J. Wiese, *Ultracold quantum gases and lattice systems: quantum simulation of lattice gauge theories*, *Ann. Phys. (Berlin)* **525** (2013) 777.

[39] M. Greiner, O. Mandel, T. Esslinger, T. W. Hänsch, and I. Bloch, *Quantum Phase Transition from a Superfluid to a Mott Insulator in a Gas of Ultracold Atoms*, *Nature* **415** (2002) 39.

[40] J. T. Barreiro, M. Müller, P. Schindler, D. Nigg, T. Monz, M. Chwalla, M. Hennrich, C. F. Roos, P. Zoller, and R. Blatt, *An open-system quantum simulator with trapped ions*, *Nature* **470** (2011) 486.

[41] D. Horn, *Finite Matrix Models with Continuous Local Gauge Invariance*, *Phys. Lett. B* **100** (1981) 149–151.

[42] P. Orland and D. Rohrlich, *Lattice gauge magnets: Local isospin from spin*, *Nucl. Phys. B* **338** (1990) 647–672.

[43] P. Orland, *Exact solution of a quantum gauge magnet in (2+1)-dimensions*, *Nucl. Phys. B* **372** (1992) 635–653.

[44] S. Chandrasekharan and U.-J. Wiese, *Quantum Link Models: A Discrete Approach to Gauge Theories*, *Nucl. Phys. B* **492** (1997) 455.

[45] R. Brower, S. Chandrasekharan, S. Riederer, and U.-J. Wiese, *D-Theory: Field Quantization by Dimensional Reduction of Discrete Variables*, *Nucl. Phys. B* **693** (2004) 149.

[46] R. Brower, S. Chandrasekharan, and U.-J. Wiese, *QCD as a quantum link model*, *Phys. Rev. D* **60** (1999) 094502.

[47] A. Kitaev, *Anyons in an exactly solved model and beyond*, *Ann. Phys., NY* **321** (2006) 2.

[48] T. Sentil, A. Vishwanath, L. Balents, S. Sachdev, and M. Fisher, *Deconfined Quantum Critical Points*, *Science* **303** (2004) 1490.

[49] T. Sentil, L. Balents, S. Sachdev, A. Vishwanath, and M. Fisher, *Quantum criticality beyond the Landau-Ginzburg-Wilson paradigm*, *Phys. Rev. B* **70** (2004) 144407.

[50] A. W. Sandvik, *Evidence for Deconfined Quantum Criticality in a Two-Dimensional Heisenberg Model with Four-Spin Interactions*, *Phys. Rev. Lett.* **98** (2007) 227202.

[51] R. G. Melko and R. K. Kaul, *Scaling in the Fan of an Unconventional Quantum Critical Point*, *Phys. Rev. Lett.* **100** (2008) 017203.

[52] F.-J. Jiang, M. Nyfeler, S. Chandrasekharan, and U.-J. Wiese, *From an antiferromagnet to a valence bond solid: evidence for a first-order phase transition*, *J. Stat. Mech.* **P02009** (2008).

[53] K. Chen, Y. Huang, Y. Deng, A. B. Kuklov, N. V. Prokof'ev, and B. V. Svistunov, *Deconfined Criticality Flow in the Heisenberg Model with Ring-Exchange Interactions*, *Phys. Rev. Lett.* **110** (2013) 185701.

[54] Y. Tang and A. W. Sandvik, *Confinement and Deconfinement of Spinons in Two Dimensions*, *Phys. Rev. Lett.* **110** (2013) 217213.

[55] S. Pujari, K. Damle, and F. Alet, *Néel-State to Valence-Bond-Solid Transition on the Honeycomb Lattice: Evidence for Deconfined Criticality*, *Phys. Rev. Lett.* **111** (2013) 087203.

[56] A. F. Albuquerque, D. Schwandt, B. Hetényi, S. Capponi, M. Mambrini, and A. M. Läuchli, *Phase diagram of a frustrated quantum antiferromagnet on the honeycomb lattice: Magnetic order versus valence-bond crystal formation*, *Phys. Rev. B* **84** (2011) 024406.

[57] Z. Zhu, D. A. Huse, and S. R. White, *Weak Plaquette Valence Bond Order in the S=1/2 Honeycomb J_1-J_2 Heisenberg Model*, *Phys. Rev. Lett.* **110** (2013) 127205.

[58] R. K. Kaul and A. W. Sandvik, *Lattice Model for the $SU(N)$ Néel to Valence-Bond Solid Quantum Phase Transition at Large N*, *Phys. Rev. Lett.* **108** (2012) 137201.

[59] R. Ganesh, J. van den Brink, and S. Nishimoto, *Deconfined Criticality in the Frustrated Heisenberg Honeycomb Antiferromagnet*, *Phys. Rev. Lett.* **110** (2013) 127203.

[60] H. Büchler, M. Hermele, S. Huber, M. Fisher, and P. Zoller, *Atomic Quantum Simulator for Lattice Gauge Theories and Ring Exchange Models*, *Phys. Rev. Lett.* **95** (2005) 040402.

[61] L. Tagliacozzo, A. Celi, A. Zamora, and M. Lewenstein, *Optical Abelian Lattice Gauge Theories*, *Ann. Phys., NY* **330** (2013) 160.

[62] E. Zohar, J. Cirac, and B. Reznik, *Simulating (2 + 1)-Dimensional Lattice QED with Dynamical Matter Using Ultracold Atoms*, *Phys. Rev. Lett.* **110** (2013) 055302.

[63] D. Marcos, P. Widmer, E. Rico, M. Hafezid, P. Rabl, U.-J. Wiese, and P. Zoller, *Two-dimensional lattice gauge theories with superconducting quantum circuits*, *Annals of Physics* **351** (2014) 634.

[64] L. Tagliacozzo, A. Celi, P. Orland, and M. Lewenstein, *Simulations of non-Abelian gauge theories with optical lattices*, *Nature Commun.* **4** (2013) 2615.

[65] O. F. Syljuasen, *Continuous-time diffusion Monte Carlo and the quantum dimer model*, *Phys. Rev. B* **71** (2005) 020401.

[66] O. F. Syljuasen, *Plaquette phase of the square-lattice quantum dimer model: Quantum Monte Carlo calculations*, *Phys. Rev. B* **73** (2006) 245105.

[67] A. Ralko, D. Poilblanc, and R. Moessner, *Generic Mixed Columnar-Plaquette Phases in Rokhsar-Kivelson Models*, *Phys. Rev. Lett.* **100** (2008) 037201.

[68] D. Banerjee, F. Jiang, P. Widmer, and U.-J. Wiese, *The (2+1)d U(1) quantum link model masquerading as deconfined criticality*, *J. Stat. Mech.* **P12010** (2013).

[69] D. Banerjee, F. Jiang, P. Widmer, and U.-J. Wiese, *Crystalline Confinement*, *PoS(LATTICE 2013)* **333** (2013).

[70] D. Banerjee, M. Bögli, C. Hofmann, F. Jiang, P. Widmer, and U.-J. Wiese, *Interfaces, strings and a soft mode in the square lattice quantum dimer model*, *Phys. Rev. B* **90** (2014) 245143.

[71] D. Banerjee, M. Bögli, C. Hofmann, F. Jiang, P. Widmer, and U.-J. Wiese, *Insights into the Quantum Dimer Model on the Square Lattice*, *In preparation* (2015).

[72] I. Montvay and G. Münster, *Quantum Fields on a Lattice*. Cambridge University Press, 1994.

[73] J. B. Kogut, *Lattice Gauge Theory Approach to Quantum Chromodynamics*, *Rev. Mod. Phys.* **55** (1983) 775.

[74] G. t' Hooft, *A property of electric and magnetic flux in non-Abelian gauge theories*, *Nucl. Phys. B* **153** (1979) 141.

[75] L. Polley and U.-J. Wiese, *Monopole condensate and monopole mass in $U(1)$ lattice gauge theory*, *Nucl. Phys. B* **356** (1991) 629.

[76] A. S. Kronfeld and U.-J. Wiese, *$SU(N)$ gauge theories with C-periodic boundary conditions (I). Topological structure*, *Nucl. Phys. B* **357** (1991) 521.

[77] J. Liu, A. Sandvik, and L. Balents, *Emergence of U(1) Symmetry in the 3D XY Model with Z_q Anisotropy*, *Phys. Rev. Lett.* **99** (2007) 207203.

Erklärung

gemäss Art. 28 Abs. 2 RSL 05

Name/Vorname: Philippe Widmer

Matrikelnummer: 05-125-240

Studiengang: Physik

Bachelor ☐ Master ☐ Dissertation ☑

Titel der Arbeit: (2+1)-d Quantum Link and Quantum Dimer Models

LeiterIn der Arbeit: Prof. Dr. Uwe-Jens Wiese

Ich erkläre hiermit, dass ich diese Arbeit selbständig verfasst und keine anderen als die angegebenen Quellen benutzt habe. Alle Stellen, die wörtlich oder sinngemäss aus Quellen entnommen wurden, habe ich als solche gekennzeichnet. Mir ist bekannt, dass andernfalls der Senat gemäss Artikel 36 Absatz 1 Buchstabe r des Gesetzes vom 5. September 1996 über die Universität zum Entzug des auf Grund dieser Arbeit verliehenen Titels berechtigt ist. Ich gewähre hiermit Einsicht in diese Arbeit.

Bern, 29.06.2015

Ort/Datum

Unterschrift

Philippe Widmer

Curriculum Vitae

Personal Information

Date of birth	24. February 1986
Hometown	Heimiswil BE
Nationality	Switzerland

Education

2011 – 2015	**PhD in Theoretical Physics**, *University of Bern*, Bern.
August 2012	**INT Summer School on Lattice QCD for Nuclear Physics**, *University of Washington*, Seattle.
2009 – 2011	**Master of Science in Physics with special qualification in Theoretical Physics**, *University of Bern*, Bern.
2006 – 2009	**Bachelor of Science in Physics**, *University of Bern*, Bern.

Theses

PhD thesis

Title	*(2+1)d Quantum Link And Quantum Dimer Models*
Supervisor	Prof. Dr. Uwe-Jens Wiese

Master thesis

Title	*The 3-d 3-state Potts model with a non-zero density of static color charges*
Supervisor	Prof. Dr. Uwe-Jens Wiese

Bachelor thesis

Title	*Contact interactions in non-relativistic quantum mechanics*
Supervisor	Prof. Dr. Uwe-Jens Wiese

Winkelriedstrasse 37 – 3014 Bern
+41 76 592 90 32 • widmer@itp.unibe.ch